Models in Micrometeorology

Mann, Jakob

Publication date:
1994

Document Version
Publisher's PDF, also known as Version of record

Link back to DTU Orbit

Citation (APA):
Mann, J. (1994). *Models in Micrometeorology*. Forskningscenter Risø. Denmark. Forskningscenter Risoe. Risoe-R No. Risø-R-727 (ENG)

Models in Micrometeorology

Risø-R-727(EN)

Jakob Mann

Risø National Laboratory, Roskilde, Denmark
March 1994

Abstract This report consists of two parts. In the first a spectral tensor model of neutral atmospheric surface layer turbulence is developed. The model is validated trough comparison with second order turbulence statistics from the Great Belt Coherence Experiment, the Lammefjords Experiment and wind tunnel data from Danish Maritime Institute. Based on the spectral tensor an efficient and simple algorithm for simulation of three-dimensional wind fields is generated. The simulation is well suited for load calculation on bridges, wind turbines and other engineering structures. The spectral tensor is also used to estimate errors in momentum flux measurements close to the ground due to displacement of the sensors of vertical and horizontal velocity fluctuations.

In the second part mathematical tools are developed to determine how long a time series of a turbulent signal must be to estimate covariances and higher order moments with a specified statistical significance. Both systematic and random errors are treated. It is demonstrated theoretically, as well as experimentally with aircraft data from the convective boundary layer over the ocean and over land, that if the time series are assumed to be Gaussian the random errors are underestimated. A skewed model process gives better estimates of the random error. The tools are used in the convective boundary layer to show that the systematic flux and flux gradient errors can be important if fluxes are calculated from a set of several short flight legs or if the vertical velocity and scalar time series are high-pass filtered.

This thesis is submitted to the University of Aalborg in partial fulfillment of the requirements for the PhD-degree.

ISBN 87-550-1950-1
ISSN 0106-2840

Grafisk Service · Risø · 1994

CONTENTS

IA: The spatial structure of surface-layer turbulence

IB: Applications of the spectral tensor

Abstract This report consists of two parts. In the first a spectral tensor model of neutral atmospheric surface layer turbulence is developed. The model is validated trough comparison with second order turbulence statistics from the Great Belt Coherence Experiment, the Lammefjords Experiment and wind tunnel data from Danish Maritime Institute. Based on the spectral tensor an efficient and simple algorithm for simulation of three-dimensional wind fields is generated. The simulation is well suited for load calculation on bridges, wind turbines and other engineering structures. The spectral tensor is also used to estimate errors in momentum flux measurements close to the ground due to displacement of the sensors of vertical and horizontal velocity fluctuations.

In the second part mathematical tools are developed to determine how long a time series of a turbulent signal must be to estimate covariances and higher order moments with a specified statistical significance. Both systematic and random errors are treated. It is demonstrated theoretically, as well as experimentally with aircraft data from the convective boundary layer over the ocean and over land, that if the time series are assumed to be Gaussian the random errors are underestimated. A skewed model process gives better estimates of the random error. The tools are used in the convective boundary layer to show that the systematic flux and flux gradient errors can be important if fluxes are calculated from a set of several short flight legs or if the vertical velocity and scalar time series are high-pass filtered.

This thesis is submitted to the University of Aalborg in partial fulfillment of the requirements for the PhD-degree.

ISBN 87-550-1950-1
ISSN 0106-2840

Grafisk Service · Risø · 1994

Models in micrometeorology

CONTENTS

IA: The spatial structure of surface-layer turbulence

IB: Applications of the spectral tensor

IIA: How long is long enough?

IIB: Errors in airborne flux measurements

General introduction

This thesis consists of two parts. The first is focused on the properties of atmospheric turbulence of importance for load calculation on engineering structures. This accomplished by modeling of the so-called spectral tensor, i.e., the 3 by 3 covariance matrix of Fourier components of the three components of the velocity field. From this tensor the one point spectra and two point cross spectra can be derived. The second part is concentrated on the statistics of fluxes, variances and higher order moments measured in the atmosphere. The theory can be used to decide how long a time series must be to estimate moments of a turbulent quantity with a specified statistical error.

Most of the material in this thesis appears as articles accepted for publication in *Journal of Fluid Mechanics, J. Atm. Ocean. Tech.* and *J. Geophys. Res.*

— — —

Part I is divided into two parts. In Part IA I model the spatial structure of atmospheric surface layer turbulence at high wind speeds. I found the the basic idea of the model reading Townsend's *The Structure of Turbulent Shear Flow* (1976): When wind speeds are high the buoyancy forces will be small (neutral stratification) and shear dominates the flow. The interaction of shear and turbulence is then modeled by the linearized (i.e. the Reynolds stress terms are neglected) Navier–Stokes equation without any buoyancy term. In the atmosphere the eddies that buffet engineering structures are generally much larger than the viscous scales, so molecular viscosity is also neglected in the linearized Navier–Stokes equation. To simplify the mathematics the atmospheric surface layer wind profile is assumed to be approximately linear. This approximate equation of fluid motion is assumed to describe how turbulence is distorted or how 'eddies' are stretched by the shear (for a mental picture of this, see figure IA.2*a* & *b* on page 18).

At some instant, however, the stretched eddies will break up into smaller and presumably more isotropic eddies. These events cannot be described by the linearized equation so we have to use our intuition to *model* what is going on. I imagine that a particular eddy is stretched by the linear shear until it breaks up and ceases to exist. It is difficult to give a precise definition of an eddy and the concept of eddy lifetime may seem even more hazy. In the inertial subrange, however, it is possible from dimensional arguments to associate a time scale ('eddy lifetime', $\tau(k)$) to a particular eddy size (or inverse wave number, k^{-1}). Outside the inertial subrange, i.e. at larger scales, the dependence of lifetime on size becomes less obvious and different alternatives must be considered (see figure IA.3 on page 19).

The simplified Navier–Stokes equation gives the time evolution of the spectral component Φ_{ij} as a function of wavevector $\boldsymbol{k}$ and time t. As initial conditions I choose the isotropic von Kármán tensor, described by a length scale L and the spectral multiplier in the inertial subrange $\alpha\varepsilon^{\frac{2}{3}}$. The solution of the simplified fluid equations is combined with the consideration about eddy lifetime and the initial conditions to postulate a stationary spectral tensor for neutral surface layer turbulence as

$$\Phi_{ij} \equiv \Phi_{ij}\left(\boldsymbol{k}, \tau(k)\right). \tag{IA.3.2}$$

This means that small eddies with short lifetime are hardly distorted by the (mean) shear and are well described by the isotropic von Kármán tensor, while larger eddies with longer lifetimes will become stretched and anisotropic, because their lifetime is comparable to or larger than the inverse shear rate. Some (among them Leif Kristensen, Risø and Larry

Cornmann, NCAR) have suggested as an improvement to (IA.3.2) to time average the time dependent solution in order to get a stationary solution. This could for example be done by assuming a scale dependent turbulent viscosity. Since the linearization already is crude, I do not think such a refinement would improve the model significantly, but it is left to be tested.

It is obvious that all the assumptions and approximations will give a tensor model with some parameters to be determined from experimental data. The shape of $\tau(k)$, the eddy lifetime as a function of size, is fixed but this function has to be multiplied by a dimensionless parameter Γ. Secondly, a turbulence length scale L determines the initial isotropic von Kármán turbulence, and finally the parameter $\alpha\varepsilon^{\frac{2}{3}}$ is the spectral multiplier in the inertial subrange. The three parameters Γ, L and $\alpha\varepsilon^{\frac{2}{3}}$ are obtained by fitting the model to the spectral measured in one point. This is done for the Great Belt Coherence Experiment in figure IA.7 (page 29), the Lammefjord Experiment in figure IA.10 (page 33) and for a boundary layer wind tunnel in figure IB.10 (page 65). Once the parameters are extracted the two point statistics, such as coherences and phases, are predicted as shown on figure IA.8 for the Great Belt (page 30) and on figures IB.14 – 16 for the wind tunnel measurements (p. 70 – 72).

The model has several good features: The ratio between the spectra of vertical and horizontal velocity fluctuations is $\frac{4}{3}$ for very high frequencies, as expected from the isotropic theory of turbulence; the cross-spectrum between vertical and horizontal fluctuation has a $f^{-\frac{7}{3}}$ shape at high frequencies, as predicted by dimensional analysis and seen from experimental data. Furthermore, the variance of longitudinal fluctuations (along the direction of the mean wind) is larger than the variance of the transversal fluctuations which again is larger than that of the vertical fluctuations. Finally, the correlation between longitudinal and vertical fluctuations is negative as it should be in the surface layer. The ratios of all these statistics depend only on Γ, not on L or $\alpha\varepsilon^{\frac{2}{3}}$, and Γ can be adjusted to fit the ratios well.

The analysis so far has been focused on the shear. Julian Hunt, as editor of Journal of Fluid Mechanics, was uncomfortable with the absence of the surface/ground in the model. One can argue that the scale L is dictated by the presence of the ground, but it does not appear directly in the equations. It is expected that when eddies are large compared to the height above the ground, the blocking by the surface must influence the turbulence. His suggestion was to apply the works of Hunt & Graham (1978) and Lee & Hunt (1989). The introduction of a correction for the blocking does not weaken the theory since no extra fitting parameter needs to be introduced as the height above the ground is known. However, I do not expect the result in §IA.3.3to be the last word in the complicated modeling of vertically *inhomogeneous* surface layer turbulence. As discussed in §IA4 this model which includes blocking by the surface is slightly superior to the simpler theory which only focuses on the linear shear, but for many applications the complications shadow the gain (see §IA.B.2). Hunt and L. Kristensen gave independently of each other the fruitful suggestion to try different lifetime models outside the inertial subrange where I in the first version of the paper (= Part IA) simply extrapolated the inertial subrange lifetimes to smaller wavenumbers.

Part IA originated in an attempt to understand the data obtained in the Great Belt Coherence Experiment (Mann, Kristensen & Courtney, 1991). The tensor model of Kristensen *et al.* (1989) was first invoked. They postulate a simple spectral tensor assuming the symmetry group (IA.2.15) and simple $k = |\boldsymbol{k}|$ dependencies of some functions describing the tensor. From the tensor model Kristensen *et al.* (1989) demonstrate an analytic relation between models of the one point spectra and the tensor. Each of the three one-point spectra (longitudinal, transversal and vertical) is determined by three parameters, which are found from observations. Although having some success for the u- and v-coherences it appeared immediately that the w-coherence was very badly modeled. Several attempts were done to improve the model. More parameters were introduced in the one point spectral models so they matched the measurements perfectly. However, the cross-spectrum between u and w had to be zero because of the assumed symmetries and the coherences were still not satisfactorily predicted. I also tried some axisymmetric tensor models (Chandrasekhar 1950) but it soon appeared that not symmetries, but the rudimentary *dynamics* as presented in Part IA could model the spatial structure of sheared turbulence.

Once the spectral tensor models of Part IA proved useful in predicting the spatial structure from the Great Belt measurements it was tested on the Lammefjord Experiment (Courtney 1988, LAMEX). LAMEX was ideally suited for validation of the models because it had nine anemometers in a plane perpendicular to the prevailing wind direction. This comparison (see §IA.4.5) shows that for some second order statistics the blocking by the surface may be important.

The models in Part IA naturally leads to the three applications presented in Part IB. The first application pursues the simple idea of simulating a stochastic process from its spectrum assuming Gaussianity. An example of the resulting fields is shown in figure IB.4 on page 57 where 'eddies' are stretch in the direction of the mean wind field and tilted by the shear. Engineers at the Test Station for Wind Turbines at Risø are now beginning to use the simulation for load calculations on wind turbines. To test the simulation they have compared wind fluctuations measured at the leading edge of a rotating blade to the simulation with good results (Kretz *et al.* 1994). In the future I hope to apply the simulation to the design of bridges in cooperation with Danish Maritime Institute.

The second application in Part IB is a part of a project, still in the stage of measuring and data analyzing, about flux measurements, both scalar and momentum, with displaced sensors. When the sensors of vertical velocity and the scalar or horizontal velocity are not co-located one cannot be sure that the eddy-correlation technique gives the right fluxes. I make predictions about the momentum flux attenuation or enhancement due to u- and w-sensor not being co-located. The corrections are only relevant close to the ground.

The last application shows that the tensor describes the turbulence in the new, wide boundary layer wind tunnel at Danish Maritime Institute well. This is useful when predicting the loads on full-scale bridges from wind tunnel model measurements.

— — —

In Part II mathematical tools are developed to determine how long a time series of a turbulent signal must be to estimate covariances and higher order moments with a specified statistical significance. For a given averaging time T there is a systematic difference between the true flux or moment and the ensemble average of the time means of the same quantities. This difference, the systematic error, is a decreasing function of T tending to zero for $T \to \infty$. The variance of the time mean of the flux or moment, the so-called error variance, represents the random scatter of individual realizations which, when

T is much larger the integral time scale $\mathcal{T}$ of the time series, is also a decreasing function of T. The tools developed here makes it possible to assess the minimum value of T necessary to obtain systematic and random errors smaller than specified values. Assuming that the time series are either Gaussian processes or skewed processes derived from a Gaussian, both with exponential correlation functions, expressions for the systematic and random errors are obtained. These expressions show that the systematic error and the error variance in the limit of large T are both inversely proportional to T which means that the random error, i.e. the square root of the error variance, will in this limit be larger than the systematic error. We demonstrate theoretically, as well as experimentally with aircraft data from the convective boundary layer over the ocean and over land, that the assumption that the time series are Gaussian leads to underestimation of the random errors, while derived processes with more realistic skewnesses and kurtoses give better estimates. For example, compared to the Gaussian process, one has to measure twice as long for a time series with the typical skewness for scalars in the convective boundary layer in order to obtain a specified random error of the variance measurement.

The project was started a long time ago by Donald H. Lenschow (NCAR) and Leif Kristensen (Lenschow & Kristensen 1990) who conceived many of the basic ideas of Part IIA. The Lenschow & Kristensen (1990) paper only gives an asymptotic analysis in the sense that the length of the time series T is assumed much larger than the integral scale $\mathcal{T}$ of the time series, and they also assume the time series to be Gaussian. In addition, they obtained a wrong result for the random error of the third order moment. My contribution to the project is the non-asymptotic analysis, i.e. T is not assumed much larger than $\mathcal{T}$, the general formulation of the asymptotic analysis (§IIA.A and §IIA.B) and the investigation of the skewed processes. The data analysis and the comparison with theoretical expression were also carried out by me.

The paper 'How long is long enough when measuring fluxes and other turbulence statistics?' (= Part IIA without the appendices) will appear in the august 1994 issue of Journal of Atmospheric and Oceanic Technology. The appendices A and B (p. 100 and 102) appear in Lenschow, Mann & Kristensen (1993). Appendix C which concerns errors of skewness and kurtosis, or normalized third- and fourth-order moments, of atmospheric time series appears here for the first time.

Part IIB applies the results of Part IIA to airborne flux and flux gradient measurement in the convective boundary layer. Part IIB has been provisionally accepted by Journal of Geophysical Research. The systematic and random errors are estimated as functions of the length of a flight leg or of the cut-off wave length of a high pass filter, which is often used in analysis of airborne measurements.

Acknowledgments

I would like to express my gratitude to my 'local supervisor' at Risø, Dr. Leif Kristensen, for the almost daily discussions about ideas, models and experiments in relation to my thesis. I also owe thanks to Leif for introducing me to numerous people in the field of micrometeorology, especially during my stay at NCAR, where Leif seems to know everybody. Without Leif's tireless effort to improve my English and the clarity of my presentation this thesis would probably have been unreadable. Helpfulness and friendliness do not only apply to Leif but to all workers at the Department of Meteorology and Wind Energy (Risø), where I have spend most of the last three years.

I would like to stress the importance of the many criticisms and suggestions of my supervisor Professor Steen Krenk of University of Aalborg.

Thanks to Dr. Donald H. Lenschow my half year stay at National Center for Atmospheric Research (NCAR) has been both pleasant and most fruitful. Most of Part II has been prepared during my stay at NCAR in inspiring collaboration with Don.

The experimental basis of Part IA is mainly due to Dr. Michael S. Courtney (Risø), who always has been very helpful. I acknowledge Professor Julian Hunt for suggesting the analysis in §IA.3.3 and for numerous other comments to Part IA. Peter Kirkegaard has generously shared his knowledge of mathematics and numerical methods, which has been used both in Part IA and IB. Part IB has benefitted from the wind tunnel data provided by Tim Reinhold & Michael Brinch of the Danish Maritime Institute (DMI) and from the discussions with Guy L. Larose about force correlations on bridge decks. I am grateful to one of the referees of Part IIA for suggesting the analysis of non-Gaussian processes, which I thought was too difficult. That suggestion has greatly improved Part IIA. The analysis in Part IIB would not have been possible without the FIFE data provided by Robert D. Kelly of the University of Wyoming.

I have enjoyed the study groups with many of the Ph.D.-students at Risø on general micrometeorology and modeling of atmospheric dispersion. I also enjoyed the time spent studying stochastic differential equations with Professor Ove Ditlevsen and others from The Technical University of Denmark.

I would also like to thank Niels Gylling Mortensen (Risø) for helping me with many typographical problems.

I acknowledge the financial support from The Danish Research Academy and especially their financial incentive to go abroad for six months.

Finally, I will give my warmest thanks to Marianne Bom for encouragement.

REFERENCES

CHANDRASEKHAR, S. 1950 The theory of axisymmetric turbulence, *Phil. Trans.* A **242**, 557–577.

COURTNEY, M. S. 1988 An atmospheric turbulence data set for wind turbine research. In *Wind Energy Conversion, Proceedings of the 1988 BWEA Wind Energy Conference* (ed. D. J. Milborrow), 89–94. Mech. Engng Publ.

HUNT, J. C. R. & GRAHAM, J. M. R. 1978 Free-stream turbulence near plane boundaries, *J. Fluid Mech.* **84**, 209–235.

KRETZ, A., MADSEN, H. AA., PETERSEN, J. T. 1994 Measured and Simulated Turbulence – Compared at a Section of a Rotating Wind Turbine Blade, *Risø Report No. R-671*, 98 pp (draft).

KRISTENSEN, L., LENSCHOW, D. H., KIRKEGAARD, P. & COURTNEY, M. S. 1989 The spectral velocity tensor for homogeneous boundary-layer turbulence, *Boundary-Layer Meteorol.*, **47**, 149–193.

LEE, M. J. & HUNT, J. C. R. 1989 The structure of sheared turbulence near a plane boundary, *7th Symp. on Turbulent Shear Flows*, Stanford.

LENSCHOW, D. H. & KRISTENSEN, L. 1990 Errors in measuring second-, third-, and fourth-order moments of turbulence variables, in the proceedings from *9th Symp. on Turbulence and Diffusion*, held in Roskilde, Denmark, 90–93.

LENSCHOW, D. H., MANN, J. AND KRISTENSEN, L. 1993 How long is long enough when measuring fluxes and other turbulence statistics? NCAR/TN-389+STR. Available from NCAR, P.O. Box 3000, Boulder, CO80307, 53 pp.

MANN, J., KRISTENSEN, L. & COURTNEY, M. S. 1991 The Great Belt Coherence Experiment – A study of atmospheric turbulence over water, *Risø Report No. R-596*, 51 pp.

TOWNSEND, A. A. 1976 *The Structure of Turbulent Shear Flow*, 2nd ed., Cambridge University Press, 429 pp.

PART IA:

The spatial structure of neutral atmospheric surface-layer turbulence

By JAKOB MANN
Risø National Laboratory, 4000 Roskilde, Denmark

(Accepted for publication in *Journal of Fluid Mechanics*)

Modelling of the complete second order structure of homogeneous, neutrally stratified atmospheric boundary-layer turbulence, including spectra of all velocity components and cross-spectra of any combination of velocity components at two arbitrarily chosen points, is attempted. Two models based on Rapid Distortion Theory (RDT) are investigated. Both models assume the velocity profile in the height interval of interest to be approximately linear. The linearized Navier–Stokes equation together with considerations of 'eddy' lifetimes is then used to modify the spatial second order structure of the turbulence. The second model differs from the first by modelling the blocking by the surface in addition to the shear. The resulting models of the spectral velocity tensor contain only three adjustable parameters: A length scale describing the size of the largest energy containing eddies, a non-dimensional number used in the parametrization of 'eddy' lifetime, and the third parameter is a measure of the energy dissipation.

Two atmospheric experiments both designed to investigate the spatial structure of turbulence and both running for approximately one year are used to test and calibrate the models. Even though the approximations leading to the models are very crude they are capable of predicting well the two-point second order statistics such as cross-spectra, coherences and phases, on the basis of measurements carried out at one point. The two models give very similar predictions, the largest difference being in the coherences involving vertical velocity fluctuations, where the blocking by the surface seems to have a significant effect.

1. Introduction

Knowledge of the turbulent atmospheric wind field has become important in calculation of dynamic loads on some spatially extended structures, such as large bridges, towers and wind turbines. For many of these structures the cross-spectra of wind fluctuations at different points on the structure are paramount to the estimation of dynamic wind loads. Under some simplifying circumstances the spectrum of the modal forces on the structure can be written as weighted integrals of the cross-spectra. The weights include modal amplitude and drag or lift coefficients at different points of the structure (Davenport 1977). For more complicated structures with moving parts or in case of non-linear structural responses there is not a similarly simple relation between spectral characteristics of the flow and the forces. However, also in these cases the cross-spectra are important for the description of dynamic loads.

For some structures the streamwise wind component of the turbulent flow is important while for others the vertical velocity fluctuations give rise to loads. There may even be structures where combinations of velocity fluctuations in different direction at different points are of importance. It is therefore desirable to have a unified description of the complete two-point second order structure of the turbulence, i.e. cross-spectra of arbitrary wind components at two arbitrarily chosen points.

Many experiments have been carried out in order to measure the spectral characteristics of the turbulence at the lowest ~ 100 meters of the atmosphere (Panofsky & Dutton 1984). Most reported observations concern one-point spectra and there is a general agreement on the shapes of these, except at the lowest frequencies. In this paper we shall investigate two models of the spectral velocity tensor, $\Phi_{ij}(\mathbf{k})$, for horizontally homogeneous, atmospheric surface-layer turbulence for neutral stratification, which prevails at high wind speeds.

The basis of the models is *rapid distortion theory* (RDT), which implies a linearization of the Navier–Stokes equation. The models combine RDT with considerations about eddy lifetimes. The difference between the two models is that the latter in addition to the effects of shear also tries to take into account the blocking by the surface by inhomogeneous RDT (Hunt & Graham 1978; Gartshore *et al.* 1983; Lee & Hunt 1989) (see figure 2). The first model which only regards a uniform shear is abbreviated US, the second US+B.

Due to the difficulties in solving the Navier–Stokes equation the physical and mathematical approximations are quite crude. Therefore, the model has been calibrated and checked with data from two large experiments. In the first, turbulence was measured over water in connection with estimation of wind loads on what is going to be the world's largest suspension bridge (Mann, Kristensen & Courtney 1991; Larsen, 1992). The second experiment investigated turbulence structure over a rural area in Denmark in connection with wind loads on horizontal axis wind turbines (Courtney 1988).

In §2 we define the notation, discuss symmetries of different tensor models and briefly describe the isotropic tensor with the von Kármán energy spectrum on which the models in §3 are based. Then in §3 we present the tensor models which have only three parameters: A length scale, a constant connected to the 'lifetime' of the eddies, and a measure of the energy dissipation. Finally, in §4, we compare the two models with data by adjusting the three parameters to fit the one-point spectra and predicting the measured two-point cross-spectra.

2. Preliminaries

We present the basic definitions and notation together with some properties of the isotropic tensor which are needed.

2.1. *Definitions*

The turbulent velocity field $\tilde{\boldsymbol{u}}(\boldsymbol{x})$ is assumed to be incompressible, and the fluctuations, $\boldsymbol{u}(\boldsymbol{x}) = \tilde{\boldsymbol{u}}(\boldsymbol{x}) - \boldsymbol{U}(\boldsymbol{x})$, about the mean wind field, $\boldsymbol{U}(\boldsymbol{x})$, are, except for the model in §3.3, homogeneous in space. Therefore the covariance tensor

$$R_{ij}(\boldsymbol{r}) = \langle u_i(\boldsymbol{x}) u_j(\boldsymbol{x}+\boldsymbol{r}) \rangle \,, \tag{2.1}$$

where $\langle \quad \rangle$ denotes ensemble averaging, is only a function of the separation vector $\boldsymbol{r}$. From (2.1) it follows that

$$R_{ij}(\boldsymbol{r}) = R_{ji}(-\boldsymbol{r}) \tag{2.2}$$

For the components of the position vector in space, $\boldsymbol{x} = (x_1, x_2, x_3)$, we shall often use (x, y, z) or $(\Delta x, \Delta y, \Delta z)$ to denote position differences and for the components of the velocity fluctuations, $\boldsymbol{u} = (u_1, u_2, u_3)$, we sometimes use (u, v, w). Some assumption of homogeneity is unavoidable if we want the mathematics to be relatively simple. In this paper we model the Fourier transform of (2.1), *the spectral velocity tensor*:

$$\Phi_{ij}(\boldsymbol{k}) = \frac{1}{(2\pi)^3} \int R_{ij}(\boldsymbol{r}) \exp(-\mathrm{i}\boldsymbol{k} \cdot \boldsymbol{r}) \mathrm{d}\boldsymbol{r}, \tag{2.3}$$

where $\int \mathrm{d}\boldsymbol{r} \equiv \int_{-\infty}^{\infty} \int_{-\infty}^{\infty} \int_{-\infty}^{\infty} \mathrm{d}r_1 \mathrm{d}r_2 \mathrm{d}r_3$. Denoting complex conjugation by *, we see that (2.2) implies that $\Phi_{ij} = \Phi_{ji}^*$, i.e. the tensor is Hermitian.

Not only the Fourier transform of the covariance tensor is of interest but also the Fourier transform of the velocity field itself. Since the stochastic velocity field is not square integrable over all physical space we can represent the field in terms of a generalized stochastic Fourier-Stieltjes integral:

$$\boldsymbol{u}(\boldsymbol{x}) = \int \mathrm{e}^{\mathrm{i}\boldsymbol{k}\cdot\boldsymbol{x}} \mathrm{d}\boldsymbol{Z}(\boldsymbol{k}) \tag{2.4}$$

where the integration is over all wave-number space (Batchelor 1953). From homogeneity of the velocity fluctuations it follows that the stochastic vector field $\boldsymbol{Z}(\boldsymbol{k})$ has uncorrelated increments, i.e. $\langle \mathrm{d}Z_i(\boldsymbol{k}')\mathrm{d}Z_j^*(\boldsymbol{k}'')\rangle = 0$ for $\boldsymbol{k}' \neq \boldsymbol{k}''$. The process $\boldsymbol{Z}$ is connected to the spectral tensor by

$$\frac{\langle \mathrm{d}Z_i^*(\boldsymbol{k})\mathrm{d}Z_j(\boldsymbol{k})\rangle}{\mathrm{d}k_1 \mathrm{d}k_2 \mathrm{d}k_3} = \Phi_{ij}(\boldsymbol{k}) \tag{2.5}$$

which is valid for infinitely small $\mathrm{d}k_i$†. The representation, (2.4), may also form the basis for a numerical simulation of a turbulent wind field assuming the stochastic vector field $\boldsymbol{Z}(\boldsymbol{k})$ to be Gaussian and to have independent increments. A good introduction to the spectral tensor and its physical significance may be found in Tennekes and Lumley (1972).

An alternative to the spectral tensor is the set of all cross-spectra

$$\chi_{ij}(k_1, \Delta y, \Delta z) = \frac{1}{2\pi} \int_{-\infty}^{\infty} R_{ij}(x, \Delta y, \Delta z) \exp(-\mathrm{i}k_1 x) \mathrm{d}x \tag{2.6}$$

which contains the same information and which is most often used in practical applications, such as estimation of loads on structures. The connection between the components of the spectral tensor and the cross-spectra is

$$\chi_{ij}(k_1, \Delta y, \Delta z) = \int \Phi_{ij}(\boldsymbol{k}) \exp(\mathrm{i}(k_2 \Delta y + k_3 \Delta z)) \mathrm{d}\boldsymbol{k}_\perp \tag{2.7}$$

where $\int \mathrm{d}\boldsymbol{k}_\perp \equiv \int_{-\infty}^{\infty} \int_{-\infty}^{\infty} \mathrm{d}k_2 \mathrm{d}k_3$ (Lumley 1970, chap. 4).

---

† Other widely used ways to represent the velocity field are either as a Fourier series assuming the field to obey cyclic boundary conditions on a box in space much larger than the scales of interest (Townsend 1976), or assuming the velocity field to vanish outside a large box. The mathematical differences of these approaches are not of interest here.

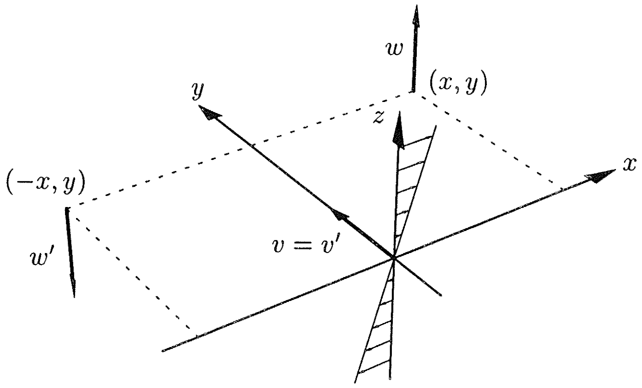

FIGURE 1. Coordinate system with the linear shear profile (2.13) shown along the z-axis. The vector v is the transversal component at the point $(0,0)$ and w is the vertical component at (x,y) of a turbulent velocity field. The vectors v' and w' are the same components after a rotation of 180° about the y-axis of the field.

Besides the cross-spectrum the *coherence* or *spectral coherence*

$$\mathrm{coh}_{ij}(k_1,\Delta y,\Delta z)=\frac{|\chi_{ij}(k_1,\Delta y,\Delta z)|^2}{F_i(k_1)F_j(k_1)}\qquad\text{(no summation)}\tag{2.8}$$

where $F_i(k_1)=\chi_{ii}(k_1,0,0)$ (no summation) is the one-point spectrum, is often reported in the literature. Sometimes the coherence is defined as the square root of the expression above. The phase, φ_{ij}, is defined as

$$\chi_{ij}(k_1,\Delta y,\Delta z)=|\chi_{ij}(k_1,\Delta y,\Delta z)|\exp\left(\mathrm{i}\varphi_{ij}(k_1,\Delta y,\Delta z)\right)\qquad\text{(no summation)}\tag{2.9}$$

and we note that from (2.7) and $\Phi_{ij}=\Phi^*_{ji}$ we get $\varphi_{ij}(k_1,\Delta y,\Delta z)=-\varphi_{ji}(k_1,-\Delta y,-\Delta z)$.

According to the definitions used here the (co-)variances can be expressed as

$$\langle u_i u_j\rangle=\langle u_i(\boldsymbol{x})u_j(\boldsymbol{x})\rangle=\int_{-\infty}^{\infty}\chi_{ij}(k_1)\mathrm{d}k_1=\int\Phi_{ij}(\boldsymbol{k})\mathrm{d}\boldsymbol{k}\tag{2.10}$$

With these conventions the (cross-)spectra $\chi_{ij}(k_1)=\chi_{ij}(k_1,0,0)$ are often called two-sided.

2.2. *Symmetries*

From symmetries of the spectral tensor it is possible to determine if some cross-spectra are real, purely imaginary or zero. Furthermore, they can be exploited in the numerical calculation of $\chi_{ij}(k_1)$ from $\Phi_{ij}(\boldsymbol{k})$.

We define the (second order) symmetry group of a turbulent field as the group of reflections and rotations of the space which leaves the statistics of the turbulent field unchanged. More precisely the symmetry group of a (stochastic) turbulent field is the subgroup of transformations T in the group of all orthonormal transformations in $\mathbf{R}^3$ for which the second order statistics of $u_i(\boldsymbol{x})$ are the same as $T_{ij}u_j(T\boldsymbol{x})$ (summation over repeated indices is understood). For the covariance tensor this means that

$$R_{ij}(\boldsymbol{r})=\langle u_i(\boldsymbol{x})u_j(\boldsymbol{x}+\boldsymbol{r})\rangle$$

$$= \langle T_{il} u_l(T\boldsymbol{x}) T_{jk} u_k(T\boldsymbol{x} + T\boldsymbol{r})\rangle = T_{il} R_{lk}(T\boldsymbol{r}) T_{jk} \tag{2.11}$$

for transformations in the symmetry group. Since the absolute value of the determinant of T is one we get, using the definition (2.3), for the spectral tensor

$$\Phi_{ij}(\boldsymbol{k}) = T_{il}\Phi_{lk}(T^*\boldsymbol{k})T_{jk} \tag{2.12}$$

where T^* is the adjoint of T (i.e. the transposed matrix).

For the models developed in §3 the mean wind field is assumed to be well represented by a uniform shear with the flow in the x_1-direction;

$$\boldsymbol{U}(\boldsymbol{x}) = \langle \tilde{\boldsymbol{u}}(\boldsymbol{x})\rangle = z\frac{\mathrm{d}U}{\mathrm{d}z}\boldsymbol{e}_1, \tag{2.13}$$

and the fluctuations are distorted by this shear†. The following symmetries apply to this situation: Firstly, for both the US and US+B models, there must be left-right symmetry (since we ignore the rotation of the of the Earth). Secondly, the US model is unaffected by a rotation of 180° about the x_2-axis and thus, ignoring the effect of gravity, the fluctuating field has this symmetry. Therefore, the symmetry group for the US model consists of four elements:

$$\left\{ I, \begin{pmatrix} 1 & 0 & 0 \\ 0 & -1 & 0 \\ 0 & 0 & 1 \end{pmatrix}, \begin{pmatrix} -1 & 0 & 0 \\ 0 & 1 & 0 \\ 0 & 0 & -1 \end{pmatrix}, -I \right\} \tag{2.14}$$

where I is the identity matrix. From the last element, $-I$, it follows from (2.12) and (2.3) that Φ is real and since it is Hermitian it is also symmetric. From the definition (2.6) and (2.11) we get, using the third element of the symmetry group, that $\chi_{ij}(k_1, y, 0)$ is purely imaginary for $\{i,j\} = \{1,2\}$ or $\{2,3\}$ and real otherwise. The case $\{i,j\} = \{2,3\}$ is shown in figure 1. The statistics of the turbulent field must be unchanged after a rotation of 180° about the y-axis, i.e. $\langle vw\rangle = \langle v'w'\rangle$ or $R_{23}(x,y,0) = -R_{23}(-x,y,0)$. From this relation and (2.6) it follows that the cross-spectrum $\chi_{23}(k_1, \Delta y, 0)$ is purely imaginary or equivalently that $\varphi_{23}(k_1, \Delta y, 0) = \pm 90°$. An example of a measured phase is shown in figure 9. Similarly, using the second element of the symmetry group one can prove that $\chi_{ij}(k_1, 0, \Delta z)$ is zero for $\{i,j\} = \{1,2\}$ or $\{2,3\}$.

It should be noted, that the third (and thereby also the last) element in the symmetry group is in fact only approximately valid in the neutral atmospheric boundary layer since the velocity profile is not linear but rather logarithmic because of the presence of the surface of the Earth. We therefore expect a model based on this symmetry group only to be valid for eddies of linear dimension smaller than the length over which the shear changes appreciably. A theory based on a logarithmic profile would be too complicated mathematically for us to deal with. (see Hunt *et al.* (1989) for an analysis of correlations and length scales in this case.) As a compromise we introduce the US+B model in §3.3 which also has uniform shear but breaks the 180° symmetry about the y-axis by modelling the blocking by the surface.

Related to the non-linear velocity profile a non-zero skewness of the w-component would also show that the 180° rotation about the y-axis is not a perfect symmetry. Measurements of $S_w \equiv \langle w^3\rangle / \sigma_w^3$ in the neutral surface layer from the Kansas experiment

---

† For neatness, we have here chosen $\boldsymbol{U}(\mathbf{o}) = \mathbf{o}$. We could have chosen, say, $\boldsymbol{U}(\mathbf{o}) = U_0\boldsymbol{e}_1$; it is just a matter of defining of the origin of the z-axis. The theories presented in §3 (US) only depend on the shear, not on the mean wind speed at the origin.

gives values between 0.1 and 0.2 (Izumi 1971) with higher values to the unstable side and lower values around zero to the stable side. We measure the skewness, S_w, to be 0.27 and −0.12 for the Great Belt Coherence Experiment (§4.2) and LAMEX (§4.5), respectively. Large Eddy Simulations of the neutral boundary layer give small negative skewnesses close to the surface (C.-H. Moeng, 1993, private communication), however, as pointed out by Moeng, in the surface layer LES may not resolve the motions sufficiently to predict the skewness. These limitations of LES have been discussed in Schmidt and Schumann (1989).

The group of symmetries of *axisymmetric turbulence* is all rotations about the axis of symmetry together with reflections in planes containing the axis and in the plane perpendicular to the axis. A model of axisymmetric turbulence has been developed by Chandrasekhar (1950) (also described in detail by Sreenivasan and Narasimha, 1978) and if the axis is vertical it is thought to give a good representation of convective turbulence without shear. However, vertical axisymmetry implies $\sigma_u^2 = \sigma_v^2$ which is not observed for atmospheric surface layer turbulence at high wind speeds.

Inspired by the axisymmetric tensor Kristensen *et al.* (1989) proposed a spectral tensor model with the following symmetry group:

$$\begin{pmatrix} \pm 1 & 0 & 0 \\ 0 & \pm 1 & 0 \\ 0 & 0 & \pm 1 \end{pmatrix} \tag{2.15}$$

By introducing 7 independent parameters defining various functions in their model Kristensen *et al.* could fit $F_1(k_1)$, $F_2(k_1)$ and $F_3(k_1)$, the measured one-point spectra of along wind transversal and vertical wind fluctuations, respectively, fairly well and thereby also giving the right proportions of the variances and the length scales of all three components. The calculated coherences, however, generally overestimated the measured coherences when the distance between the anemometers was not small compared to the height above the surface. Furthermore, reflection in the horizontal plane which is an element in (2.15) implies $\chi_{13}(k_1, 0, 0) = 0$ and $\varphi_{11}(k_1, 0, \Delta z) = 0$ which is not supported by data.

2.3. *Taylor's hypothesis*

Usually Taylor's hypothesis is used to convert measured time series into 'space series'. When the shear is zero the mean speed at all points in space is the same and the hypothesis can be straightforwardly applied to interpret two-point time spectra as space cross-spectra. When the shear is not zero, however, Taylor's hypothesis is not so easily applicable. Consequently it will be used heuristically as follows: Consider two points $\boldsymbol{x}_1$ and $\boldsymbol{x}_2$ with $\boldsymbol{x}_2 - \boldsymbol{x}_1$ perpendicular to $\boldsymbol{U}(\boldsymbol{x})$. Simultaneously measured time series $\tilde{\boldsymbol{u}}(\boldsymbol{x}_1, t)$ and $\tilde{\boldsymbol{u}}(\boldsymbol{x}_2, t)$ are interpreted as the wind field along two lines in space: $\tilde{\boldsymbol{u}}(\boldsymbol{x}_1 - \boldsymbol{U}_m t, 0)$ and $\tilde{\boldsymbol{u}}(\boldsymbol{x}_2 - \boldsymbol{U}_m t, 0)$, where $\boldsymbol{U}_m = (\boldsymbol{U}(\boldsymbol{x}_1) + \boldsymbol{U}(\boldsymbol{x}_2))/2$. The more direct use of Taylor's hypothesis, i.e. interpreting the time series as $\tilde{\boldsymbol{u}}(\boldsymbol{x}_1 - \boldsymbol{U}(\boldsymbol{x}_1)t, 0)$ and $\tilde{\boldsymbol{u}}(\boldsymbol{x}_2 - \boldsymbol{U}(\boldsymbol{x}_2)t, 0)$, would obviously be wrong and it would violate the assumption of homogeneity.

2.4. *The isotropic tensor with the von Kármán spectrum*

The symmetry group of isotropic turbulence is simply all rotations and reflections in $\mathbf{R}^3$. As argued in §2.2 the spectral tensor may be assumed to be real and symmetric because point reflection with respect to the origin, $-I$, is an element in the symmetry group. In the theory of isotropic turbulence the mean field is assumed to be constant, i.e. no shear. Furthermore, if the flow is assumed to be incompressible the spectral tensor can be written as

$$\Phi_{ij}(\boldsymbol{k}) = \frac{E(k)}{4\pi k^4}\left(\delta_{ij}k^2 - k_i k_j\right) \tag{2.16}$$

where $E(k)\mathrm{d}k$ is half the variance of the wind velocity fluctuations whose magnitude of the wave vector is in the range $(k, k+\mathrm{d}k)$, as it can be seen by integrating $\Phi_{ii}(\boldsymbol{k})$ over a spherical shell with constant k.

Von Kármán (1948) has suggested the following form of the energy spectrum

$$E(k) = \alpha\varepsilon^{\frac{2}{3}}L^{\frac{5}{3}}\frac{(Lk)^4}{(1+(Lk)^2)^{\frac{17}{6}}} \tag{2.17}$$

where ε is the rate of viscous dissipation of specific turbulent kinetic energy and L is a length scale. The empirical value of α is approximately 1.7. Using (2.7) to derive the one-point spectra, we get

$$F_1(k_1) = \frac{9}{55}\alpha\varepsilon^{\frac{2}{3}}\frac{1}{(L^{-2}+k_1^2)^{\frac{5}{6}}} \tag{2.18}$$

and for the v- and w-spectra:

$$F_i(k_1) = \frac{3}{110}\alpha\varepsilon^{\frac{2}{3}}\frac{3L^{-2}+8k_1^2}{(L^{-2}+k_1^2)^{\frac{11}{6}}} \qquad \text{for } i = 2, 3. \tag{2.19}$$

All the one-point cross-spectra are zero.

The length scale, L, in the one-point spectra can be calculated from $F_i(0)$. In the atmosphere, however, the spectra at the very lowest wavenumbers vary considerably due to instationarity and large scale phenomena, which are not of interest here. A better way of characterizing L is by the maximum of $k_1F_i(k_1)$. Denoting the wavenumber at maximum of $k_1F_i(k_1)$ by $1/L_{\mathrm{max},i}$ we get

$$L_{\mathrm{max},1} = \left(\frac{2}{3}\right)^{\frac{1}{2}}L \approx 0.816L \tag{2.20}$$

and

$$L_{\mathrm{max},i} = \frac{2}{(6+3\sqrt{5})^{\frac{1}{2}}}L \approx 0.561L \qquad \text{for } i = 2, 3 \tag{2.21}$$

so the maximum of $k_1F_i(k_1)$ occurs when k_1 is slightly larger than $1/L$.

The variances can easily be calculated from either (2.17), (2.18) or (2.19) using (2.10):

$$\sigma_{\mathrm{iso}}^2 = \sigma_{11}^2 = \sigma_{22}^2 = \sigma_{33}^2 = \frac{9}{55}\frac{\sqrt{\pi}\,\Gamma\left(\frac{1}{3}\right)}{\Gamma\left(\frac{5}{6}\right)}\alpha\varepsilon^{\frac{2}{3}}L^{\frac{2}{3}} \approx 0.688\alpha\varepsilon^{\frac{2}{3}}L^{\frac{2}{3}}, \tag{2.22}$$

All the co-variances are of course zero.

The advantage of the isotropic turbulence model is that it describes the spectra and cross-spectra well for high frequencies or small distances compared to the length scale of the turbulence. Furthermore, the cross-spectra can be calculated analytically in terms of Bessel functions for the von Kármán energy spectrum, (2.17), or even nore simply for $-\frac{5}{3}$ power law spectrum (Harris 1970; Kristensen & Jensen 1979).

The property of isotropic turbulence that the variances σ_u^2, σ_v^2 and σ_w^2 must all be equal is not supported by data. In fact $\sigma_w^2/\sigma_u^2 \approx 0.25$ and $\sigma_v^2/\sigma_u^2 \approx 0.5 - 0.7$ depending on the averaging time (usually $\sim$ 10 min. for meteorological measurements). Isotropy

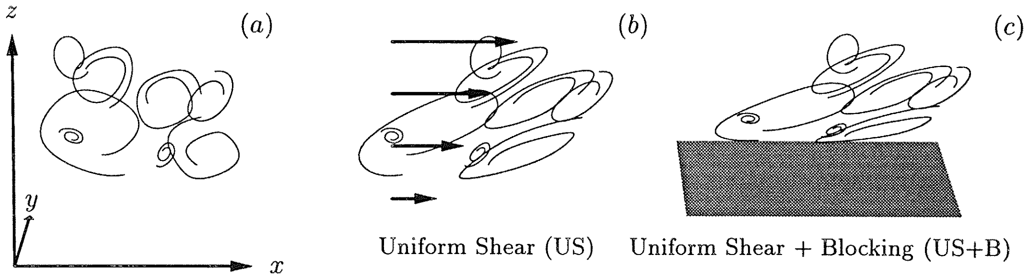

FIGURE 2. Sketch of investigated models. (*a*): Both models are based on isotropic turbulence with the von Kármán energy spectrum (§2.4). (*b*): The effect of shear is modelled by rapid distortion theory in §3.2. (*c*): In addition blocking by the surface is modelled by 'inhomogeneous rapid distortion theory' (Lee & Hunt 1989) (see §3.3).

also implies that χ_{13} must be zero which is certainly not the case at the lower frequencies (see the dot-dashed line in figure 7).

3. The velocity tensor for shear flow

In this section we sketch the development of two models of the spectral velocity tensor for neutral atmospheric surface-layer turbulence. We have argued that by neglecting the rotation of the Earth and the effect of gravity and by assuming a linear mean velocity shear, the statistics of the flow has only the four elements of (2.14) as a symmetry group. Our plan is to use RDT to estimate the effect of shear on the turbulence. RDT gives an equation for the evolution or the 'stretching' of the spectral tensor. If the initial conditions can be represented by the isotropic von Kármán tensor, (2.16), with the energy spectrum (2.17), then the tensor $\Phi_{ij}(\boldsymbol{k},t)$ will become more and more 'anisotropic' with time.

The linearization implied by RDT is unrealistic, however; at some point (in time) the stretched eddies will break up. We shall use this picture to make $\Phi_{ij}(\boldsymbol{k},t)$ stationary, i.e. not dependent on time. We postulate that eddies of linear dimension $\sim|\boldsymbol{k}|^{-1}$ (or more precisely the Fourier modes) are stretched by the shear over a time which is proportional to their life time. The life time τ is

$$\tau(k)\propto\varepsilon^{-\frac{1}{3}}k^{-\frac{2}{3}} \tag{3.1}$$

pertaining, at least in the inertial subrange, to eddies with wave vector magnitude $k=|\boldsymbol{k}|$ (Landau & Lifshitz 1987, §33).

The basic postulate of this paper is that the *stationary* spectral tensor

$$\Phi_{ij}(\boldsymbol{k})\equiv\Phi_{ij}\left(\boldsymbol{k},\tau(k)\right) \tag{3.2}$$

describes the surface layer turbulence well. The combination of RDT and scale dependent eddy life times has previously been used by Derbyshire & Hunt (1993).

Maxey (1982) has described a similar model with the exception that the lifetime τ

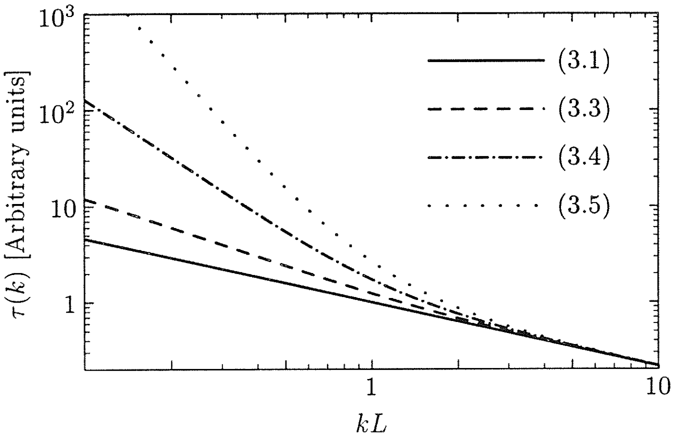

FIGURE 3. Eddy lifetimes as functions of the magnitude of the wave vector. The lifetimes given by (3.3) give the most realistic results.

was assumed to be constant for all wavevectors. ($\tau \mathrm{d}U/\mathrm{d}z$ is called 'the equilibrium value of the effective distortion strain' by Maxey (1982).) Maxey's model gives a reasonable, but not perfect, description of the ratios between σ_u^2, σ_v^2, σ_w^2 and $\langle uw \rangle$ for turbulent shear flows. There are two grave drawbacks when the model of Maxey (1982) is used to calculate spectra:

(i) The uw-cross-spectrum in the inertial subrange decays as $k_1^{-\frac{5}{3}}$ whereas $k_1^{-\frac{7}{3}}$ is more physical (Wyngaard & Coté 1972).

(ii) For typical values of the effective distortion strain the model predicts $F_u/F_w \sim 7$ in the inertial subrange whereas it should be $F_u/F_w = \frac{3}{4}$ (see figures 7 and 10).
The models presented here do not suffer from these shortcomings.

Several alternative expressions for the eddy lifetime outside the inertial subrange will be discussed in §3.1. Only an outline of the derivation of the Uniform Shear model (US) will be given in §3.2 since basic equations of rapid distortion theory has been given elsewhere (Townsend 1976). The modification of the model by blocking by the surface (US+B) is given in §3.3.

3.1. *Eddy lifetimes*

At scales larger than the inertial subrange (3.1) is not necessarily valid. We construct an alternative model for the 'eddy lifetime' assuming that the destruction of an eddy with size k^{-1} is mainly due to eddies comparable to or smaller than k^{-1}. The characteristic velocity of these eddies may be expressed as $\sim \left(\int_k^\infty E(p)\mathrm{d}p\right)^{\frac{1}{2}}$, and we simply assume the lifetime to be proportional to the size k^{-1} divided by this velocity:

$$\begin{aligned}\tau(k) &\propto k^{-1}\left(\int_k^\infty E(p)\mathrm{d}p\right)^{-\frac{1}{2}} \\ &\propto k^{-\frac{2}{3}}\left[{}_2F_1\left(\frac{1}{3},\frac{17}{6};\frac{4}{3};-(kL)^{-2}\right)\right]^{-\frac{1}{2}} \propto \begin{cases} k^{-\frac{2}{3}} & \text{for } k \to \infty \\ k^{-1} & \text{for } k \to 0 \end{cases}\end{aligned} \qquad (3.3)$$

where we have chosen E as the von Kármán energy spectrum (2.17) and where ${}_2F_1$ is the hypergeometric function.

Another lifetime model which has the right asymptotic behavior for $k \to \infty$ is the 'coherence-destroying diffusion time' (Comte-Bellot & Corrsin 1971, eq. 99)

$$\begin{aligned}\tau_D(k) &\propto k^{-2}\left[\int_k^\infty p^{-2}E(p)\mathrm{d}p\right]^{-\frac{1}{2}} \\ &\propto k^{-\frac{2}{3}}\left[{}_2F_1\left(\frac{4}{3},\frac{17}{6};\frac{7}{3};-(kL)^{-2}\right)\right]^{-\frac{1}{2}} \propto \begin{cases} k^{-\frac{2}{3}} & \text{for } k \to \infty \\ k^{-2} & \text{for } k \to 0 \end{cases}\end{aligned} \tag{3.4}$$

which was constructed as the square of the eddy size divided by a k-dependent 'turbulent viscosity'.

Further, the inverse 'eddy-damping rate'

$$\tau_E(k) \propto \left(k^3E(k)\right)^{-\frac{1}{2}} \propto \begin{cases} k^{-\frac{2}{3}} & \text{for } k \to \infty \\ k^{-\frac{7}{2}} & \text{for } k \to 0 \end{cases} \tag{3.5}$$

is used in eddy-damped quasi-normal theories of turbulence as a characteristic non-linear relaxation time (Lesieur 1987).

All lifetime models are shown in figure 3 normalized such that they coincide in the inertial subrange. It turns out that σ_u^2 becomes infinite using (3.4) or (3.5), while (3.1) and (3.3) give reasonable results. It also turns out that the spectra calculated from (3.3) fit the data better than (3.1) for which reason (3.3) is used in the rest of this paper. Some support for (3.3) may be found in Panofsky *et al.* (1982) who measured eddy 'response times' of eddies in the neutral atmospheric surface-layer. Also Kristensen and Kirkegaard (1987) were in their theoretical model of the growth of a puff in a turbulent fluid compelled to use (3.3) rather than (3.4) or (3.5).

It is convenient to write (3.3) as

$$\tau(k) = \Gamma\left(\frac{\mathrm{d}U}{\mathrm{d}z}\right)^{-1}(kL)^{-\frac{2}{3}}\left[{}_2F_1\left(\frac{1}{3},\frac{17}{6};\frac{4}{3};-(kL)^{-2}\right)\right]^{-\frac{1}{2}}, \tag{3.6}$$

where Γ is a parameter to be determined.

3.2. *The Uniform Shear model*

The flow field is decomposed into a mean and fluctuating part

$$\tilde{\boldsymbol{u}} = \boldsymbol{U} + \boldsymbol{u} \tag{3.7}$$

where $\boldsymbol{U}$ is given by (2.13). When appropriate we shall use the more general $U_i(\boldsymbol{x}) = x_j\partial U_i/\partial x_j$, where $\partial U_i/\partial x_j$ is a constant tensor, instead of (2.13). The Navier–Stokes equation for an incompressible fluid may be written as

$$\frac{\partial \tilde{u}_i}{\partial t} + \tilde{u}_j\frac{\partial \tilde{u}_i}{\partial x_j} = -\frac{1}{\rho}\frac{\partial p}{\partial x_i} + \nu\frac{\partial^2 \tilde{u}_i}{\partial x_j \partial x_j}, \tag{3.8}$$

assuming the kinematic viscosity ν constant and neglecting gravity and the rotation of the Earth. Upon elimination of the pressure by taking the divergence on both sides of (3.8) and after decomposition in means and fluctuations according to (3.7) we drop the non-linear and viscous terms and Fourier transform the resulting equation. Defining the 'average total derivative' of the velocity as $\frac{\mathrm{D}u_i}{\mathrm{D}t} = \frac{\partial u_i}{\partial t} + U_j\frac{\partial u_i}{\partial x_j} = \frac{\partial u_i}{\partial t} + x_k\frac{\partial U_j}{\partial x_k}\frac{\partial u_i}{\partial x_j}$ and interpreting the rate of change of wave number, $\mathrm{d}k_k/\mathrm{d}t$, by

$$\frac{\mathrm{d}k_k}{\mathrm{d}t} = -k_j \frac{\partial U_j}{\partial x_k} \tag{3.9}$$

the Fourier representation of the average total derivative of the velocity field may be written as

$$\frac{\mathrm{D}u_i(\boldsymbol{x},t)}{\mathrm{D}t} = \int \mathrm{e}^{\mathrm{i}\boldsymbol{k}\cdot\boldsymbol{x}} \left\{ \left(\frac{\partial}{\partial t} + \frac{\mathrm{d}k_k}{\mathrm{d}t}\frac{\partial}{\partial k_k} \right) \mathrm{d}Z_i(\boldsymbol{k},t) \right\} = \int \mathrm{e}^{\mathrm{i}\boldsymbol{k}\cdot\boldsymbol{x}} \left\{ \frac{\mathrm{Dd}Z_i(\boldsymbol{k},t)}{\mathrm{D}t} \right\}, \tag{3.10}$$

where we have implicitly defined $\mathrm{D}/\mathrm{D}t$ acting on a function of wavenumber and time. Combining this expressions with linearized and Fourier transformed version of (3.8) we get

$$\frac{\mathrm{Dd}Z_i(\boldsymbol{k},t)}{\mathrm{D}t} = \frac{\mathrm{d}U}{\mathrm{d}z} \left\{ -\delta_{i1} + 2\frac{k_i k_1}{k^2} \right\} \mathrm{d}Z_3(\boldsymbol{k},t) \tag{3.11}$$

which is the basic rapid distortion equation for shear flow. The differential equations (3.9) and (3.11) are easily solved given the initial conditions $\boldsymbol{k}(0) = \boldsymbol{k}_0 = (k_1, k_2, k_{30})$ and $\mathrm{d}\boldsymbol{Z}(\boldsymbol{k}_0, 0)$. Instead of time, t, we shall use the non-dimensional time, β, defined as

$$\beta = \frac{\mathrm{d}U}{\mathrm{d}z} t \quad . \tag{3.12}$$

First (3.9) is solved using the mean flow (2.13) giving

$$\boldsymbol{k}(t) = (k_1, k_2, k_3) \quad \text{where } k_3 = k_{30} - \beta k_1 . \tag{3.13}$$

The solution to (3.11) is then

$$\mathrm{d}\boldsymbol{Z}(\boldsymbol{k},\beta) = \begin{bmatrix} 1 & 0 & \zeta_1 \\ 0 & 1 & \zeta_2 \\ 0 & 0 & k_0^2/k^2 \end{bmatrix} \mathrm{d}\boldsymbol{Z}(\boldsymbol{k}_0, 0). \tag{3.14}$$

where

$$\zeta_1 = \left[C_1 - \frac{k_2}{k_1} C_2 \right] \quad , \quad \zeta_2 = \left[\frac{k_2}{k_1} C_1 + C_2 \right] \tag{3.15}$$

with

$$C_1 = \frac{\beta k_1^2 (k_0^2 - 2k_{30}^2 + \beta k_1 k_{30})}{k^2 (k_1^2 + k_2^2)} \tag{3.16}$$

and

$$C_2 = \frac{k_2 k_0^2}{(k_1^2 + k_2^2)^{\frac{3}{2}}} \arctan \left[\frac{\beta k_1 (k_1^2 + k_2^2)^{\frac{1}{2}}}{k_0^2 - k_{30} k_1 \beta} \right] . \tag{3.17}$$

The equations (3.13) and (3.14) give the temporal evolution of individual Fourier modes.

Given the initial second order statistics $\Phi_{ij}(\boldsymbol{k}_0, 0) = \Phi_{ij}^{\mathrm{iso}}(\boldsymbol{k}_0)$ as the isotropic von Kármán tensor, (2.16), with energy spectrum, (2.17), we then have an explicit expression for $\Phi_{ij}(\boldsymbol{k}, t)$ (using (2.5)).

To make a stationary model we use (3.6) and (3.2) discussed in the beginning of this section, i.e. we substitute t with τ given by (3.6). For the 33-component we get

$$\Phi_{33}(\boldsymbol{k}) = \Phi_{33}^{\mathrm{iso}}(\boldsymbol{k}_0) \frac{k_0^4}{k^4} = \frac{E(k_0)}{4\pi k^4} (k_1^2 + k_2^2) \tag{3.18}$$

where Φ_{33}^{iso} refers to the isotropic von Kármán tensor and E to the energy spectrum

(2.17). The other components become

$$\Phi_{11}(\boldsymbol{k}) = \frac{E(k_0)}{4\pi k_0^4}\left(k_0^2 - k_1^2 - 2k_1k_{30}\zeta_1 + (k_1^2+k_2^2)\zeta_1^2\right) \tag{3.19}$$

$$\Phi_{22}(\boldsymbol{k}) = \frac{E(k_0)}{4\pi k_0^4}\left(k_0^2 - k_2^2 - 2k_2k_{30}\zeta_2 + (k_1^2+k_2^2)\zeta_2^2\right) \tag{3.20}$$

$$\Phi_{12}(\boldsymbol{k}) = \frac{E(k_0)}{4\pi k_0^4}\left(-k_1k_2 - k_1k_{30}\zeta_2 - k_2k_{30}\zeta_1 + (k_1^2+k_2^2)\zeta_1\zeta_2\right) \tag{3.21}$$

$$\Phi_{13}(\boldsymbol{k}) = \frac{E(k_0)}{4\pi k_0^2 k^2}\left(-k_1k_{30} + (k_1^2+k_2^2)\zeta_1\right) \tag{3.22}$$

and

$$\Phi_{23}(\boldsymbol{k}) = \frac{E(k_0)}{4\pi k_0^2 k^2}\left(-k_2k_{30} + (k_1^2+k_2^2)\zeta_2\right). \tag{3.23}$$

The equations (3.18) to (3.23) with (3.6) constitute the Uniform Shear model (US).

These equations have two differences from the expressions of Townsend (1976) for plane shearing of homogeneous turbulence. The first is the elimination of time by (3.6) and the second and related difference is that we do not use the turbulent viscosity of Townsend, which would make the decay time time for all eddies equal, independent of their sizes. (There are, however, also two typographical errors in (3.12.4) of Townsend (1976): In the innermost brackets in the the expression for Φ_{11}, k_{20} should be changed into k_{30}. The expression for Φ_{13} should be divided by k_0^2.)

3.3. *The effect of blocking by the surface*

The US model presented in §3.2 has the symmetry group (2.14). This implies e.g. that the one-point cross-spectrum spectrum of longitudinal and vertical fluctuation $\chi_{uw}(k_1)$ is real and that $\chi_{vw}(k_1, \Delta y, \Delta z = 0)$ is purely imaginary, i.e. $\phi_{vw}(k_1, \Delta y, \Delta z = 0) = \pm 90°$. As seen from figure 10(*b*) $\mathrm{Im}(\chi_{uw}(k_1))$ is in fact negative, and $\phi_{vw}(k_1, \Delta y, \Delta z = 0)$ is systematically different from ±90° for low wavenumbers (see figure 9(*b*)). This means that the deviation from the reflection symmetry in the y-axis has measurable consequences. In this section we shall modify the US model by incorporating the effect of blocking by the surface which will break this reflection symmetry. The physical assumptions in this section are crude, especially for the atmospheric flows in consideration, but are made to illuminate effect of blocking in a tractable way.

We follow the ideas of Lee & Hunt (1989): They analyze by RDT how homogeneous turbulence in a uniform shear is distorted when a rigid surface at $z = 0$ is suddenly introduced at time $\beta = 0$. As in the US model we ignore viscosity so the only effect of the surface is to block vertical velocity fluctuation. The blocked velocity field $\boldsymbol{u}^B(\boldsymbol{x}, \beta)$ is written as $\boldsymbol{u}^B = \boldsymbol{u} + \boldsymbol{u}^S$, where $\boldsymbol{u}(\boldsymbol{x}, \beta)$ is the homogeneous velocity field from the US model and $\boldsymbol{u}^S$ obeys $w^S(x, y, 0, \beta) = -w(x, y, 0, \beta)$, such that $w^B = 0$ on the surface, and $\boldsymbol{u}^S \to 0$ for $z \to \infty$.

We no longer have homogeneity in the vertical direction and it is appropriate to use Fourier transforms in the two horizontal directions. The two-dimensional Fourier transform of the homogeneous velocity field $u_i(\boldsymbol{x})$ from the US model thus becomes

$$\mathrm{d}\mathcal{Z}_i(k_1, k_2, z, \beta) = \int_{k_3} \mathrm{d}Z_i \mathrm{e}^{\mathrm{i}k_3 z} \tag{3.24}$$

where $\int_{k_3}$ denotes integration over all k_3's and $\mathrm{d}Z_i$ is given by (3.14).

It can be shown (Hunt 1973; Hunt & Graham 1978) that $\boldsymbol{u}^S$ is irrotational at the initial instant ($\beta = 0$) and has the form

$$\mathrm{d}Z_3^S(k_1, k_2, z, 0) = -\mathrm{e}^{-z\kappa} \int_{k_3} \mathrm{d}Z_3(\boldsymbol{k}, 0). \tag{3.25}$$

and

$$\mathrm{d}Z_i^S(k_1, k_2, z, 0) = \mathrm{i}k_i \frac{\mathrm{e}^{-z\kappa}}{\kappa} \int_{k_3} \mathrm{d}Z_3(\boldsymbol{k}, 0) \quad \text{for } i = 1, 2 \tag{3.26}$$

where $\kappa = \left(k_1^2 + k_2^2\right)^{\frac{1}{2}}$. From the momentum equation Gartshore, Durbin & Hunt (1983) derive $\frac{\mathrm{D}}{\mathrm{D}\beta}\nabla^2 w^S = 0$ for a linear shear which implies

$$\mathrm{d}Z_3^S(k_1, k_2, z, \beta) = -\mathrm{e}^{-z\kappa} \int_{k_3} \mathrm{d}Z_3(\boldsymbol{k}, \beta) = -\mathrm{e}^{-z\kappa}\mathrm{d}Z_3(k_1, k_2, 0, \beta) \tag{3.27}$$

(see also Durbin, 1987).

The other two components of the velocity field may be found from first two components of the curl of the linearized momentum equations

$$\frac{\mathrm{D}}{\mathrm{D}\beta}\left(\frac{\partial w^S}{\partial y} - \frac{\partial v^S}{\partial z}\right) = \frac{\partial v^S}{\partial x} \quad \text{and} \quad \frac{\mathrm{D}}{\mathrm{D}\beta}\left(\frac{\partial u^S}{\partial z} - \frac{\partial w^S}{\partial x}\right) = \frac{\partial v^S}{\partial y} \tag{3.28}$$

as it has been done by Lee & Hunt (1989). The results are

$$\mathrm{d}Z_i^S(k_1, k_2, z, \beta) = \mathrm{i}\frac{k_i}{\kappa}\mathrm{e}^{-z\kappa} \int_{k_3} (1 + P_i(z))\,\mathrm{d}Z_3(\boldsymbol{k}, \beta) \tag{3.29}$$

where

$$P_1(z) = \frac{k^2 k_2^2}{2\kappa^2 k_1^2} Q(z) \quad \text{and} \quad P_2(z) = -\frac{k^2}{2\kappa^2} Q(z). \tag{3.30}$$

The function Q is given by

$$\begin{aligned} Q(z) = \mathrm{e}^{\mathrm{i}k_3 z} \Big\{ & \mathrm{e}^{\kappa z}\left[E_1(\kappa z + \mathrm{i}k_{30} z) - E_1(\kappa z + \mathrm{i}k_3 z)\right] \\ & - \mathrm{e}^{-\kappa z}\left[2\pi \mathrm{i} H(-k_3 k_{30}) + E_1(-\kappa z + \mathrm{i}k_{30} z) - E_1(-\kappa z + \mathrm{i}k_3 z)\right] \Big\} \end{aligned} \tag{3.31}$$

where H is the Heaviside function ($H(x) = 1$ for $x > 0$ and 0 for $x < 0$) and E_1 is the exponential integral function.

Using (3.24), (3.27) and (3.29) and eliminating the time dependence by (3.2) the spectral tensor for the blocked flow now becomes a function of the two horizontal wavevectors and two heights above the surface:

$$\begin{aligned} & \Phi_{ij}^B(k_1, k_2, z_1, z_2) \equiv \\ & \qquad \frac{\left\langle \left(\mathrm{d}Z_i(k_1, k_2, z_1) + \mathrm{d}Z_i^S(k_1, k_2, z_1)\right)^* \left(\mathrm{d}Z_j(k_1, k_2, z_2) + \mathrm{d}Z_j^S(k_1, k_2, z_2)\right) \right\rangle}{\mathrm{d}k_1 \mathrm{d}k_2} \end{aligned} \tag{3.32}$$

from which all spectra and cross-spectra can be derived. As an example the 11-component becomes

$$\Phi_{11}^B(k_1, k_2, z_1, z_2) = \int_{-\infty}^{\infty} \Phi_{11}(\boldsymbol{k})\mathrm{e}^{\mathrm{i}k_3(z_2 - z_1)}$$

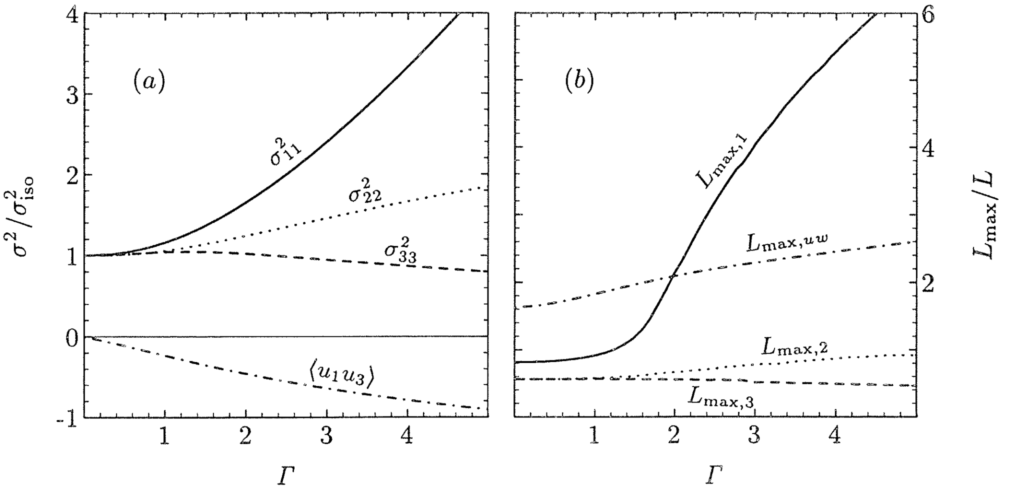

FIGURE 4. Properties of the uniform shear model as functions of the parameter Γ; (*a*): (Co-)variances divided by the isotropic variance (2.22), (*b*): Length scales of (cross-)spectra defined by (3.34) divided by L.

$$+ \frac{\mathrm{i}k_1}{\kappa}\left\{(1+P_1(z_2))\mathrm{e}^{-\mathrm{i}k_3z_1}\mathrm{e}^{-\kappa z_2} - (1+P_1(z_1))^*\mathrm{e}^{\mathrm{i}k_3z_2}\mathrm{e}^{-\kappa z_1}\right\}\Phi_{13}(\boldsymbol{k})$$
$$+ k_1^2\frac{\mathrm{e}^{-\kappa(z_1+z_2)}}{\kappa^2}(1+P_1(z_1))^*(1+P_1(z_2))\Phi_{33}(\boldsymbol{k})\mathrm{d}k_3 \qquad (3.33)$$

Though being more complicated than the US model the US+B model do not contain more adjustable parameters since the distance to the surface z is known.

3.4. *Properties of the sheared velocity tensors*

We shall now investigate the basic properties of the sheared velocity tensors, (3.18) through (3.23) and (3.32). The only four (co-)variances which are not zero, i.e. $\sigma^2_{11} = \sigma^2_u$, $\sigma^2_{22} = \sigma^2_v$, $\sigma^2_{33} = \sigma^2_w$ and $\langle uw\rangle$, are calculated numerically by (2.10) and are shown in figure 4(*a*) for the US model as functions of Γ. The model exhibits the ordering $\sigma^2_u > \sigma^2_v > \sigma^2_w$ and a negative co-variance of u and w as observed in neutral flows over homogeneous terrain in the atmosphere. In figure 5(*a*) the (co-)variances from the US+B model (§3.3) for $\Gamma = 3.5$ are shown. It is seen that σ^2_w and $\langle uw\rangle$ are attenuated strongly close to the surface. This is not consistent with surface-layer scaling where $\langle uw\rangle$ is approximately constant. However, the US+B model may be able to model the surface-layer turbulence within a horizontal slab where $\langle uw\rangle$ is not varying too much.

Another characteristic feature of the one-point (cross-)spectra is the extremum of $k_1F_i(k_1)$ or $k_1\mathrm{Re}(\chi_{13}(k_1))$. Assuming isotropy this could be done analytically (2.20 and 2.21), but in the sheared case the extremum must be found numerically by integrating (2.7) with $\Delta y = \Delta z = 0$. Defining

$$L_{\mathrm{max},i} \equiv 1/k_{\mathrm{max},i}, \qquad (3.34)$$

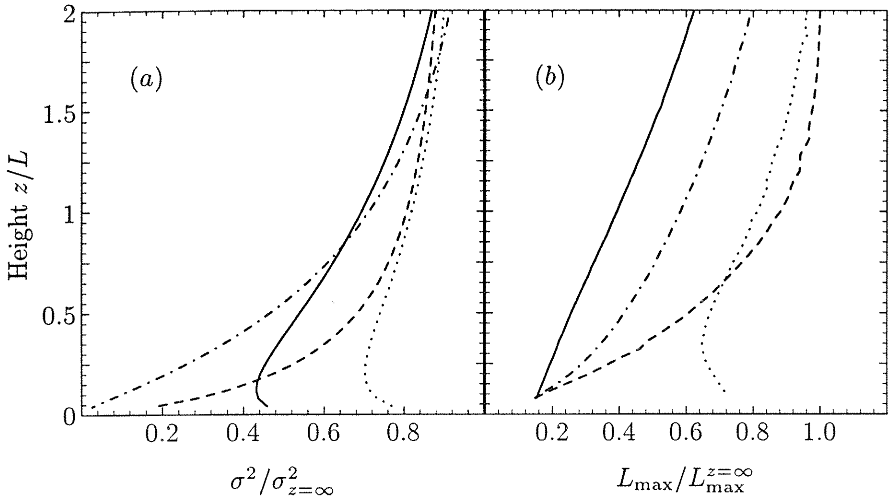

FIGURE 5. The effect of blocking on the (co-)variances (*a*) and length scales (*b*) as function of distance to the surface normalized by the unblocked values. The lifetime parameter Γ is 3.5. See figure 4 for legends to the curves.

where $k_{\max,i}$ is the solution to

$$\frac{\mathrm{d}}{\mathrm{d}k_1}\left(k_1 F_i(k_1)\right) = 0$$

we get the ordering $L_{\max,1} > L_{\max,2} > L_{\max,3}$ for the US model as seen from figure 4(*b*), which is in at least qualitative agreement with experiments. The length scales of the US+B model are strongly attenuated close to the surface as seen from figure 5(*b*).

4. Experimental validation

To test the tensor models described in §3 our strategy is:

(i) We determine the three parameters L, Γ and $\alpha\varepsilon^{\frac{2}{3}}$ of each of the models from the four non-zero spectra measured in *one* point, namely $F_u(k_1)$, $F_v(k_1)$, $F_w(k_1)$ and $F_{uw}(k_1) = \mathrm{Re}\,(\chi_{uw}(k_1))$. (In the case of the model in §3.3 $\mathrm{Im}(\chi_{uw}(k_1))$ is also non-zero.)

(ii) Then we predict all *two-point* cross-spectra or coherences.

(iii) Finally, we compare the predicted and measured two-point cross spectra.

The easiest way to extract the parameters from the measured spectra would be to estimate the length scales, defined as the reciprocal of the wavenumber that extremizes $k_1 F(k_1)$, and then determine Γ and L from figure 4(*b*) in case of the US model. The measured variances could then be used the estimate $\alpha\varepsilon^{\frac{2}{3}}$ from figure 4(*a*) and (2.22), or alternatively the parameter could be determined from $\lim_{k_1\to\infty} k_1^{\frac{5}{3}} F_1(k_1)$ which for $i = 1$ is $\frac{9}{55}\alpha\varepsilon^{\frac{2}{3}}$ and for $i = 2, 3$ is $\frac{12}{55}\alpha\varepsilon^{\frac{2}{3}}$, see (2.18) and (2.19), for which the limits still are valid in the sheared case because the distortion tends to zero for large wavenumbers according to (3.1). There are, however, several reasons not to proceed in that way. Firstly because the time series available are of limited length the estimated spectra appear 'ragged' and the global extrema are greatly influenced by random spikes in the spectra. Secondly, the measured variances depend on the filtering by the instruments in the high frequency end and on large scale phenomena in the low frequency end, which can be caused by small departures from neutral stratification. We do not want to model these very low frequency phenomena.

Instead we find the parameters by performing a χ^2-fit of the models to the data. In other words we minimize

$$\chi^2(\Gamma, L, \alpha\varepsilon^{\frac{2}{3}}) = \sum_{j=1}^{N} \frac{(F_{uw,t}(k_j) - F_{uw}(k_j))^2}{\sigma_u(k_j)\sigma_w(k_j)} + \sum_{i=1}^{3}\sum_{j=1}^{N} \frac{(F_{i,t}(k_j) - F_i(k_j))^2}{\sigma_i^2(k_j)}, \tag{4.1}$$

where N is the number of wavenumbers in the estimated spectra, a subscript t means theoretical model values calculated by (2.7) with $\Delta y = \Delta z = 0$, using the tensor models described in §3. The σ^2's are the variances of the spectral estimates at the given wavenumber, which will be discussed below.

4.1. *Time series analysis*

The spectra are estimated by dividing the time series into a number, n, of 'ensembles' of equal duration. Each segment is Fourier transformed and the spectrum is the average of the absolute square of the Fourier transform over all the ensembles. Cross-spectra are the ensemble average of Fourier amplitude of the first time series times the complex conjugate of the second. The coherence is estimated as the absolute square of the cross-spectrum divided by the product of the estimated spectra, and the phase is argument of the complex cross-spectrum, in accordance with (2.8) and (2.9), respectively.

Under the assumption that the time series is long compared to the time scale of the spectrum L/U, the relative standard deviation of the spectral estimate is,

$$\frac{\sigma(F_i)}{\langle F_i \rangle} = \frac{1}{\sqrt{n}} \tag{4.2}$$

and for the cross-spectrum

$$\frac{\sigma(\chi_{ij})}{(\langle F_i \rangle \langle F_j \rangle)^{\frac{1}{2}}} = \frac{1}{\sqrt{n}}, \tag{4.3}$$

(Koopmans 1974). Often the spectra are block averaged over, say, n_b consecutive frequencies or wavenumbers in which case the relative standard deviation becomes $(n_b n)^{-\frac{1}{2}}$.

As an example the spectra in figure 7 are made on basis of time series of length 6 h = 21600 s, which are divided into 27 pieces of 800 s. The relative standard deviation is thus $27^{-\frac{1}{2}} \approx 19\%$ at the lower wave numbers and smaller at higher wave numbers, where block averaging is applied.

If we use (4.2) and (4.3) in the χ^2-fit, (4.1), the data will be closely fitted at the high wave numbers but may be fitted poorly at the lower wave numbers. In practice we have found that constant relative standard deviations give more satisfactory fits.

The statistics of the estimated coherences are more complicated. Kristensen & Kirkegaard (1986) have analyzed the problem in depth. We shall use their results derived under the assumption that the segments of the time series are independent of each other. Let coh_n denoted the coherence estimated as described above from n segments of two time series having the true coherence, coh. The (ensemble) average of this stochastic variable is unfortunately not the true coherence, coh, but

$$\langle \mathrm{coh}_n \rangle = \alpha_1 \tag{4.4}$$

with α_1 given by

$$\alpha_1 = 1 - \frac{n-1}{n}(1-\mathrm{coh})^n \, {}_2F_1(n, n; n+1; \mathrm{coh}). \tag{4.5}$$

It can shown that $\langle \mathrm{coh}_n \rangle > \mathrm{coh}$, i.e. the coherence is on average or systematically overestimated, and that $\lim_{n\to\infty} \langle \mathrm{coh}_n \rangle = \mathrm{coh}$. For the number of segments we have used for the estimation of the coherence (≥ 144) the overestimation is almost insignificant. F.ex. $\langle \mathrm{coh}_{144} \rangle = 0.5017$ for $\mathrm{coh} = 0.5$ and $\langle \mathrm{coh}_{144} \rangle = 0.0168$ for $\mathrm{coh} = 0.01$.

Kristensen & Kirkegaard (1986) found the ensemble variance of the coherence estimate to be

$$\mathrm{Var}(\mathrm{coh}_n) = \alpha_2 - \alpha_1^2 \tag{4.6}$$

where

$$\alpha_2 = 1 - (1-\mathrm{coh})^n (n-1) \times \left\{ \frac{n}{n+1} \, {}_2F_1(n+1, n; n+2; \mathrm{coh}) - \frac{n-2}{n} \, {}_2F_1(n, n; n+1; \mathrm{coh}) \right\} \tag{4.7}$$

which has the property that $\lim_{n\to\infty} \mathrm{Var}(\mathrm{coh}_n) = 0$.

In order to assess the success of the prediction of the coherence we define a 'goodness' parameter

$$G = \frac{\sigma_{\mathrm{coh}}}{\sigma_{\mathrm{coh},t}} \tag{4.8}$$

which is the ratio of the actual integrated scatter of the data around the predicted coherence, σ_{coh}, to the theoretically expected scatter, $\sigma_{\mathrm{coh},t}$. The integrated scatter is

$$\sigma_{\mathrm{coh}}^2 = \frac{1}{N} \sum_i^N (\langle \mathrm{coh}_{n,t}(k_i) \rangle - \mathrm{coh}_n(k_i))^2 \tag{4.9}$$

where $\mathrm{coh}_n(k_i)$ is the coherence estimated from n segments of the time series at the wavenumber k_i, and $\langle \mathrm{coh}_{n,t}(k_i) \rangle$ is the theoretically predicted coherence with the small overestimation added caused by the finite number of degrees of freedom according to (4.4). N is the number of wavenumbers taken into the comparison with data. The expected scatter for a perfect theory is

$$\sigma_{\mathrm{coh},t}^2 = \frac{1}{N} \sum_i^N \mathrm{Var}\left(\mathrm{coh}_{n,t}(k_i)\right), \tag{4.10}$$

where the variance of the predicted coherence is given by (4.6). For a perfect theory the value of G should be close to one.

Finally, we shall also use a approximate expression for the variance of the phase estimate from Kristensen & Kirkegaard (1986):

$$\mathrm{Var}(\varphi) \approx \frac{1-\mathrm{coh}}{2(n-1)\,\mathrm{coh}} \left[1 - (1-\mathrm{coh})^{n-1}\right] \tag{4.11}$$

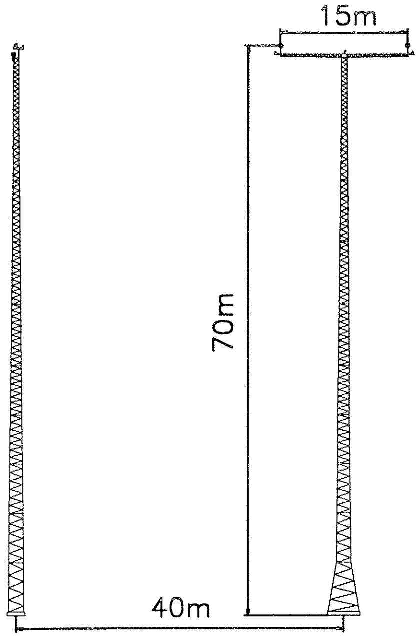

MMM, NCAR

FIGURE 6. The mast array on Sprogø viewed from SSE. The tiny dots at the top of the masts are the omni-directional sonic anemometers.

4.2. *The Great Belt Coherence Experiment*

The construction of the world's largest suspension bridge connecting two islands of Denmark, Funen and Zealand, is about to begin. The suspension bridge will have a main span of 1,624 m and the 27 m wide girder deck will rise almost 70 m over the waters of the Great Belt. The girder will be aerodynamically shaped and a large part of the dynamic force on it arises from the turbulence of the wind. The cross-spectrum of vertical velocity fluctuations $\chi_{ww}(k_1, \Delta y, 0)$ which give rise to lift forces on the girder, but also χ_{uu} is of importance for the estimation of dynamic loads on the bridge. Risø National Laboratory was therefore asked to perform an experiment to measure and model the relevant cross-spectra or coherences for the design basis of the Great Belt Bridge.

4.3. *Description of the experiment*

In order to conduct the coherence measurements a 70 m high mast was erected 40 m from an existing mast on the easterly spit of Sprogø, an island in the midst of the Great Belt. A 15 m long horizontal boom was mounted symmetrically at the top of the new mast so that the whole construction has the form of a letter "T". A Kaijo-Denki DAT-300 omni-directional sonic anemometer was installed at each end of the boom and at the top of the old mast, providing 15.0, 32.5 and 47.5 m horizontal separations between the three co-linear instruments. The mast array is shown in figure 6.

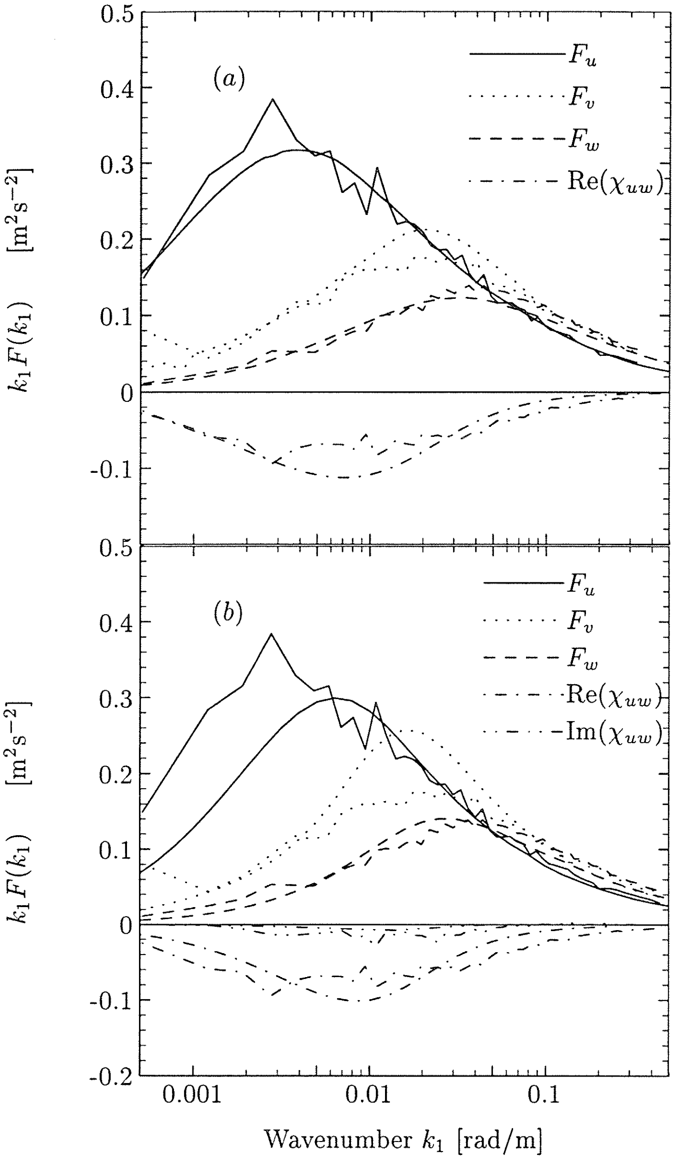

FIGURE 7. Fit of the model spectra (smooth lines) to the data (ragged lines) from the Great Belt Coherence Experiment. The US model is shown in (*a*) US+B in (*b*). Since $\mathrm{Im}(\chi_{uw}) = 0$ for the US model it is only shown in (*b*). The values of the model parameters are given in table 1.

The masts had other instruments to measure velocity and temperature profiles in order to determine the stability and to cross-check the sonic anemometers.

We obtained one year of excellent data from which we can calculate lateral coherences with unsurpassed precision. More details about the experiment including correction for flow distortion by the sonic anemometers may be found in Mann *et al.* (1991).

	Great Belt		LAMEX	
	US	US+B	US	US+B
L [m]	61	100	42	67
Γ	3.2	3.8	2.6	3.4
$\alpha\varepsilon^{\frac{2}{3}}$ [$\mathrm{m}^{\frac{4}{3}}\mathrm{s}^{-2}$]	0.11	0.105	0.095	0.092

TABLE 1. Parameters obtained by fitting models to the data. US: Uniform shear model (§3.2), US+B: Uniform shear + blocking effects (§3.3). Compare with figures 7 and 10.

	$\Delta y = 15$ m		$\Delta y = 32.5$ m		$\Delta y = 47.5$ m	
Components	US	US+B	US	US+B	US	US+B
uu	1.5	2.1	2.3	1.8	3.7	2.8
vv	2.0	2.7	1.7	3.0	2.0	3.3
ww	3.0	3.7	3.8	3.4	4.4	2.9
uv	1.1	1.1	1.5	1.2	1.8	1.5
uw	4.7	3.3	3.9	2.4	3.7	2.2
vw	1.2	1.0	1.4	1.2	1.7	1.4

TABLE 2. The 'goodness', G, of the coherence prediction given by (4.8). Compare with figures 8 and 9. A perfect prediction has $G = 1$.

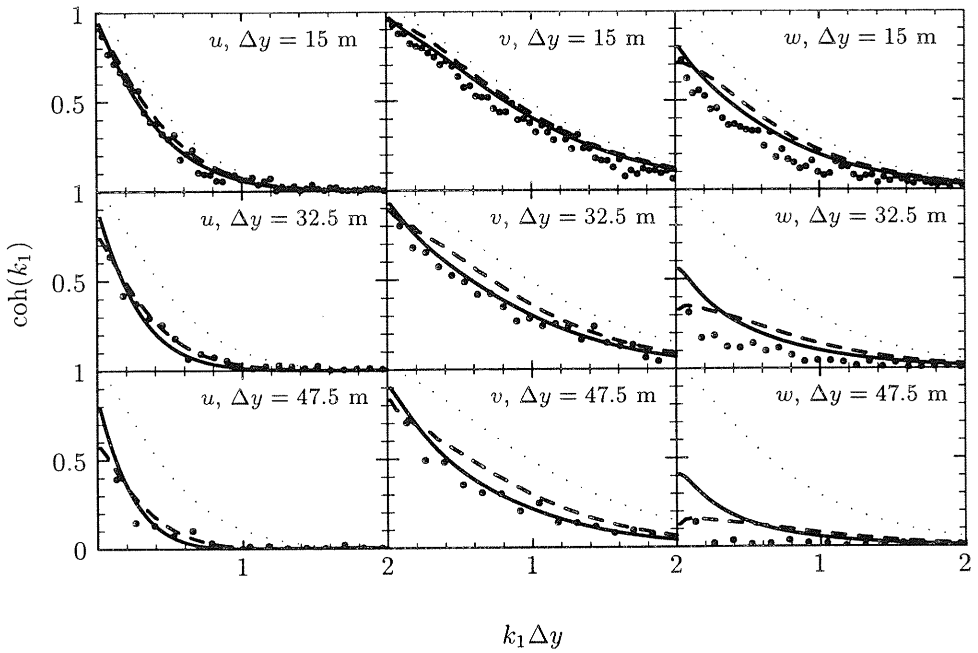

FIGURE 8. Measured (dots) and predicted coherences (solid lines, US; dashed lines, US+B) at all horizontal separations from the Great Belt. The rightmost plot at the top is $\mathrm{coh}_{11}(k_1, 15\mathrm{m}, 0)$. The dotted lines are the isotropic inertial range coherences, i.e. coherences valid for very small Δy (Harris 1970; Kristensen & Jensen 1979). Compare with table 2.

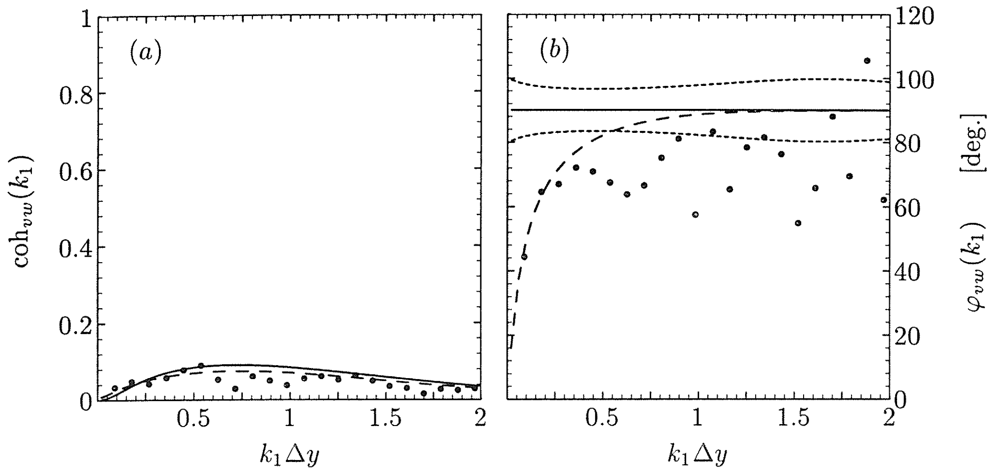

FIGURE 9. Coherence (*a*) and phase (*b*) between the v- and the w-component for a purely horizontal separation of $\Delta y = 32.5$ m from the Great Belt. The solid curve is the prediction by the US model, the dashed is the US+B model and the dots are experimental values. The short-dashed curves in (*b*) are the theoretical 1-σ deviations of the phase from the US model according to (4.11).

4.4. *Comparison with data*

To test the models we have selected a six hour time series. The wind direction is virtually perpendicular to the instrument line and the wind speed is fluctuating around 22.3 ms^{-1} at 70 m above the sea. The upstream over-water fetch is uninterrupted for more than 20 km. One-point spectra are calculated as described in §4.1 and are shown twice in figure 7.

The parameters of the models are found by minimizing (4.1). Keeping in mind that all four non-zero one-points spectra are fitted simultaneously with only *three* parameters the fits for both models are very satisfactory.

The coherences are now predicted by performing the integral (2.7) numerically and using the definition of coherence, (2.8). The numerics of a fast evaluation of (2.7) are described in Mann *et al.* (1991). In table 2 the goodness, G, of the predictions of all possible combinations of velocity components at the three different horizontal distances for both models are shown. To get an idea of the meaning of G table 2 should be compared to figure 8, where the measured and predicted coherences for some component combinations are plotted.

There is generally a good agreement between measurements and predictions. One of the poorer predictions in figure 8 is by the US model of $\mathrm{coh}_{33}(k_1, 47.5\ \mathrm{m}, 0)$. In this case $G = 4.4$ as seen from table 2 and the US+B model obviously gives a better prediction with $G = 2.9$. Generally, there is otherwise not very large differences between the model predictions. Large departures from the isotropic inertial subrange coherences are seen at separations as small as $\Delta y = 15$ m.

As an example of coherence between different components of the wind field we have shown coh_{vw} in figure 9(*a*) which is small but significantly larger than zero. The corre-

46 m	sonic		
30 m	cup	cup	cup
20 m	cup		cup
10 m	cup	cup	cup
Position (y, z)	0 m	20 m	30 m

TABLE 3. Position of the instruments of the Lammefjord Experiment.

sponding phase is shown in figure 9(*b*). In the discussion about symmetries in §2.2 we found that if the turbulent field has the symmetry group (2.14) as the US model, then χ_{vw} is purely imaginary. If this is the case, the phase should be close to $\pm 90^\circ$ which is not found at the lowest wave numbers in figure 9(*b*). The US+B model gives a slightly better prediction of the phase.

The US tensor model has been tested with other runs from the Great Belt with mean wind speeds in the range 12.5 ms^{-1} to 20 ms^{-1} and with small departures from neutral stability in Mann *et al.* (1991). They used the inertial subrange lifetime (3.1) instead of (3.6) and got slightly poorer fits to the one-point spectra but the predicted coherences deviated not much from the US model with (3.6).

4.5. *The Lammefjord Experiment*

The purpose of the Lammefjord Experiment (Courtney 1988, LAMEX), which ran from the beginning of June 1987 to the end of June 1988, was to provide wind data suitable both as input for studies of dynamic loads on structures, especially wind turbines, and, as in this study, as a basis for the verification and improvement of atmospheric turbulence models.

4.6. *Description of LAMEX*

The experimental site was located at Lammefjord, a reclaimed, flat-bottomed fjord on the Danish island of Zealand. The surrounding land is used for agriculture and lies slightly below sea level. Because of difficulties with drainage, no buildings are found within 2.5 km in the direction of the prevailing southwesterly winds. In this direction the level did not vary more than one meter. The old sea bed is bounded by a drainage canal beyond which the terrain rises steeply with hills up to ~ 100 m roughly 4 km from the site. The change of roughness 2.5 km upstream of the masts will affect the turbulence measurements above ~ 25 m.

Three masts were erected in a vertical plane perpendicular to the prevailing southwesterly wind direction. Two were 30 m high and the third was 45 m. The position of the anemometers relative to the base of the 45 m mast is shown in table 3.

The cup anemometers used were the Risø model 70, which has a distance constant of about 1.7 m. At the wave numbers considered in this study the spectra are unaffected by the low-pass filtering by the cups. The omni-directional sonic anemometer at the top of the highest mast was a Kaijo-Denki model DAT-300. The sonic signal was recorded at 16 Hz and the cups (and some other instruments) were recorded at 8 Hz almost uninterrupted for a year, giving a body of data of approximately 12 Gbytes.

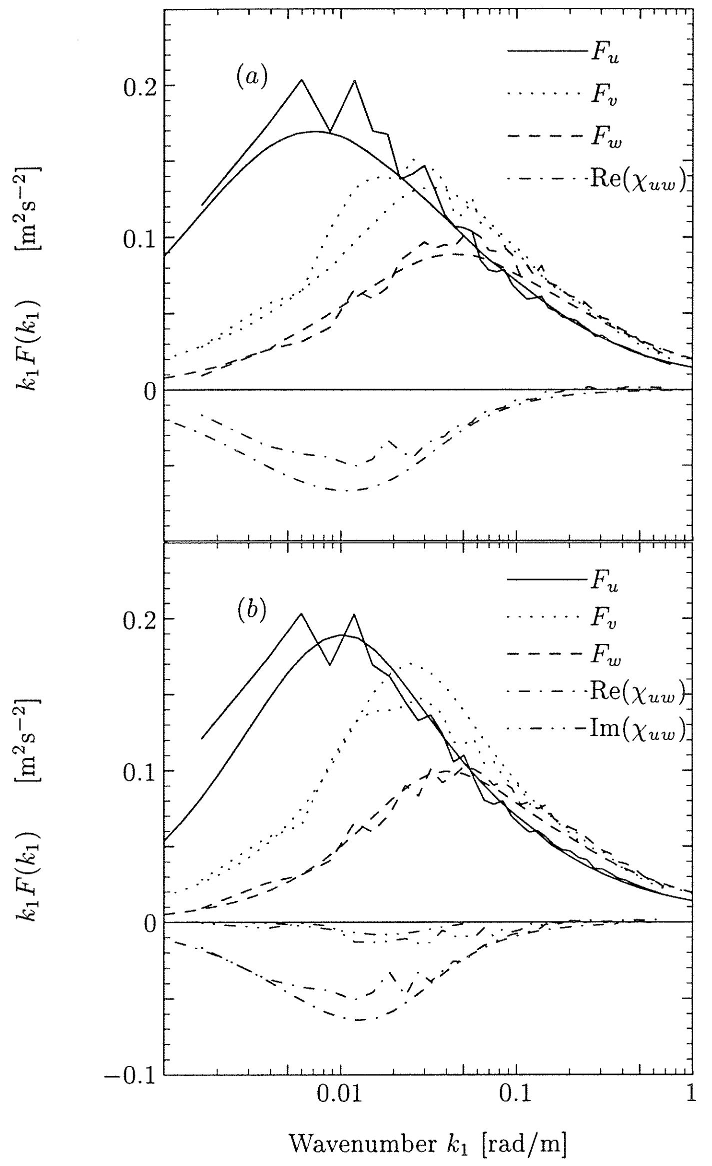

FIGURE 10. Fit of the model spectra (smooth lines) to the data (ragged lines) from the sonic of the Lammefjord Experiment at $z = 46$ m. The US model is shown in (*a*) US+B in (*b*). The values of the model parameters are given in table 1.

4.7. *Comparison with LAMEX data*

The Lammefjord experiment is not perfectly suited to test our model since the fitting of the one-point component spectra to the model is based on data from the sonic 46 m above the ground while the all the other instruments are at lower heights.

To test our model we have chosen a 10 hour run with mean wind speed around 11 ms^{-1} and direction very close to perpendicular to the mast array. The Richardson number is

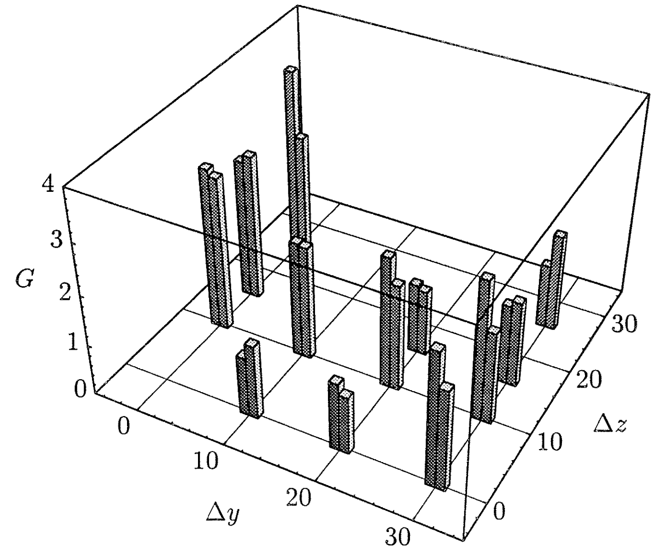

FIGURE 11. 'Goodness' of the predicted *uu*-coherences, G, according to (4.8) as a function of vertical and transversal separation. At each position $(\Delta y, \Delta z)$ the left bar refers to the US model while the right refers to the US+B model. Bars with G close to 1 represent the best predictions.

---

between 0 and 0.1 at $z = 21$ m estimated from measured velocity and temperature profiles. Even though the stratification is perhaps slightly stable it is assumed to be sufficiently close to neutral that our model applies. The three measured component spectra and the *uw*-cross-spectrum are shown in figure 10 together with the model fit. Again the models account well for the essential features of the spectra. The values of Γ are smaller compared to the Great Belt indicating that the turbulence at the Lammefjord site is more isotropic (see table 1). This may be explained by the limited fetch at the Lammefjord site.

Only instruments from 20 m and above are used to test the model because we consider it too crude to assume a linear wind profile from the sonic at 46 m down to 10 m.

From the parameters obtained from the fits in figure 10 we have predicted all possible coherences between the velocity components of the sonic and the *u*-components measured by the cups. The 'goodness', G, of the predicted *uu*-coherences is shown in figure 11 as a function of transversal and vertical separation for both the US model and the US+B model. It is seen that the models work well primarily for horizontal separations and that the US+B model generally gives slightly better predictions. The models predict by a small amount too large coherences for vertical separations. The consequences for the errors in load calculations on vertical structures depend on the shape of the excited modes. If the typical length scale of the mode shape is larger than the 'coherence decay length' the model will predict slightly too high loads.

The success of the *uv*- and *uw*-coherence predictions is shown in table 4. For the

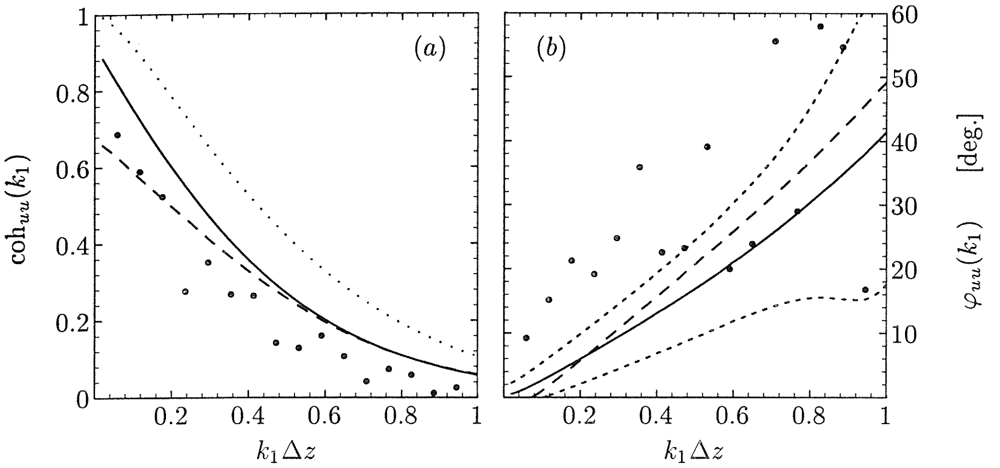

FIGURE 12. uu-coherence (a) and phase (b) for a vertical separation $\Delta z = 26$ m from LAMEX ($z_1 = 20$ m, $z_2 = 46$ m). The dots are measured coherences, the solid curve is the US prediction, the dashed is from the US+B model and the dotted curve is the isotropic inertial subrange prediction. The short-dashed curves in (b) are the theoretical 1-σ deviations of the phase from the US model according to (4.11).

	Δy	Δz	G	
	[m]	[m]	US	US+B
	20	16	1.9	1.7
uv	30	16	2.3	1.6
	30	26	2.3	1.9
	0	16	3.3	1.0
	0	26	3.3	1.5
uw	20	16	2.2	1.2
	30	16	2.0	2.1
	30	26	2.0	1.4

TABLE 4. 'Goodness' of the predicted uv- and uw-coherences, G, according to (4.8) for different horizontal and vertical separation, Δy and Δz. Predictions with G closest to one are the best predictions.

US model the coherences with predominantly horizontal separations again seem to be predicted best, but the US+B model seems to be superior to the US model.

We shall now look at two examples of predicted coherences represented in the bar chart in figure 11 and in table 4. The first is the uu-coherence and phase between the sonic at 46 m and a cup directly under the sonic at $z = 20$ m (see table 3) displayed in figure 12. This is a quite poor predictions ($G = 3.6$ for the US model, $G = 2.3$ for US+B); the models, especially the US, are seen to overestimate the coherence systematically.

The phase calculated from the same data is shown in figure 12(b), where the scatter is estimated using (4.11). A positive φ here means that the fluctuations at $z = 20$ m

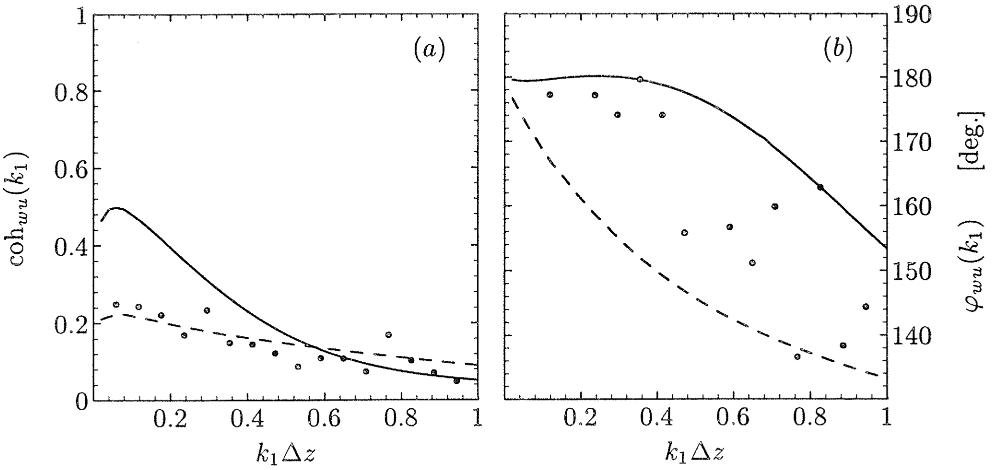

FIGURE 13. uw-coherence with w measured at $z = 46$ m and u at 20 m and with zero horizontal separation. See caption to figure 12.

come after the fluctuations at $z = 46$ m. The phase and the scatter are well predicted at the higher wave numbers while the phase is underestimated at the lowest wave numbers. The models make quite similar predictions in this case.

The last example (figure 13) shows coherence and phase predicted significantly differently by the two models. The coherence is predicted better by the US+B model which has $G = 1.5$ compared to $G = 3.3$ for the US model. The measured phases are between the two predictions.

5. Conclusion

We have investigated two slightly different models of the spectral tensor of neutral atmospheric surface layer turbulence which contain only three parameters: A length scale L, an eddy lifetime constant Γ and the spectral multiplier in the inertial subrange ($\alpha\varepsilon^{\frac{2}{3}}$). Both models crudely consider the effect of shear on turbulence by using the linearized and inviscid Navier–Stokes equation. The effect of the non-linear terms is taken into account by including considerations about the lifetime of eddies of different sizes. The simplest model is the Uniform Shear model (US) (§3.2) while the US+B model (§3.3) additionally attempts to take into account the effect of blocking by the surface.

We have used two experiments specially designed to measure the spatial structure of turbulence to test the models: The Great Belt Coherence Experiment measuring turbulence over water and the Lammefjord Experiment (LAMEX), which measures turbulence over an almost horizontally homogeneous terrain.

As mentioned in §2.2, since we have assumed a linear shear, we should only expect the spectral tensors to model eddies with sizes smaller than the scale over which the shear changes appreciably, which in the surface layer is the height above the ground, z. Because of the three adjustable parameters, however, the fit of the model to the *one-point* spectra is good well below $k_1 \sim 2\pi/z$. From these parameters virtually all second order

	σ_u^2/q^2	σ_v^2/q^2	σ_w^2/q^2	$-\langle uw\rangle/q^2$
Panofsky & Dutton (1984)	0.53	0.33	0.14	0.09
Other data (Maxey 1982)	0.53	0.28	0.19	0.14
Great Belt	0.54	0.31	0.15	0.11
US model (G.B. parameters)	0.51	0.30	0.19	0.13
US+B model (G.B. parameters)	0.46	0.34	0.20	0.11
Model of Maxey (1982)	0.59	0.34	0.07	0.14
LAMEX†	0.45	0.35	0.20	0.11
US model (LAMEX parameters)	0.47	0.31	0.22	0.13
US+B model (LAMEX parameters)	0.44	0.34	0.22	0.11

† Site is not completely homogeneous.

TABLE 5. Stress ratios from two references, our two experiment and some models. The parameters of the US and US+B models are given in table 1.

two point statistics, i.e. coherences, phases etc., are predicted satisfactorily from the models. Both models performs less well for vertical separations (e.g. figure 12) where the departure from a linear profile might be important.

There are only small differences in the predictions made by the US and US+B models, with the notable exception of coherences involving vertical velocity fluctuations where the US+B model is superior. For the predicted phases the situation is not that clear (see figures 9(*b*), 12(*b*) and 13(*b*)). Because the US+B model is more complex than the US model we recommend the latter for engineering purposes, except in cases where the coherence of vertical velocity fluctuations at low frequencies is of particular importance.

The two Great Belt Experiment gives a larger value of the lifetime parameter Γ than LAMEX (see table 1). The most plausible cause of the difference is a change of roughness 2.5 km upwind of the LAMEX site as discussed in §4.6 and §4.7.

This paper differ from previous studies of the application of rapid distortion theory to homogeneous shear flow (Maxey 1982; Townsend 1976; Lee & Hunt 1989) in two respects. Firstly, they do not incorporate 'eddy life time' in the spectral tensor models. Maxey's (1982) assumes that shear acts on all scales with the same strain in contrast to our model. This has the consequence that the cross-spectrum $F_{uw}(k_1)$ in the inertial subrange is proportional to $k_1^{-\frac{5}{3}}$ while our model predicts $k_1^{-\frac{7}{3}}$ in accordance with Wyngaard and Coté (1972) and that $F_w \ll F_u$ for $k_1 \to \infty$ in contrast to the present models which are isotropic for large k, i.e. $F_w = \frac{4}{3}F_u$ for $k_1 \to \infty$. In relation to this, if the parameters of the model of Maxey (1982) are adjusted to fit the observed shear stress ratio $-\langle uw\rangle/q^2 = 0.14$ (q^2 is $\sigma_u^2+\sigma_v^2+\sigma_w^2$) then the derived normalized variances of the three velocity components are not well predicted. In table 5 normalized variances and shear stresses are from homogeneous shear flow measurements and models are displayed. It is seen that a closer comparison is found than that by Maxey (1982). The model by Maxey (1982) predicts the ratio σ_v^2/σ_w^2 to be 4.9 while ours gives values in the range 1.4 to 1.7 in better agreement with data. The other difference from the previous studies is that we not only use one-point but also emphasize two-point statistics such as coherences and phases in our experimental validation.

Finally, it should be noted that we have no formal justification to apply rapid distortion theory to stationary and homogeneous flows. The reader may find discussions of this point elsewhere (Townsend 1976; Maxey 1982; Savill 1987; Hunt & Carruthers 1993). The purpose of paper is solely to present the models and make a detailed comparison with data.

The author acknowledges J. C. R. Hunt for suggesting the analysis in §3.3. I thank Dr. Michael S. Courtney and others at the Risø National Laboratory for the excellent experiments and A/S Storebæltsforbindelsen for financing the Great Belt Coherence Experiment. The author is grateful to Drs. Leif Kristensen and Peter Kirkegaard (both Risø) for many fruitful discussions and to Professor Steen Krenk of University of Aalborg for his useful comments to the manuscript. Thanks to suggestions from Drs. Jack Herring and Don Lenschow of the National Center for Atmospheric Research in Boulder, Colorado the manuscript has been improved in several ways. The author acknowledge the financial support from The Danish Research Academy during this study.

REFERENCES

BATCHELOR, G. K. 1953 *The theory of homogeneous turbulence*, Cambridge Monographs on Mechanics and Applied Mathematics, 197 pp.

CHANDRASEKHAR, S. 1950 The theory of axisymmetric turbulence, *Phil. Trans.* A **242**, 557–577.

COMTE-BELLOT, G. & CORRSIN, S. 1971 Simple Eulerian time correlation of full- and narrow-band velocity signals in grid-generated, 'isotropic' turbulence, *J. Fluid Mech.* **48**, 273–337.

COURTNEY, M. S. 1988 An atmospheric turbulence data set for wind turbine research. In *Wind Energy Conversion, Proceedings of the 1988 BWEA Wind Energy Conference* (ed. D. J. Milborrow), 89–94. Mech. Engng Publ.

DAVENPORT, A. G. 1977 The Prediction of the Response of Structures to Gusty Wind. In *Safety of Structures Under Dynamic Loading* (eds. I. Holland, D. Kavlie, G. Moe & R. Sigbjörnsson). Norwegian Institute of Technology, Trondheim, 257–284.

DAVIS, P. J. & RABINOWITZ, P. 1984 *Methods of numerical integration*, 2nd ed. Academic Press.

DERBYSHIRE, S. H. & HUNT, J. C. R. 1993 Structure of Turbulence in Stably Stratified Atmospheric Boundary Layers; Comparison of Large Eddy Simulations and Theoretical Models. In *Waves and Turbulence in Stably Stratified Flows* (ed S. D. Mobbs & J. C. King), 23–59. Clarendon.

DURBIN, P. A. 1978 Rapid distortion theory of turbulent flows. Ph.D. thesis, University of Cambridge.

GARTSHORE, I. S., DURBIN, P. A. & HUNT, J. C. R. 1983 The production of turbulent stress in a shear flow by irrotational fluctuations, *J. Fluid Mech.* **137**, 307–329.

HARRIS, I. 1970 The nature of the wind. *Proc. Seminar at Inst. Civil Engrs, June* 1970.

HUNT, J. C. R. 1973 A theory of turbulent flow round two-dimensional bluff bodies, *J. Fluid Mech.* **61**, 625–706.

HUNT, J. C. R. & CARRUTHERS, D. J. 1993 Rapid distortion theory and the 'problems' of turbulence, *J. Fluid Mech.* **212**, 497–532.

HUNT, J. C. R. & GRAHAM, J. M. R. 1978 Free-stream turbulence near plane boundaries, *J. Fluid Mech.* **84**, 209–235.

HUNT, J. C. R., MOIN, P., LEE, M., MOSER, R. D., SPALART, P., MANSOUR, N. N., KAIMAL, J. C. & GAYNOR, E. 1989 Cross Correlation and Length Scales in Turbulent Flows near Surfaces, *Advances in Turbulence*, **2**, 128–134, (eds. H.-H. Fernholz & H. E. Fiedler) Springer.

IZUMI, Y. 1971 Kansas 1968 field program data report, *Environmental Research Papers*, No. 379, AFCRL-72-0041, Air Force Cambridge Research Laboratories, Bedford, Massachusetts.

KÁRMÁN, T. VON 1948 Progress in the Statistical Theory of Turbulence, *Proc. National Akad. Sci.* **34**, 530–539.

KOOPMANS, L. H. 1974 *The Spectral Analysis of Time Series*, Academic.

KRISTENSEN, L. & JENSEN, N. O. 1979 Lateral coherence in isotropic turbulence and in the natural wind, *Boundary-Layer Meteorol.*, **17**, 353–373.

KRISTENSEN, L. & KIRKEGAARD, P. 1986 Sampling Problems with Spectral Coherence, *Risø Report No. R-526*, 63 pp.

KRISTENSEN, L. & KIRKEGAARD, P. 1987 Puff Kinematics, *Risø Report No. R-548*, 88 pp.

KRISTENSEN, L., LENSCHOW, D. H., KIRKEGAARD, P. & COURTNEY, M. S. 1989 The spectral velocity tensor for homogeneous boundary-layer turbulence, *Boundary-Layer Meteorol.*, **47**, 149–193.

LANDAU, L. D. & LIFSHITZ, E. M. 1987 *Fluid Mechanics*, vol. 6 in Course of Theoretical Physics, Pergamon.

LARSEN, A. (ed.) 1992 *Proc. Intl Symp. on Aerodynamics of Large Bridges*, 305 pp. Balkema.

LEE, M. J. & HUNT, J. C. R. 1989 The structure of sheared turbulence near a plane boundary, *7th Symp. on Turbulent Shear Flows*, Stanford.

LESIEUR, M. 1987 *Turbulence in fluids*, Martinus Nijhoff Publishers, 286 pp.

LUMLEY, J. L. 1970 *Stochastic Tools in Turbulence*, 194 pp. Academic.

MANN, J., KRISTENSEN, L. & COURTNEY, M. S. 1991 The Great Belt Coherence Experiment – A study of atmospheric turbulence over water, *Risø Report No. R-596*, 51 pp.

MAXEY, M. R. 1982 Distortion of turbulence in flows with parallel streamlines, *J. Fluid Mech.* **124**, 261–282.

PANOFSKY, H. A., LARKO, D., LIPSCHUTZ, R., STONE, G., BRADLEY, E. F., BOWEN, A. J. & HØJSTRUP, J. 1982 Spectra of velocity components over complex terrain *Quart. J. R. Met. Soc.*, **108**, 215–230.

PANOFSKY, H. A. & DUTTON, J. A. 1984 *Atmospheric Turbulence*, 397 pp. John Wiley & Sons.

PRESS, W. H., B. P. FLANNERY, S. A. TEUKOLSKY, & W. T. VETTERLING 1986 *Numerical Recipes*, 735 pp., Cambridge University Press.

SAVILL, A. M. 1987 Recent developments in rapid-distortion theory, *Ann. Rev. Fluid Mech.* **19**, 531–575.

SCHMIDT, H. & SCHUMANN, U. 1989 Coherent structure of the convective boundary layer derived from large-eddy simulations, *J. Fluid Mech.* **200**, 511–562.

SREENIVASAN, K. R. & NARASIMHA, R. 1978 Rapid distortion of axisymmetric turbulence, *J. Fluid Mech.* **84**, 497–516.

TENNEKES, H. & LUMLEY, J. L. 1972 *A First Course in Turbulence*, 300 pp. MIT Press.

TOWNSEND, A. A. 1976 *The Structure of Turbulent Shear Flow*, 2nd ed., Cambridge University Press, 429 pp.

WYNGAARD, J. C. & COTÉ, O. R. 1972 Co-spectral similarity in the atmospheric surface layer. *Quart. J. R. Met. Soc.*, **98**, 590–603.

Appendix A. Numerical methods

It does not take a great numerical effort to calculate one point spectra and co-variances from (2.7) with $\Delta y = \Delta z = 0$ and from (2.10). Two and three dimensional adaptive integration algorithms from the Risø Computer Library are used to these purposes. However, when Δy and Δz are just moderately large the standard adaptive integration algorithms become very inefficient. The problem with the numerical evaluation of (2.7) is that the integrand may vary rapidly, even if $\Phi_{ij}(\mathbf{k})$ itself is quite slowly varying. This means that a 2-dimensional adaptive integration routine will spend a lot of time mapping all the wiggles of the simple trigonometric function $\exp(\mathrm{i}(k_2\Delta y + k_3\Delta z))$.

In this appendix we give a fast and reliable method to evaluate the numerical double integral (2.7). For the sake of simplicity of the argument we assume $\Delta z = 0$ in (2.7). The idea is first, for a given k_1 (or frequency), to use a standard 1-dimensional adaptive integration routine to evaluate the function

$$f(k_1, k_2) = \int_{-\infty}^{\infty} \Phi_{ij}(\mathbf{k})\mathrm{d}k_3 \tag{A 1}$$

on a mesh in k_2. This mesh is constructed as follows:, x is chosen equidistantly on the interval $]-1, 1[$ and k_2 is given as $k_2 = k_{\mathrm{div}}x/(1-x)$, where k_{div} is $1/L$ if $k_1 < 1/L$ and $k_{\mathrm{div}} = k_1$ otherwise, where L is the length scale in the spectral tensor. Next we calculate

$$\chi_{ij}(k_1, \Delta y, 0) = \int_{-\infty}^{\infty} f(k_1, k_2)\exp(\mathrm{i}k_2\Delta y)\,\mathrm{d}k_2 \tag{A 2}$$

by the effective method given below. The method allows fast calculation of χ_{ij} for a range of Δy-values, when $f(k_1, k_2)$ is tabulated on the k_2-mesh.

A.1. *Integration of the product of a smooth function and an oscillating multiplier by use of non-local cubic spline*

This method generalizes Filon's Method (Davis & Rabinowitz, 1984) to an arbitrary mesh and combines is with the non-local cubic spline interpolation (Press *et al.*, 1986).

Let the function $y(x)$ be tabulated in the points x_j, $j = 1 \ldots N$ and let $y_j = y(x_j)$. We want to estimate the integral

$$\int_a^b y(x)W(x)\mathrm{d}x \tag{A 3}$$

where $W(x)$ is either $\cos(kx)$ or $\sin(kx)$ and $a = x_1$ and $b = x_N$. Suppose y is so smooth, that it is well approximated by a cubic spline. Then the second derivatives $y_j'' = y''(x_j)$ can by found easily in $O(N)$ operations (see Press *et al.*, 1986).

We start by estimating

$$\int_a^b y(x)dx \tag{A 4}$$

which is needed in our application. To integrate y on a subinterval $[x_j, x_{j+1}]$ we approximate y by the a cubic polynomial f determined by the non-local cubic spline interpolation routine (Press *et al.*, 1986) and use partial integration as follows

$$\begin{aligned}\int_{x_j}^{x_{j+1}} y(x)\mathrm{d}x &\approx \int_{x_j-\bar{x}}^{x_{j+1}-\bar{x}} f(x+\bar{x})\mathrm{d}x \\ &= [f(x+\bar{x})x]_{x_j-\bar{x}}^{x_{j+1}-\bar{x}} - \int_{x_j-\bar{x}}^{x_{j+1}-\bar{x}} f'(x+\bar{x})x\mathrm{d}x\end{aligned}$$

$$
\begin{aligned}
&= \left[f(x+\bar{x})x - \frac{1}{2}f'(x+\bar{x})x^2\right]_{x_j-\bar{x}}^{x_{j+1}-\bar{x}} \\
&\quad + \frac{1}{2}\int_{x_j-\bar{x}}^{x_{j+1}-\bar{x}} f''(x+\bar{x})x^2\mathrm{d}x \\
&= \left[f(x+\bar{x})x - \frac{1}{2}f'(x+\bar{x})x^2 + \frac{1}{6}f''(x+\bar{x})x^3\right]_{x_j-\bar{x}}^{x_{j+1}-\bar{x}} \\
&\quad - \frac{1}{6}\int_{x_j-\bar{x}}^{x_{j+1}-\bar{x}} f'''(x+\bar{x})x^3\mathrm{d}x, \qquad \text{(A 5)}
\end{aligned}
$$

where $\bar{x} = (x_j + x_{j+1})/2$. Since f''' is constant and x^3 is odd the last integral vanishes and we end up with

$$
\begin{aligned}
\int_{x_j}^{x_{j+1}} y(x)\mathrm{d}x \approx \frac{1}{48}\Big\{ & 24(y_{j+1}+y_j)(x_{j+1}-x_j) \\
& - 6(y'_{j+1}-y'_j)(x_{j+1}-x_j)^2 + (y''_{j+1}+y''_j)(x_{j+1}-x_j)^3\Big\}. \qquad \text{(A 6)}
\end{aligned}
$$

We can express $y'_{j+1} - y'_j$ as $\int_{x_j}^{x_{j+1}} f''(x)\mathrm{d}x$, and since the interpolating polynomial f is cubic, f'' is linear and we get

$$
y'_{j+1} - y'_j = \frac{(x_{j+1}-x_j)(y''_j + y''_{j+1})}{2} \qquad \text{(A 7)}
$$

Substituting (A 7) into (A 6) and summing over all the sub-intervals of $[a, b]$ we finally get the estimate

$$
\int_a^b y(x)\mathrm{d}x \approx \sum_{j=1}^{N-1} \frac{1}{2}(y_j + y_{j+1})(x_{j+1}-x_j) - \frac{1}{24}(y''_j + y''_{j+1})(x_{j+1}-x_j)^3. \qquad \text{(A 8)}
$$

We now estimate (A 3) in the same way as (A 5) by partial integration. For definiteness, we take $W(x) = \cos(kx)$:

$$
\begin{aligned}
\int_{x_j}^{x_{j+1}} y(x)\cos(kx)\mathrm{d}x \approx\ & \frac{1}{k}\left(y_{j+1}\sin(kx_{j+1}) - y_j\sin(kx_j)\right) \\
& + \frac{1}{k^2}\left(y'_{j+1}\cos(kx_{j+1}) - y'_j\cos(kx_j)\right) \\
& - \frac{1}{k^3}\left(y''_{j+1}\sin(kx_{j+1}) - y''_j\sin(kx_j)\right) \\
& - \frac{1}{k^4}y'''_{(j,j+1)}\left(\cos(kx_{j+1}) - \cos(kx_j)\right), \qquad \text{(A 9)}
\end{aligned}
$$

where $y'''_{(j,j+1)}$ means the (constant) third derivative of the interpolating polynomial on the interval $[x_j, x_{j+1}]$. Adding all terms and expressing $y'''_{(j,j+1)}$ in terms of the second derivative, which is given by the cubic spline, we end up with

$$
\begin{aligned}
\int_a^b y(x)\cos(kx)\mathrm{d}x \approx\ & \frac{1}{k}\left(y_N\sin(kb) - y_1\sin(ka)\right) \\
& + \frac{1}{k^2}\left(y'_N\cos(kb) - y'_1\cos(ka)\right) \\
& - \frac{1}{k^3}\left(y''_N\sin(kb) - y''_1\sin(ka)\right)
\end{aligned}
$$

k_1	0.01	0.1	1	10
$\chi_{11}^{\mathrm{ex}}(k_1,0,0)$	0.16362	0.16229	0.091838	0.0034963
$\chi_{11}^{\mathrm{num}}(k_1,0,0)$	0.16356	0.16224	0.091774	0.0034953
$\chi_{22}^{\mathrm{ex}}(k_1,0,0)$	0.081825	0.082482	0.084185	0.0046329
$\chi_{22}^{\mathrm{num}}(k_1,0,0)$	0.081812	0.082469	0.084166	0.0046324
$\chi_{33}^{\mathrm{ex}}(k_1,0,0)$	0.081825	0.082482	0.084185	0.0046329
$\chi_{33}^{\mathrm{num}}(k_1,0,0)$	0.081790	0.082446	0.084149	0.0046321

TABLE 6. Exact and calculated one point spectra for various wavenumbers k_1.

$$- \frac{1}{k^4} \sum_{j=1}^{N-1} \frac{y''_{j+1} - y''_j}{x_{j+1} - x_j} \left(\cos(kx_{j+1}) - \cos(kx_j)\right). \tag{A 10}$$

The first derivatives at the end points y'_1 and y'_N are either specified as a input to the cubic spline routine or the so-called *natural cubic spline*, where y''_1 and y''_N are equal to zero, is chosen, in which case the first derivatives in the end points are given by

$$y'_1 = \frac{y_2 - y_1}{x_2 - x_1} - \frac{(x_2 - x_1)y''_2}{6} \tag{A 11}$$

and

$$y'_N = \frac{y_N - y_{N-1}}{x_N - x_{N-1}} + \frac{(x_N - x_{N-1})y''_{N-1}}{6}. \tag{A 12}$$

In the case $W(x) = \sin(kx)$, which is used for calculating imaginary parts of cross-spectra, the estimate of (A 3) is

$$\begin{aligned} \int_a^b y(x)\sin(kx)\mathrm{d}x \approx & -\frac{1}{k}\left(y_N\cos(kb) - y_1\cos(ka)\right) \\ & + \frac{1}{k^2}\left(y'_N\sin(kb) - y'_1\sin(ka)\right) \\ & + \frac{1}{k^3}\left(y''_N\cos(kb) - y''_1\cos(ka)\right) \\ & - \frac{1}{k^4}\sum_{j=1}^{N-1}\frac{y''_{j+1} - y''_j}{x_{j+1} - x_j}\left(\sin(kx_{j+1}) - \sin(kx_j)\right). \end{aligned} \tag{A 13}$$

A.2. *Test of the numerical code*

The numerical code is tested by comparison to the analytical von Kármán spectra and coherences given in terms of modified Bessel functions (Harris 1970; Kristensen & Jensen 1979; Mann *et al.* 1991). Throughout the testing the relative precision of the 1-dimensional adaptive integration routine in (A 1) is set to 0.0002. The number of points in the k_2-mesh is 300. For $L = 1$, $\alpha\varepsilon^{2/3} = 1$ and $\Gamma = 0$ (i.e the isotropic the von Kármán tensor) exact and calculated one point spectra are given in Table 6 , where the superscript of χ corresponds to the *ex*act result or the *num*eric result. The relative error is on average 0.0003 and the maximum relative error for the tested wavenumbers is less than 0.0007. This error can for the present purpose be neglected.

For the same values of L and Γ we have calculated the coherence for three various values of the displacement: $D = 1/3, 1, 3$. The largest difference between the numerical

k_1	0.01	0.1	1	10
$\mathrm{coh}_{11}^{\mathrm{ex}}(k_1,\frac{1}{3},0)$	0.60653	0.60446	0.44721	0.00137
$\mathrm{coh}_{11}^{\mathrm{num}}(k_1,\frac{1}{3},0)$	0.60688	0.60482	0.44762	0.00137
$\mathrm{coh}_{11}^{\mathrm{ex}}(k_1,1,0)$	0.10628	0.10466	0.02490	0.00000
$\mathrm{coh}_{11}^{\mathrm{num}}(k_1,1,0)$	0.10635	0.10472	0.02489	0.00000
$\mathrm{coh}_{11}^{\mathrm{ex}}(k_1,3,0)$	0.00119	0.00120	0.00088	0.00000
$\mathrm{coh}_{11}^{\mathrm{num}}(k_1,3,0)$	0.00119	0.00120	0.00088	0.00000
$\mathrm{coh}_{22}^{\mathrm{ex}}(k_1,\frac{1}{3},0)$	0.74897	0.75039	0.74053	0.02216
$\mathrm{coh}_{22}^{\mathrm{num}}(k_1,\frac{1}{3},0)$	0.74921	0.75064	0.74075	0.02218
$\mathrm{coh}_{22}^{\mathrm{ex}}(k_1,1,0)$	0.28893	0.29108	0.25742	0.00000
$\mathrm{coh}_{22}^{\mathrm{num}}(k_1,1,0)$	0.28902	0.29117	0.25748	0.00000
$\mathrm{coh}_{22}^{\mathrm{ex}}(k_1,3,0)$	0.00911	0.00934	0.00398	0.00000
$\mathrm{coh}_{22}^{\mathrm{num}}(k_1,3,0)$	0.00911	0.00934	0.00399	0.00000
$\mathrm{coh}_{33}^{\mathrm{ex}}(k_1,\frac{1}{3},0)$	0.47919	0.48290	0.52584	0.00470
$\mathrm{coh}_{33}^{\mathrm{num}}(k_1,\frac{1}{3},0)$	0.47960	0.48331	0.52629	0.00470
$\mathrm{coh}_{33}^{\mathrm{ex}}(k_1,1,0)$	0.01314	0.01504	0.06792	0.00000
$\mathrm{coh}_{33}^{\mathrm{num}}(k_1,1,0)$	0.01315	0.01505	0.06798	0.00000
$\mathrm{coh}_{33}^{\mathrm{ex}}(k_1,3,0)$	0.02703	0.02463	0.00000	0.00000
$\mathrm{coh}_{33}^{\mathrm{num}}(k_1,3,0)$	0.02705	0.02465	0.00000	0.00000

TABLE 7. Exact and calculated coherences for various values of the displacement Δy and wavenumber k_1.

and exact values (see table 7) is 0.0004 (we do not use relative error, because the coherence is sometimes zero). This error is again too small to have any significance in the present work.

Appendix B. Derivation of (3.11) and (3.29)

In this appendix we first derive the linearized and Fourier transformed inviscid Navier-Stokes equation (3.11) in some detail. This has been done elsewhere (Townsend 1976, and references therein), but I would like to include a step-by-step derivation here.

Secondly, we include a explicit derivation of (3.29), although somewhat similar deductions appear in other publications (Durbin 1978; Gartshore *et al.* 1983).

B.1. *Derivation of (3.11)*

To get an equation for the velocity components we start by taking the divergence on both sides of the Navier-Stokes equation (3.8) and after decomposition in means and fluctuations according to (3.7) we get

$$-\rho\left(\frac{\partial U_i}{\partial x_j}\frac{\partial U_j}{\partial x_i}+2\frac{\partial U_i}{\partial x_j}\frac{\partial u_j}{\partial x_i}+\frac{\partial u_i}{\partial x_j}\frac{\partial u_j}{\partial x_i}\right)=\nabla^2 p. \tag{B 1}$$

The first term containing gradients of the mean flow is zero because of (2.13) and the non-linear term in $\boldsymbol{u}$ is neglected (but is later crudely modelled as discussed in §3). Taking the Fourier transform of the resulting equation we get

$$\rho\left(2\frac{\partial U_j}{\partial x_i}\mathrm{i}k_j\mathrm{d}Z_i(\boldsymbol{k})\right)=k^2\mathrm{d}\Pi(\boldsymbol{k}), \tag{B 2}$$

where the scalar field $\Pi(\boldsymbol{k})$ is the Fourier transform of the pressure field:

$$p(\boldsymbol{x})=\int \mathrm{e}^{\mathrm{i}\boldsymbol{k}\cdot\boldsymbol{x}}\mathrm{d}\Pi(\boldsymbol{k}).$$

Using (3.7) in (3.8) we get

$$\frac{\mathrm{D}u_i}{\mathrm{D}t}+u_j\frac{\partial U_i}{\partial x_j}+U_j\frac{\partial U_i}{\partial x_j}+u_j\frac{\partial u_i}{\partial x_j}=-\frac{1}{\rho}\frac{\partial p}{\partial x_i}+\nu\nabla^2\tilde{\boldsymbol{u}} \tag{B 3}$$

where $\mathrm{D}/\mathrm{D}t$ is defined in the main text. Equation (2.13) impies that the third term is zero. Again, the non-linear term on the left hand side is neglected. On the right hand side the last term is negligible since the Reynolds number of the neutral atmospheric surface layer is high for the z's of interest and we are only interested in the larger scales of the turbulence.

Townsend (1976) uses this last linear term to model the non-linear terms by substituting the molecular viscosity ν by a 'turbulent viscosity' or 'effective viscosity', ν_{turb}. We use the life time concept, as illustrated in §3.1, to model the non-linear terms.

To find the Fourier representation of the first term in (B 3), we note that because of incompressibility of the mean flow

$$\frac{\partial U_j}{\partial x_k}\frac{\partial(x_k u_i)}{\partial x_j}=\frac{\partial U_j}{\partial x_k}\left(\delta_{kj}u_i+x_k\frac{\partial u_i}{\partial x_j}\right)=\frac{\partial U_j}{\partial x_k}x_k\frac{\partial u_i}{\partial x_j}=U_j\frac{\partial u_i}{\partial x_j}.$$

The Fourier representation of the term $\partial(x_k u_i)/\partial x_j=\partial/\partial x_j\left(x_k\int\exp(\mathrm{i}\boldsymbol{k}\cdot\boldsymbol{x})\mathrm{d}Z_i(\boldsymbol{k},t)\right)$ is transformed as follows:

$$\begin{aligned}\frac{\partial}{\partial x_j}\left(x_k\int \mathrm{e}^{\mathrm{i}\boldsymbol{k}\cdot\boldsymbol{x}}\mathrm{d}Z_i\right)&=\frac{\partial}{\partial x_j}\int\frac{1}{\mathrm{i}}\frac{\partial}{\partial k_k}\mathrm{e}^{\mathrm{i}\boldsymbol{k}\cdot\boldsymbol{x}}\mathrm{d}Z_i\\&=-\frac{\partial}{\partial x_j}\int\frac{1}{\mathrm{i}}\mathrm{e}^{\mathrm{i}\boldsymbol{k}\cdot\boldsymbol{x}}\frac{\partial\mathrm{d}Z_i}{\partial k_k}=-\int k_j\mathrm{e}^{\mathrm{i}\boldsymbol{k}\cdot\boldsymbol{x}}\frac{\partial\mathrm{d}Z_i}{\partial k_k},\end{aligned}$$

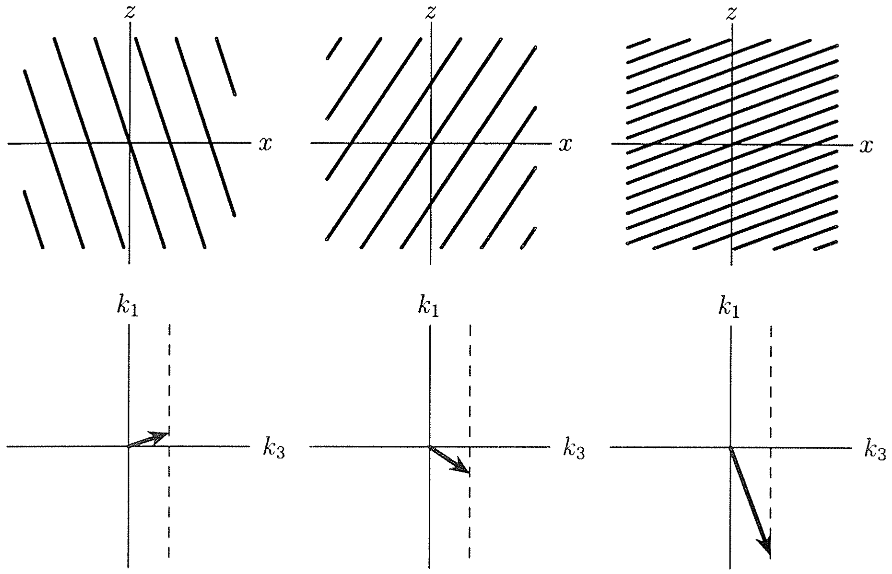

$\beta = 0$ $\beta = 1$ $\beta = 3$

FIGURE 14. Advection of a wave by linear shear in physical space (upper plots) and in Fourier space (lower plot) according to (3.9) with $\partial U_j/\partial x_k = \delta_{j1}\delta_{k3}\mathrm{d}U/\mathrm{d}z$, i.e vertical shear. Note that k_1 (and k_2) is constant in time.

---

where we have used partial integration. The averaged total derivative can therefore be written as

$$\frac{\mathrm{D}u_i(\boldsymbol{x},t)}{\mathrm{D}t} = \int \mathrm{e}^{\mathrm{i}\boldsymbol{k}\cdot\boldsymbol{x}} \left\{ \frac{\partial \mathrm{d}Z_i(\boldsymbol{k},t)}{\partial t} - \frac{\partial U_j}{\partial x_k} k_j \frac{\partial \mathrm{d}Z_i(\boldsymbol{k},t)}{\partial k_k} \right\}.$$

Interpreting the rate of change of wave number, $\mathrm{d}k_k/\mathrm{d}t$, by

$$\frac{\mathrm{d}k_k}{\mathrm{d}t} = -k_j \frac{\partial U_j}{\partial x_k} \tag{3.9}$$

the Fourier representation of the averaged total derivative of the velocity field may be written as

$$\frac{\mathrm{D}u_i(\boldsymbol{x},t)}{\mathrm{D}t} = \int \mathrm{e}^{\mathrm{i}\boldsymbol{k}\cdot\boldsymbol{x}} \left\{ \left(\frac{\partial}{\partial t} + \frac{dk_k}{dt}\frac{\partial}{\partial k_k} \right) \mathrm{d}Z_i(\boldsymbol{k},t) \right\} = \int \mathrm{e}^{\mathrm{i}\boldsymbol{k}\cdot\boldsymbol{x}} \left\{ \frac{\mathrm{D}\mathrm{d}Z_i(\boldsymbol{k},t)}{\mathrm{D}t} \right\}, \tag{B 4}$$

where we have implicitly defined $\mathrm{D}/\mathrm{D}t$ acting on a function of wavenumber and time. Figure 14 illustrates the connection between advection in physical space and in Fourier space shown in (3.9) and (B 4). Combining (B 4) with the linearized version of (B 3) and substituting the pressure according to (B 2) we get

$$\frac{\mathrm{D}\mathrm{d}Z_i(\boldsymbol{k},t)}{\mathrm{D}t} = \frac{\mathrm{d}U}{\mathrm{d}z} \left\{ -\delta_{i1} + 2\frac{k_i k_1}{k^2} \right\} \mathrm{d}Z_3(\boldsymbol{k},t). \tag{3.11}$$

B.2. *Derivation of (3.29)*

The initial conditions (3.25) and (3.26) has been derived by Hunt (1973) and Hunt & Graham (1978) for a sudden introduction of the surface/ground at $\beta = 0$. We are now going to investigate the development of turbulence in the presence of linear shear *and* the surface using rapid distortion theory. The solution for the third component (3.27) is found in Gartshore, Durbin & Hunt (1983). I have not, however, been able to find the exact derivation or explicit results from (3.29) and to the end of §3.3 anywhere although it must have been used by Lee & Hunt (1989).

Taking the curl of the linearized momentum equation we get

$$\frac{\mathrm{D}\boldsymbol{\omega}}{\mathrm{D}t} = \boldsymbol{\Omega} \cdot \nabla \boldsymbol{u} + \boldsymbol{\omega} \cdot \nabla \boldsymbol{U}, \tag{B 5}$$

where $\boldsymbol{\Omega}$ and $\boldsymbol{\omega}$ are the mean and the fluctuating part of the vorticity. Writing out the two first components and using the definition of β (3.12) we get the form (3.28), which — since it is linear — is valid for the unblocked and blocked flows. From the first equation in (3.28) we shall now derive the second component of the velocity field from the third (vertical).

First we expand the total derivative and Fourier transform in the two homogeneous directions (x and y):

$$\frac{\partial}{\partial \beta}\left(\mathrm{i}k_2 \mathrm{d}\mathcal{Z}_3^S - \frac{\partial \mathrm{d}\mathcal{Z}_2^S}{\partial z}\right) + \mathrm{i}k_1 z \left(\mathrm{i}k_2 \mathrm{d}\mathcal{Z}_3^S - \frac{\partial \mathrm{d}\mathcal{Z}_2^S}{\partial z}\right) = \mathrm{i}k_1 \mathrm{d}\mathcal{Z}_2^S. \tag{B 6}$$

We have already solved for $\mathrm{d}\mathcal{Z}_3^S$ (3.27) and guess a solution of (B 6) of the form

$$\mathrm{d}\mathcal{Z}_2^S(z,\beta) = \mathrm{i}\frac{k_2}{\kappa}\mathrm{e}^{-z\kappa} \int_{k_3} \left(1 - \frac{k^2}{2\kappa^2}\mathrm{e}^{\mathrm{i}k_3 z} Q_s(z,\beta)\right) \mathrm{d}Z_3(\boldsymbol{k},\beta), \tag{B 7}$$

where $Q_s(z,\beta)$ is a function to be determined. To obtain Q_s we first calculate

$$\begin{aligned}\frac{\partial \mathrm{d}\mathcal{Z}_2^S}{\partial z} &= -\mathrm{i}k_2 \mathrm{e}^{-z\kappa} \int_{k_3} \left\{\left(1 - \frac{k^2}{2\kappa^2}\mathrm{e}^{\mathrm{i}k_3 z} Q_s\right) + \frac{k^2}{2\kappa^3}\mathrm{e}^{\mathrm{i}k_3 z}\left(\mathrm{i}k_3 Q_s + \frac{\partial Q_s}{\partial z}\right)\right\} \mathrm{d}Z_3(\boldsymbol{k},\beta) \\ &= -\mathrm{i}k_2 \mathrm{e}^{-z\kappa} \int_{k_3} \left\{1 + \mathrm{i}\frac{k^2}{2\kappa^3}\mathrm{e}^{\mathrm{i}k_3 z}\psi\right\} \mathrm{d}Z_3(\boldsymbol{k},\beta),\end{aligned} \tag{B 8}$$

where

$$\psi \equiv (\mathrm{i}\kappa + k_3) Q_s - \mathrm{i}\frac{\partial Q_s}{\partial z} \tag{B 9}$$

is defined for notational convenience. The parenthesis in (B 6) is then by (3.27)

$$\begin{aligned}\mathrm{i}k_2 \mathrm{d}\mathcal{Z}_3^S - \frac{\partial \mathrm{d}\mathcal{Z}_2^S}{\partial z} &= -\frac{k_2 \mathrm{e}^{-z\kappa}}{2\kappa^3} \int_{k_3} \mathrm{e}^{\mathrm{i}k_3 z} k^2 \psi \mathrm{d}Z_3(\boldsymbol{k},\beta) \\ &\overset{(3.14)}{=} -\frac{k_2 \mathrm{e}^{-z\kappa}}{2\kappa^3} \int_{k_3} \mathrm{e}^{\mathrm{i}k_3 z} k_0^2 \psi \mathrm{d}Z_3(\boldsymbol{k}_0, 0)\end{aligned} \tag{B 10}$$

The left hand side of (B 6) thus becomes

$$\begin{aligned}\mathrm{L.H.S} &= -\frac{k_2 \mathrm{e}^{-z\kappa}}{2\kappa^3} \int_{k_3} \left\{\frac{\partial}{\partial \beta}\left(\mathrm{e}^{\mathrm{i}k_3 z}\psi\right) k_0^2 + \mathrm{i}k_1 z \mathrm{e}^{\mathrm{i}k_3 z}\psi k_0^2\right\} \mathrm{d}Z_3(\boldsymbol{k}_0, 0) \\ &= -\frac{k_2 \mathrm{e}^{-z\kappa}}{2\kappa^3} \int_{k_3} \mathrm{e}^{\mathrm{i}k_3 z} \frac{\partial \psi}{\partial \beta} k_0^2 \mathrm{d}Z_3(\boldsymbol{k}_0, 0),\end{aligned} \tag{B 11}$$

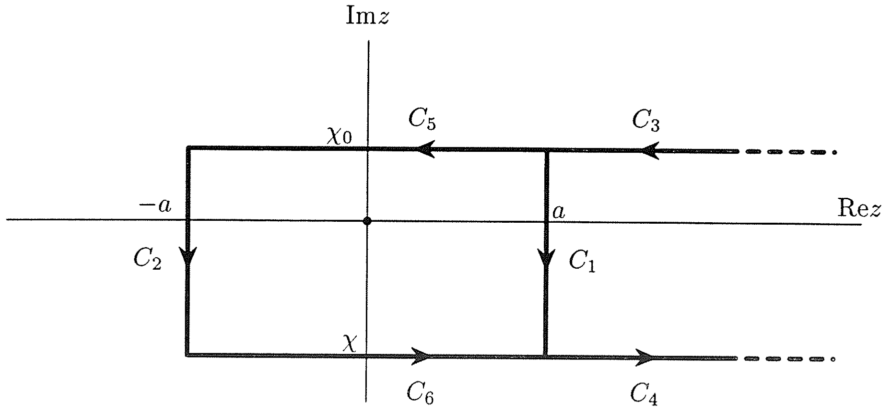

FIGURE 15. Contours integral paths. The curves C_3 and C_5 begin at real part $+\infty$ and end at (a, χ_0) and $(-a, \chi_0)$, respectively. C_4 and C_6 begin at (a, χ) and $(-a, \chi)$ and go toward real part ∞.

---

because (3.9) implies $\frac{\partial}{\partial\beta}\exp(\mathrm{i}k_3 z) = -\mathrm{i}k_1 z\exp(\mathrm{i}k_3 z)$. Using (B 7) on the right hand side of (B 6) gives

$$\text{R.H.S} = -\frac{k_2 \mathrm{e}^{-z\kappa}}{2\kappa^3}\int_{k_3}\left(2\kappa^2 k_1 \frac{k_0^2}{k^2} - k_1 k_0^2 \mathrm{e}^{\mathrm{i}k_3 z} Q_s\right)\mathrm{d}Z_3(\boldsymbol{k}_0, 0). \tag{B 12}$$

Equating (B 11) and (B 12) we see that if Q_s obeys

$$\frac{\partial\psi}{\partial\beta} = \frac{2\kappa^2 k_1}{k^2}\mathrm{e}^{-\mathrm{i}k_3 z} - k_1 Q_s \tag{B 13}$$

then we have found a particular solution to (B 6). We postulate

$$Q_s = 2\kappa\mathrm{i}\int_{k_{30}}^{k_3}\frac{\mathrm{e}^{-\mathrm{i}k_3' z}}{\kappa^2 + k_3'^2}\mathrm{d}k_3' \tag{B 14}$$

is a solution and we are now going to show that it is indeed so. The derivative of Q_s with respect to z is

$$\frac{\partial Q_s}{\partial z} = 2\kappa\mathrm{i}\int_{k_{30}}^{k_3}(-\mathrm{i})\frac{k_3'\mathrm{e}^{-\mathrm{i}k_3' z}}{\kappa^2 + k_3'^2}\mathrm{d}k_3', \tag{B 15}$$

and ψ becomes

$$\psi = 2\kappa\mathrm{i}\int_{k_{30}}^{k_3}\frac{(\mathrm{i}\kappa + k_3 - k_3')\mathrm{e}^{-\mathrm{i}k_3' z}}{\kappa^2 + k_3'^2}\mathrm{d}k_3'. \tag{B 16}$$

Differentiating ψ with respect to β we now get (B 13). In order to obey the initial conditions (3.26) we see that Q_s must be zero for $\beta = 0$. This follows clearly from (B 14).

In order to complete the solution we shall express Q_s (B 14) in terms of exponential integral functions. Using the substitutions $\chi = k_3 z$, $\chi_0 = k_{30} z$ and $a = \kappa z$, (B 14) may be written as

$$Q_s = 2\mathrm{i}a \int_{\chi_0}^{\chi} \frac{\mathrm{e}^{-\mathrm{i}x}}{a^2 + x^2}\mathrm{d}x$$
$$= \mathrm{i}\left\{\mathrm{e}^{a} \int_{\chi_0}^{\chi} \frac{\mathrm{e}^{-a-\mathrm{i}x}}{a + \mathrm{i}x}\mathrm{d}x - \mathrm{e}^{-a} \int_{\chi_0}^{\chi} \frac{\mathrm{e}^{a-\mathrm{i}x}}{-a + \mathrm{i}x}\mathrm{d}x\right\}, \tag{B 17}$$

or more compactly written

$$Q_s = \mathrm{e}^{a} \int_{C_1} \frac{\mathrm{e}^{-z}}{z}\mathrm{d}z - \mathrm{e}^{-a} \int_{C_2} \frac{\mathrm{e}^{-z}}{z}\mathrm{d}z, \tag{B 18}$$

where the contours are defined in figure 15. Cauchy's integral formula immediately gives

$$\int_{C_1} = -\int_{C_3+C_4} \quad \text{and} \quad \int_{C_2} = 2\pi \mathrm{i} H(-\chi_0\chi) - \int_{C_5+C_6} \tag{B 19}$$

because the lone pole in $(0, 0)$ of $\exp(-z)/z$ has *residue* 1 (H is the Heaviside function). For the integrals along C_3, C_4, C_5 and C_6 we use the definition of the exponential integral function to obtain

$$Q_s = \mathrm{e}^{a}\left[E_1(a + \mathrm{i}\chi_0) - E_1(a + \mathrm{i}\chi)\right] - \mathrm{e}^{-a}\left[2\pi\mathrm{i}H(-\chi_0\chi) + E_1(-a + \mathrm{i}\chi_0) - E_1(-a + \mathrm{i}\chi)\right] \tag{B 20}$$

from which (3.31) derives ($Q = \exp(\mathrm{i}k_3 z)Q_s$).

The first component of the flow can most easily be found from the assumption of incompressibility:

$$\mathrm{i}k_1 \mathrm{d}\mathcal{Z}_1^S(z,\beta) + \mathrm{i}k_2 \mathrm{d}\mathcal{Z}_2^S(z,\beta) + \frac{\partial}{\partial z}\mathrm{d}\mathcal{Z}_3^S(z,\beta) = 0 \tag{B 21}$$

Because of (3.25) the last term in the left hand side equals $\kappa \mathrm{e}^{-\kappa z}\mathrm{d}\mathcal{Z}_3(0,\beta)$ so

$$\mathrm{d}\mathcal{Z}_1^S(z,\beta) = -\frac{\kappa \mathrm{e}^{-\kappa z}\mathrm{d}\mathcal{Z}_3(0,\beta) + \mathrm{i}k_2 \mathrm{d}\mathcal{Z}_2^S(z,\beta)}{\mathrm{i}k_1}. \tag{B 22}$$

We now introduce (3.29) for $i = 2$ in this equation and get

$$\mathrm{d}\mathcal{Z}_1^S(z,\beta) = \mathrm{i}\frac{\kappa}{k_1}\mathrm{e}^{-\kappa z}\mathrm{d}\mathcal{Z}_3(0,\beta) - \mathrm{i}\frac{k_2^2}{k_1\kappa}\mathrm{e}^{-\kappa z}\left(1 - \frac{k^2}{2\kappa^2}Q(z)\right)\mathrm{d}\mathcal{Z}_3(0,\beta)$$
$$= \mathrm{i}\frac{k_1}{\kappa}\mathrm{e}^{-\kappa z}\mathrm{d}\mathcal{Z}_3(0,\beta) + \mathrm{i}\mathrm{e}^{-\kappa z}\frac{k_2^2 k^2}{2\kappa^3 k_1}Q(z)\mathrm{d}\mathcal{Z}_3(0,\beta) \tag{B 23}$$

from which (3.29) for $i = 1$ follows.

The solution (B 14) has been guessed as follows: Rearranging the terms in (B 6) we get

$$\frac{\partial^2 \mathrm{d}\mathcal{Z}_2^S}{\partial\beta\partial z} + \mathrm{i}k_1 z\frac{\partial \mathrm{d}\mathcal{Z}_2^S}{\partial z} + \mathrm{i}k_1 \mathrm{d}\mathcal{Z}_2^S = \mathrm{i}k_2\frac{\partial \mathrm{d}\mathcal{Z}_3^S}{\partial\beta} - zk_1k_2\mathrm{d}\mathcal{Z}_3^S. \tag{B 24}$$

This inhomogeneous, linear, partial differential equation can be solved by Fourier transforming in β:

$$\mathrm{i}(\omega + k_1 z)\frac{\partial \mathrm{d}\mathcal{Z}_2^S}{\partial z} + \mathrm{i}k_1 \mathrm{d}\mathcal{Z}_2^S = k_2(\omega + k_1 z)\mathrm{e}^{-\kappa z}\mathrm{d}\mathcal{Z}_3(k_1, k_2, 0, \omega), \tag{B 25}$$

where the solution for $\mathrm{d}\mathcal{Z}_3^S(z,\beta)$ (3.27) is used, and where any missing arguments in $\mathrm{d}\mathcal{Z}_i$ or $\mathrm{d}\mathcal{Z}_i^S$, such as k_1, k_2, z or ω, is understood. The equation, now just an ordinary linear differential equation, can be solved by standard methods:

$$\mathrm{d}\mathcal{Z}_2^S(z,\omega) = \mathrm{i}\frac{k_2}{\kappa}\mathrm{e}^{-\kappa z}\mathrm{d}\mathcal{Z}_3(0,\omega) + \frac{\mathrm{i}k_1 k_2 \mathrm{d}\mathcal{Z}_3(0,\omega)\mathrm{e}^{-\kappa z}/\kappa^2 + C(\omega)}{\omega + k_1 z} \tag{B 26}$$

where C in an arbitrary function of ω. A particular solution is thus

$$\mathrm{d}\mathcal{Z}_2^S(z,\beta) = \mathrm{i}\frac{k_2}{\kappa}\mathrm{e}^{-\kappa z}\mathrm{d}\mathcal{Z}_3(0,\beta) + \mathrm{i}\frac{k_1 k_2}{\kappa^2}\mathrm{e}^{-\kappa z}\left(\mathrm{d}\mathcal{Z}_3(z=0) * \mathcal{H}\right)(\beta), \tag{B 27}$$

where $*$ means convolution, $C(\omega) \equiv 0$ is chosen and $\mathcal{H}$ is the inverse Fourier transform of $(\omega + k_1 z)^{-1}$:

$$\mathcal{H}(\beta) = \begin{cases} \frac{\mathrm{i}}{2}\mathrm{e}^{-\mathrm{i}k_1 z\beta} & \beta > 0 \\ 0 & \beta = 0 \\ -\frac{\mathrm{i}}{2}\mathrm{e}^{-\mathrm{i}k_1 z\beta} & \beta < 0 \end{cases} \tag{B 28}$$

Calculation of the convolution in (B 27) leads to an equation from which the particular solution (3.29) for $i = 2$ can be guessed.

PART IB:

Applications of the spectral tensor

By JAKOB MANN
Risø National Laboratory, 4000 Roskilde, Denmark

Three applications of the spectral tensor models in Part IA are presented. The first application concerns simulation of a three-dimensional turbulent velocity field that has the second order statistics of the model in Part IA. The simulations can be used for dynamic load calculations on wind turbines, bridges, masts etc. The simulation algorithm is fast and simple to implement. The second investigates the attenuation of momentum flux measurements done with displaced sensors. Specifically, the 'K' style sonic array is analyzed. The spectral tensor model of Part IA is especially well suited for this, because it models the uw-cross-spectrum correctly with a $-\frac{7}{3}$ power law in the inertial subrange. The last application in this part uses the tensor model to analyze turbulence generated in a boundary layer wind tunnel. It comes as no surprise that the wind tunnel turbulence is more isotropic compared to the atmospheric turbulence, but methods are suggested to correct for this discrepancy in calculation of dynamic loads on a bridge.

1. Fourier simulation of a non-isotropic wind field model†

Realistic modeling of three-dimensional wind fields has become important in calculation of dynamic loads on some spatially extended structures, such as large bridges, towers and wind turbines. For some structures the along wind component of the of the turbulent flow is important while for others the vertical velocity fluctuations give rise to loads. There may even be structures where combinations of velocity fluctuations in different direction are of importance.

Most methods that have been developed to simulate the turbulent wind field are based on one-point (cross-)spectra and two-point cross-spectra. Here a method is described which builds on the model of the *spectral tensor* for atmospheric surface layer turbulence at high wind speeds developed in Part IA (the US model). Although the tensor does not in principle contain more information than the cross-spectra, it leads to a more natural and direct representation of the three-dimensional turbulent flow. As described in Part IA the basis of the model is an application of rapid distortion theory, which implies a linearization of the Navier-Stokes equation, combined with considerations of eddy life times. The physical considerations are quite crude, but the tensor contains essential aspects of the second order structure of atmospheric turbulence. The tensor model has

---

† Parts of this section appear in the proceedings of the 6th International Conference on Structural Safety and Reliability, ICOSSAR '93, held in Innsbruck. Professor Steen Krenk of University of Aalborg coauthored that paper.

been checked and calibrated with data from different experiments made for estimation of wind loads on a large suspension bridge and on horizontal axis wind turbines.

The wind field can be represented as a generalized Fourier-Stieltjes integral of its spectral components. The necessary factorization (i.e., 'square root') of the spectral tensor can be accomplished in closed form. A numerical simulation algorithm is obtained by recasting the Fourier representation of the wind field in discrete frequency/wavenumber space. The method is considerably faster and simpler than methods based on cross-spectra. Shinozuka and Jan (1972) suggested a quite similar method in general terms, but lack of a realistic spectral tensor of the turbulence in the atmospheric surface layer has prevented its use in wind engineering. The discretization imposes two requirements: If either the width or the height of the domain of the simulated field is not much larger than the length scale of the turbulence care must be taken to represent the energy of the largest scales. Secondly, the space domain must have a large enough margin around the structure of interest in order to avoid effects of the imposed periodicity.

1.1. *Definitions and preliminaries*

The notation used in this part is presented in §IA.2.1, so we shall only refresh the most basic concepts.

The atmospheric turbulent velocity field is denoted by $\tilde{\boldsymbol{u}}(\boldsymbol{x})$, where $\boldsymbol{x} = (x_1, x_2, x_3) = (x, y, z)$ is a right-handed coordinate system with the x-axis in the direction of the mean wind field and z as the vertical axis. The fluctuations about the mean wind field, $\boldsymbol{u}(\boldsymbol{x}) = (u_1, u_2, u_3) = (u, v, w) = \tilde{\boldsymbol{u}}(\boldsymbol{x}) - (U(z), 0, 0)$, are assumed to be homogeneous in space, which is often the case in the horizontal directions but is only a crude approximation in the vertical. Since we are interested in shear generated turbulence the mean wind field is allowed to vary as a function of z.

We shall use *Taylor's frozen turbulence hypothesis* (see e.g. Panofsky & Dutton, 1984) to interpret time series as 'space series' and to change between frequency and wavenumber. Since the mean wind speed is not constant in space, the wind speed U in the Taylor relation $\tilde{\boldsymbol{u}}(x, y, z) = \tilde{\boldsymbol{u}}(-Ut, y, z)$ must chosen as a vertical average of $U(z)$.

We only aim at simulating turbulence which has the right second order statistics, such as variances, cross-spectra etc. The velocity field is otherwise assumed to be Gaussian, which is not a bad approximation for strong winds. All second order statistics can be derived from the covariance tensor or its Fourier transform, the spectral tensor:

$$\Phi_{ij}(\boldsymbol{k}) = \frac{1}{(2\pi)^3} \int R_{ij}(\boldsymbol{r}) \exp(-\mathrm{i}\boldsymbol{k} \cdot \boldsymbol{r}) \mathrm{d}\boldsymbol{r}, \tag{1.1}$$

where $\int \mathrm{d}\boldsymbol{r} \equiv \int_{-\infty}^{\infty} \int_{-\infty}^{\infty} \int_{-\infty}^{\infty} \mathrm{d}r_1 \mathrm{d}r_2 \mathrm{d}r_3$. The spectral tensor is the basis of the Fourier simulation and we shall only briefly describe the non-isotropic tensor model in §1.2, because it is described in detail in Part IA.

The stochastic velocity field can be represented in terms of a generalized stochastic Fourier-Stieltjes integral:

$$\boldsymbol{u}(\boldsymbol{x}) = \int \mathrm{e}^{\mathrm{i}\boldsymbol{k}\cdot\boldsymbol{x}} \mathrm{d}\boldsymbol{Z}(\boldsymbol{k}), \tag{1.2}$$

where the integration is over all wave-number space. The orthogonal process $\boldsymbol{Z}$ is connected to the spectral tensor by

$$\langle \mathrm{d}Z_i^*(\boldsymbol{k}) \mathrm{d}Z_j(\boldsymbol{k}) \rangle = \Phi_{ij}(\boldsymbol{k}) \mathrm{d}k_1 \mathrm{d}k_2 \mathrm{d}k_3, \tag{1.3}$$

which is valid for infinitely small $\mathrm{d}k_i$ and where * denotes complex conjugation.

1.2. *The 'sheared' spectral tensor*

Only an outline of the derivation of the sheared spectral tensor will be given since details may be found in Part IA.

To model the spectral velocity tensor in a shear flow we linearize the Navier-Stokes equation to estimate the effect of the shear on the turbulence. If we assume the shear to be linear such that $\partial U/\partial z$ is constant we obtain a simple linear differential equation for the time evolution or the 'stretching' of the spectral tensor. If the statistics of the initial condition is the isotropic von Kármán tensor (IA.2.16) with energy spectrum (IA.2.17), then the tensor $\Phi_{ij}(\boldsymbol{k}, t)$ will become more and more 'anisotropic' with time. The linearization is unrealistic, however, and at some point the stretched 'eddies' will break up. To close the problem an equilibrium is postulated where eddies of size $\propto |\boldsymbol{k}|^{-1}$ are stretched by the shear over a time proportional to their life time, τ. At least for relatively high frequencies (the inertial subrange), $\tau \propto k^{-2/3}$, and we introduce a parameter Γ, such that the non-dimensional life time, β, can be written as $\beta \equiv \frac{\mathrm{d}U}{\mathrm{d}z}\tau = \Gamma\frac{\mathrm{d}U}{\mathrm{d}z}(kL)^{-\frac{2}{3}}$. For a more realistic modeling of the eddy life time outside the inertial subrange see figure IA.3.

To the present purpose it is most convenient to present the results in terms of the stochastic process $\mathrm{d}\boldsymbol{Z}(\boldsymbol{k})$ as in Part IA. We write $\boldsymbol{k}_0$ for (k_1, k_2, k_{30}) with $k_{30} = k_3 + \beta k_1$. If $\mathrm{d}Z_i^{\mathrm{iso}}$ has the statistics of the isotropic von Kármán tensor, (IA.2.16), then the sheared tensor may be found from (1.3) and the following equations

$$\begin{pmatrix} \mathrm{d}Z_1(\boldsymbol{k}) \\ \mathrm{d}Z_2(\boldsymbol{k}) \\ \mathrm{d}Z_3(\boldsymbol{k}) \end{pmatrix} = \begin{bmatrix} 1 & 0 & C_1 - k_2C_2/k_1 \\ 0 & 1 & k_2C_1/k_1 + C_2 \\ 0 & 0 & k_0^2/k^2 \end{bmatrix} \begin{pmatrix} \mathrm{d}Z_1^{\mathrm{iso}}(\boldsymbol{k}_0) \\ \mathrm{d}Z_2^{\mathrm{iso}}(\boldsymbol{k}_0) \\ \mathrm{d}Z_3^{\mathrm{iso}}(\boldsymbol{k}_0) \end{pmatrix} \tag{1.4}$$

where

$$C_1 = \frac{\beta k_1^2(k_0^2 - 2k_{30}^2 + \beta k_1 k_{30})}{k^2(k_1^2 + k_2^2)} \tag{1.5}$$

and

$$C_2 = \frac{k_2 k_0^2}{(k_1^2 + k_2^2)^{\frac{3}{2}}} \arctan\left[\frac{\beta k_1 (k_1^2 + k_2^2)^{\frac{1}{2}}}{k_0^2 - k_{30}k_1\beta}\right], \tag{1.6}$$

which are identical to (IA.3.14) — (IA.3.17).

Compared to the isotropic tensor model we have an extra parameter Γ which determines the anisotropy of the tensor. Integrating the spectral tensor over the entire wavevector space gives the (co-)variances as a function of Γ (see fig. IA.4). It is seen that when anisotropy is introduced, $\sigma_u^2 > \sigma_v^2 > \sigma_w^2$ and $\langle uw \rangle < 0$ as confirmed by observations.

Three experimental tests of the model has been made. Two are atmospheric, one over water and one over flat terrain giving the parameters $L/z = 0.73$, $\Gamma = 3.2$ and $L/z = 0.87$, $\Gamma = 2.6$, respectively (see §IA.4). The third is based on data from a boundary layer wind tunnel giving $L/z = 0.60$, $\Gamma = 2.2$, implying that the turbulence is closer to being isotropic compared to the atmospheric turbulence, see §3.

1.3. *Fourier simulation*

Having discussed the spectral tensor we shall now describe how to simulate a velocity field $\boldsymbol{u}(\boldsymbol{x})$ from it.

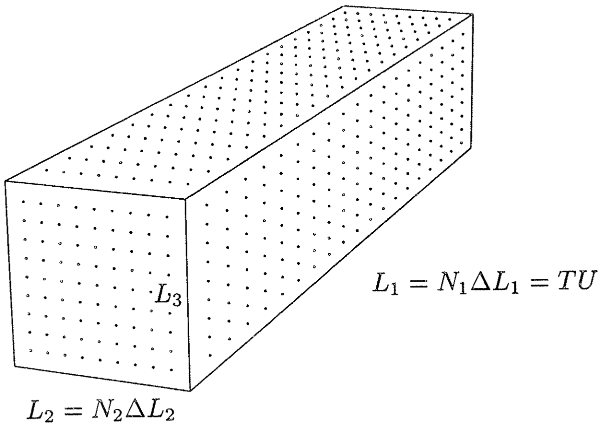

FIGURE 1. The box B consists of $N_1 \times N_2 \times N_3$ points and has side lengths L_i, $i = 1, 2, 3$, so the separation between the points in the i-direction is $\Delta L_i = L_i / N_i$. U is the mean wind speed and T is the simulation time.

We would like to approximate the integral (1.2) by a discrete Fourier series:

$$u_i(\boldsymbol{x}) = \sum_{\boldsymbol{k}} \mathrm{e}^{\mathrm{i}\boldsymbol{k}\cdot\boldsymbol{x}} C_{ij}(\boldsymbol{k}) n_j(\boldsymbol{k}), \tag{1.7}$$

where the i'th component of $\boldsymbol{x}$ is $x_i = n\Delta L_i$ with $n = 1, ..., N_i$. The symbol $\sum_{\boldsymbol{k}}$ denotes the sum over all wavevectors $\boldsymbol{k}$ with components $k_i = m2\pi/L_i$, with the integer $m = -N_i/2, ..., N_i/2$, $n_j(\boldsymbol{k})$ are independent Gaussian stochastic complex variables with unit variance and $C_{ij}(\boldsymbol{k})$ are coefficients to be determined. See figure 1. The great advantage of (1.7) is that, once the coefficients are known, it can be evaluated very fast by the fast Fourier transform (FFT). Solving (1.7) we get

$$C_{ij}(\boldsymbol{k}) n_j(\boldsymbol{k}) = \frac{1}{V(B)} \int_B u_i(\boldsymbol{x}) \mathrm{e}^{-\mathrm{i}\boldsymbol{k}\cdot\boldsymbol{x}} \mathrm{d}\boldsymbol{x}, \tag{1.8}$$

where $V(B) = L_1 L_2 L_3$ is the volume of B and $\int_B \mathrm{d}\boldsymbol{x}$ means integration over the box B. To find the coefficients $C_{ij}(\boldsymbol{k})$ we calculate the covariance tensor of (1.8) obtaining

$$\begin{aligned} & C_{ik}^*(\boldsymbol{k}) C_{jk}(\boldsymbol{k}) \\ & = \frac{1}{V^2(B)} \int_B \int_B \langle u_i(\boldsymbol{x}) u_j(\boldsymbol{x}') \rangle \, \mathrm{e}^{\mathrm{i}\boldsymbol{k}\cdot\boldsymbol{x}} \mathrm{e}^{-\mathrm{i}\boldsymbol{k}\cdot\boldsymbol{x}'} \mathrm{d}\boldsymbol{x} \mathrm{d}\boldsymbol{x}' \\ & = \frac{1}{V^2(B)} \int \int R_{ij}(\boldsymbol{x} - \boldsymbol{x}') 1_B(\boldsymbol{x}) 1_B(\boldsymbol{x}') \mathrm{e}^{\mathrm{i}\boldsymbol{k}\cdot(\boldsymbol{x}-\boldsymbol{x}')} \mathrm{d}\boldsymbol{x} \mathrm{d}\boldsymbol{x}', \end{aligned} \tag{1.9}$$

where 1_B denotes the indicator function of B. Using the convolution theorem we get

$$C_{ik}^*(\boldsymbol{k}) C_{jk}(\boldsymbol{k}) = \int \Phi_{ij}(\boldsymbol{k}') \prod_{l=1}^{3} \mathrm{sinc}^2 \left(\frac{(k_l - k_l') L_l}{2} \right) \mathrm{d}\boldsymbol{k}', \tag{1.10}$$

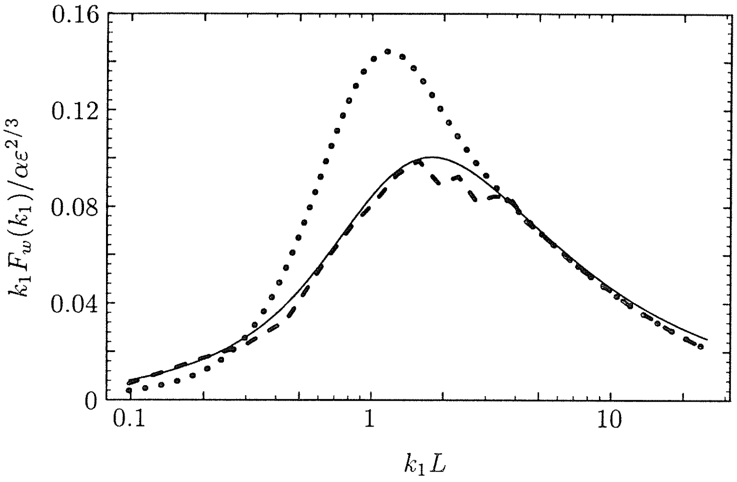

FIGURE 2. Illustration of the discretization problem by an isotropic w-spectrum. The thin line is the target spectrum, the dotted line is the average spectrum obtained by using (1.12) and the dashed line is an average spectrum using (1.13).

---

where $\operatorname{sinc} x \equiv (\sin x)/x$. For $L_l \gg L$, assuming $\mathrm{d}k_l = 2\pi/L_l$, we have

$$C^*_{ik}(\boldsymbol{k})C_{jk}(\boldsymbol{k}) = \frac{(2\pi)^3}{V(B)}\Phi_{ij}(\boldsymbol{k}) = \langle \mathrm{d}Z^*_i(\boldsymbol{k})\mathrm{d}Z_j(\boldsymbol{k})\rangle\,. \tag{1.11}$$

The relation $C_{ij}(\boldsymbol{k})n_j(\boldsymbol{k}) = \mathrm{d}Z_i(\boldsymbol{k})$ then implies

$$C_{ij}(\boldsymbol{k}) = \frac{(2\pi)^{3/2}}{V(B)^{1/2}}A_{ij}(\boldsymbol{k}) \tag{1.12}$$

with $A^*_{ik}A_{jk} = \Phi_{ij}$, which is expected comparing (1.2) to (1.7).

1.3.1. *Problems with discretization and periodicity*

Two problems occur by simulating a field by the Fourier series (1.7) with the coefficients (1.12). The first is that for many applications the dimensions of the simulated box need not to be much larger than the length scale of the turbulence model L. Therefore (1.11) may not be a good approximation to (1.10). However, almost always $L_1 \gg L$, so we can at least reduce (1.10) to

$$\begin{aligned} &C^*_{ik}(\boldsymbol{k})C_{jk}(\boldsymbol{k}) \\ &= \frac{2\pi}{L_1}\int \Phi_{ij}(k_1,k'_2,k'_3)\prod_{l=2}^{3}\operatorname{sinc}^2\left(\frac{(k_l-k'_l)L_l}{2}\right)\mathrm{d}\boldsymbol{k}'_\perp \end{aligned} \tag{1.13}$$

This integration, which has to be done numerically is here limited to wavevectors, $\boldsymbol{k}$, obeying $k = |\boldsymbol{k}| < 2.5/L$. Outside this volume we consider (1.11) to be a good approximation to (1.10) regardless of the dimensions of the box. This discretization problem is illustrated by figure 2. The thin line is the target spectrum, the dotted line is the average spectrum obtained by using (1.12) with dimensions $64L \times 2L \times 2L$, that is $L_l \gg L$ is not true for $l = 2, 3$. The dashed line is an average of ten $512 \times 32 \times 32$ points simulations using (1.13) as described above.

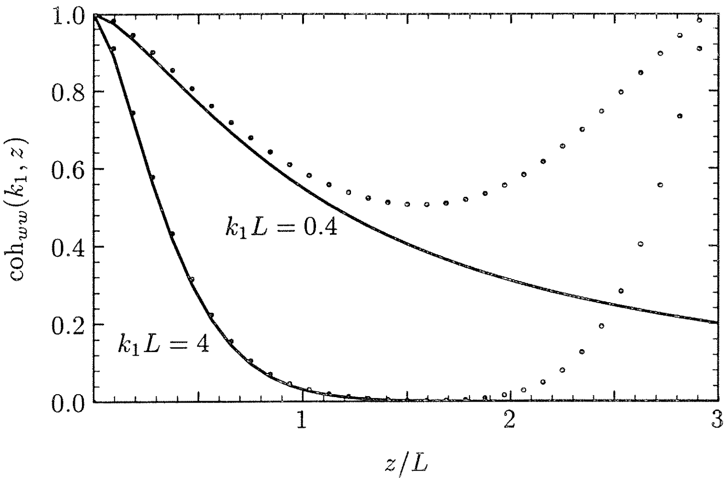

FIGURE 3. Illustration of periodicity. Simulated (dots) and model w-coherences (curves) as functions of vertical coordinate z. The vertical dimension of the box is $L_3 = 3L$.

The second problem is that the simulated velocity field (1.7) is periodic in all three directions. Shinozuka and Jan (1972) suggested to perturb the wavevectors in (1.7) to avoid this problem. However, this would corrupt the efficiency of the FFT. Our solution to the problem is to use a larger spatial window. In figure 3 the coherence of vertical velocity fluctuations for a vertical separation

$$\mathrm{coh}_{ww}(k_1, z) \equiv \frac{|\chi_{33}(k_1, z)|^2}{\chi_{33}(k_1, 0)^2} \tag{1.14}$$

calculated from the sheared velocity tensor with $\Gamma = 4$ according to (IA.2.7) is shown together with coherences calculated from simulations with $2048 \times 32 \times 32$ points and dimensions $256L \times 3L \times 3L$. Since the simulated field is periodic the coherence goes to 1 as $z \to L_3 = 3L$. In a response analysis the space domain (L_2 and L_3) should be chosen large enough to contain roughly *twice* the structure of interest in each dimension. However, if $L_l \gg L$ or if the structure is insensitive to low frequency fluctuations the structure might cover more than half the simulated field in each direction.

An example of a simulated non-isotropic velocity field with $\Gamma = 4$ is shown in Figure 4. It is seen that the shear elongates and tilts the fluctuations.

1.3.2. *Implementation and speed*

The implementation of the model includes three steps:

(i) Evaluate the coefficients $C_{ij}(\boldsymbol{k})$, either by (1.12) or if necessary by (1.13).
(ii) Simulate the Gaussian variable $n_j(\boldsymbol{k})$ and multiply.
(iii) Calculate $u_i(\boldsymbol{x})$ from (1.7) by FFT.

The time consumption in the first step is proportional to the total number of points $N = N_1N_2N_3$ in the simulation. It is well known that the required time to perform the FFT is $O(N \log_2 N)$.

If only one velocity component, i, is needed then $A(\boldsymbol{k})$ is simply $\sqrt{\Phi_{ii}(\boldsymbol{k})}$. In this case the first two steps in the $2048 \times 32 \times 32$ simulation used in figure 3 took $3\frac{1}{4}$ minutes

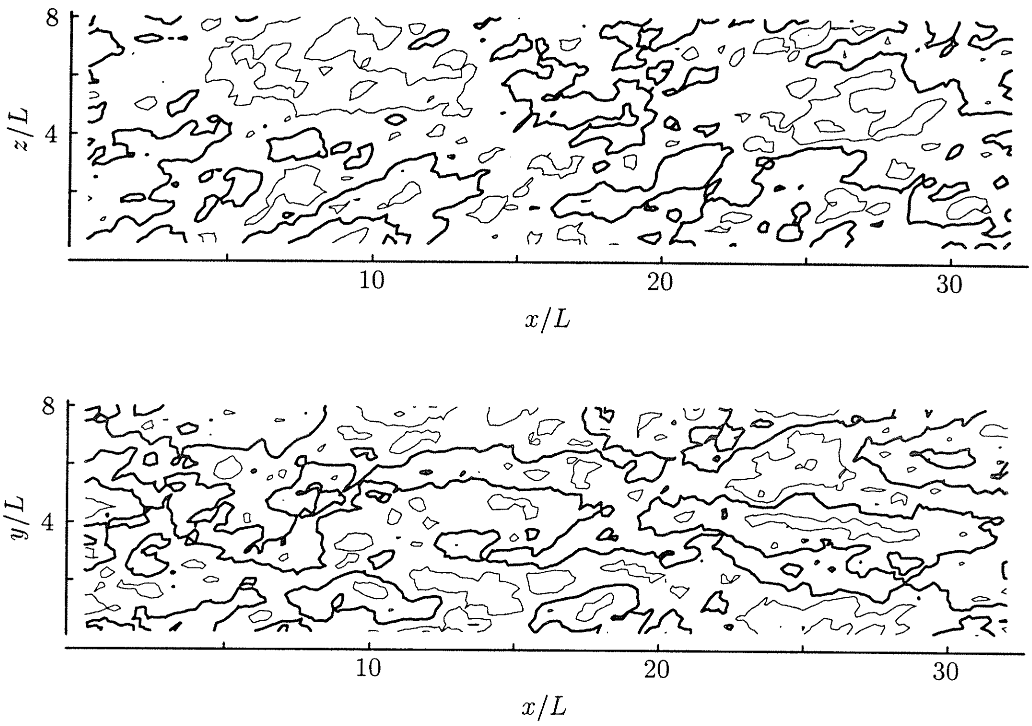

FIGURE 4. Vertical and horizontal cross sections of the u-fluctuations of simulated non-isotropic turbulence with $\Gamma = 4$. The broad contours have $u_1 = 0$ and the thin contours have $u_1 = \pm\sigma_u$ or $\pm 2\sigma_u$.

---

on a Intel 486 25 MHz computer. The FFT used used $2\frac{1}{4}$ minutes and input/output 45 seconds giving a total execution time of $6\frac{1}{4}$ minutes. If the integral (1.13) is not used only half a minute is saved on the execution time while the spectra are poorly simulated as illustrated by figure 2.

To simulate all three velocity components $\mathrm{d}Z_i^{\mathrm{iso}}$ is first calculated from (1.12) with the explicit factorization

$$A(\boldsymbol{k}) = \frac{E^{1/2}(k)}{(4\pi)^{1/2}k^2}\begin{pmatrix} 0 & k_3 & -k_2 \\ -k_3 & 0 & k_1 \\ k_2 & -k_1 & 0 \end{pmatrix} \tag{1.15}$$

of Φ^{iso} (see equation (IA.2.16)). Then $\mathrm{d}Z_i^{\mathrm{iso}}(\boldsymbol{k}_0)$ is transformed into $\mathrm{d}Z_i(\boldsymbol{k})$ by (1.4) and (1.7) is used to get $\boldsymbol{u}(\boldsymbol{x})$.

1.4. *Conclusion and future developments*

In this section we simulate a stochastic field from a spectral tensor. This has not been done before for a realistic spectral velocity tensor for atmospheric surface layer turbulence, apparently because no such tensor model has been available. This paper is in principle a special case of the general paper by Shinozuka and Jan (1972). There are some differences, however: Shinozuka and Jan use (1.12) which in our specific study is shown *not* to be a good approximation to the exact (1.10). Furthermore, we use evenly

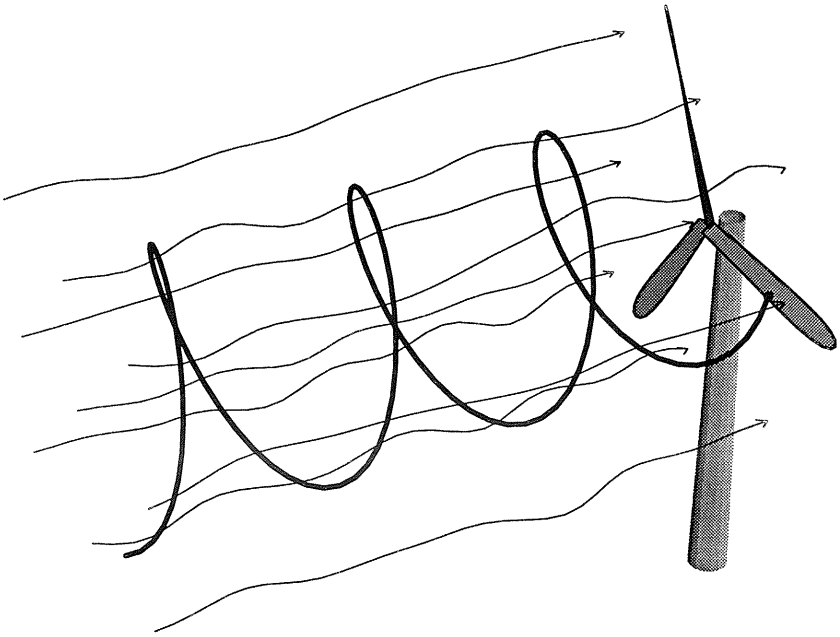

FIGURE 5. Sketch of experimental setup in Kretz *et al.* (1994). The wind velocity measuring instrument is mounted on a blade, so the path of the instrument is a helix.

spaced wavevectors while Shinozuka and Jan suggest to wobble the wavevectors in order to avoid the imposed periodic boundary conditions.

The two most time consuming steps in our algorithm are the evaluation of the spectral tensor using time proportional to the number of points in the simulations $N = N_1N_2N_3$, and the FFT using $O(N \log_2 N)$.

Methods bases on cross-spectra often has the decomposition of N_1 cross-spectral matrices as the most time consuming step. The fastest algorithm to do this known to the author is proportional to $N_1N_2^2N_3^2$, Winkelaar (1991), i.e., considerably slower than our simulation method. Winkelaar's study uses coherences and not complex cross-spectra in which case important phase information is lost. Simulations based on Winkelaar (1991) would thus never show tilted velocity fluctuations as in the upper contour plot of figure 4.

The work presented in this section is far from finished. Firstly, I have to clarify the problems in §1.3.1 and provide general ways to avoid them. Secondly, the method has to prove its usefulness in engineering. An important first step in that direction has been taken by Kretz, Madsen and Petersen (1994) from the Test Station for Wind Turbines at Risø. They have mounted five–hole pitot tube on a blade of a wind turbine (see figure 5) in order to measure actual wind fluctuations impinging on the blade which give rise to the forces and torque attacking the blade. Kretz *et al.* then used two models to simulate the wind wind field streaming through the rotor plane; the one presented here and the frequently used Sandia method (Veers 1988) (which is refined in Winkelaar (1991)). Their tentative conclusion is that the model presented here compares very favorably to

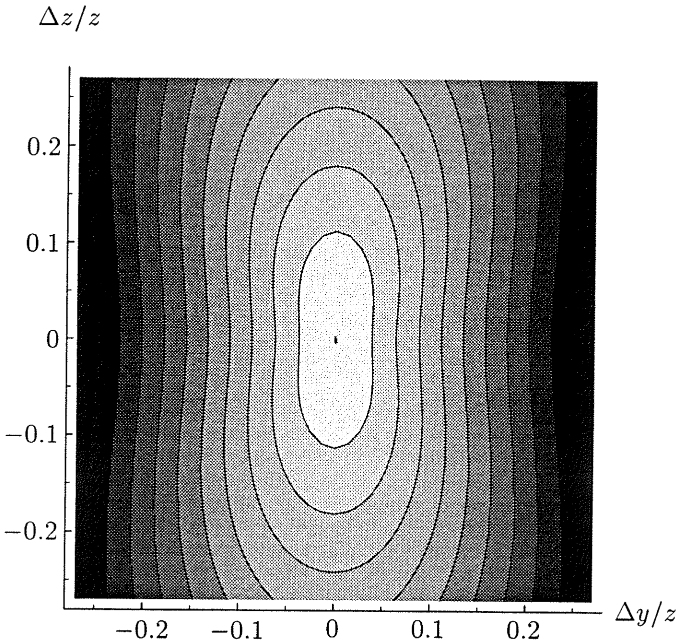

FIGURE 6. Contour plot of $R_{13}(0, \Delta y, \Delta z)/R_{13}(0,0,0)$ for $L/z = 0.9$ and $\Gamma = 3$. Contours at 1.0, 0.975, 0.95, ... The 1.0 contour is the dot at (0,0).

---

the Sandia method by giving more realistic spectra of the forces on the blades. Kretz *et al.* (1994) show that this has significant consequences for the estimation of the blade fatigue. An other engineering application to pursue is the calculation of dynamic loads on large bridges.

2. Momentum flux measurements with displaced sensors

The vertical flux of horizontal momentum is measured by correlating vertical and horizontal velocity fluctuation in one point. A simple application of the US model is to estimate the loss or gain of measured momentum flux caused by spatial averaging or by the sensors of vertical and horizontal velocity not being co-located. Firstly, we shall calculate the correlation expected from ideal pointlike vertical and horizontal velocity sensor placed in two displaced point, i.e. we shall look at $R_{13}(\boldsymbol{r})$ for non-zero $\boldsymbol{r}$. Secondly, in §2.2, we shall investigate the expected response from a specific sonic array.

The spectral tensor model presented in the main text is well suited for these calculation because the observed $k_1^{-\frac{7}{3}}$ behavior of the *uw* cross-spectrum (Wyngaard & Coté 1972) is obeyed by the model.

We believe that the US+B model (§3.3) is unnecessary complicated for the subsequent calculations because only the larger scales of the turbulence are affected by the blocking by the surface. Therefore, we use the simpler US model (§3.2). The calculations apply to horizontally homogeneous sites.

2.1. *The structure of* R_{13}

The correlation $R_{13}(\boldsymbol{r})$ is calculated from the US model (§3.2) of the spectral tensor

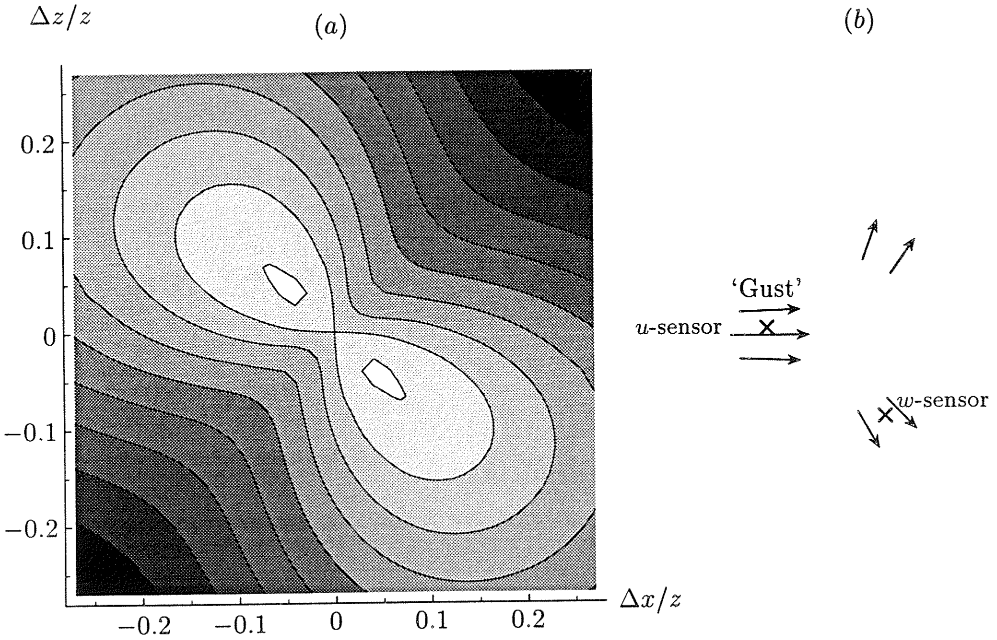

FIGURE 7. (*a*): Contour plot of $R_{13}(\Delta x, 0, \Delta z)/R_{13}(0,0,0)$ for $L/z = 0.9$ and $\Gamma = 3$. Contours at 1.025, 1.0, 0.975, 0.95, ... The 1.0 contour is "8"-shaped. (*b*): Sketch to support the qualitative argument for the location of extrema of the correlation. The u- and w-sensors are located at crosses and the u-sensor is engulfed in a localized gust.

---

by the inverse of (2.3):

$$R_{13}(\boldsymbol{r}) = \int \Phi_{13}(\boldsymbol{k}) \exp(\mathrm{i}\boldsymbol{k} \cdot \boldsymbol{r}) \mathrm{d}\boldsymbol{k}. \tag{2.1}$$

Figure 6 shows the correlation in the yz-plane and figure 7 in the xz-plane for parameters $L/z = 0.9$ and $\Gamma = 3$, which agree with the observed values from The Great Belt Experiment and LAMEX. We have assumed the length parameter L to scale with z, which is expected from neutral surface similarity theory.

The enhanced correlation away from (0,0) in figure 7*a* can be explained from the incompressibility of the flow: Suppose u is measured at (0,0) and w at a small positive Δx and a small negative Δz as in figure 7*b*. If a local 'gust' engulfes the u-sensor at some instant (i.e. positive u), then, because of incompressibility, it is probable that there is a positive divergence in the yz-plane for small positive x as illustrated on the drawing (fig. 7*b*). Therefore, it is likely that w is negative at the position of the sensor. The correlation of u and w at these points is thus expected to be negative *only* because of incompressibility. The negative correlation will add to the general negative correlation (because of the downward momentum flux) and $R_{13}(\Delta x, 0, \Delta z)/R_{13}(0,0,0)$ becomes larger that one. Similar arguments account for the behavior of the correlation in the other three quadrants of figure 7.

2.2. *The 'K' style sonic array*

The 'K' style sonic array, named after its designer J. C. Kaimal (Kaimal *et al.* 1990),

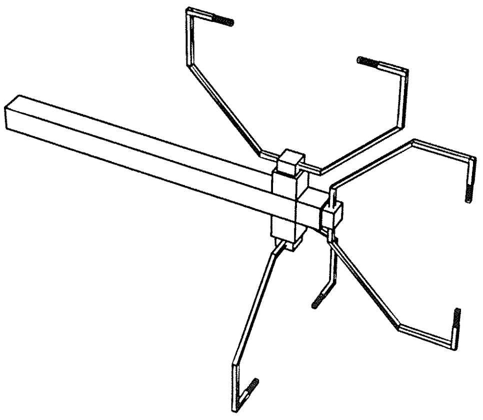

FIGURE 8. Sketch of the 'K' style sonic array from Advanced Technologies, Inc.

is used for atmospheric boundary layer studies. The K sonic consists of three transducer pairs with gaps of $G = 0.15$ m. It is designed to minimize flow distortion errors at the expense of the co-location of the gaps; see figure 8. We use the US spectral tensor model to estimate the consequences of the displaced sensor gaps.

To make the analysis more complete we also take into account the finite gaps. First we calculate the covariance between to arbitrarily positioned and oriented acoustic paths (straight line between a transducer pair). Their signals are

$$X = \frac{1}{G}\int_{-G/2}^{G/2} \boldsymbol{m}\cdot\boldsymbol{u}(l\boldsymbol{m}+\boldsymbol{r})\mathrm{d}l \tag{2.2}$$

and

$$Y = \frac{1}{G}\int_{-G/2}^{G/2} \boldsymbol{n}\cdot\boldsymbol{u}(l'\boldsymbol{n}+\boldsymbol{s})\mathrm{d}l', \tag{2.3}$$

where $\boldsymbol{r}$ and $\boldsymbol{m}$ are the position and orientation (a unit vector parallel to the gap line) of sonic X, $\boldsymbol{s}$ and $\boldsymbol{n}$ are the position and orientation of sonic Y and G is the length of the gap. The covariance of X and Y is

$$\begin{aligned}\langle XY\rangle &= \frac{m_i n_j}{G^2}\int_{-G/2}^{G/2}\int_{-G/2}^{G/2} R_{ij}(l'\boldsymbol{n}-l\boldsymbol{m}+\boldsymbol{s}-\boldsymbol{r})\mathrm{d}l\mathrm{d}l' \\ &= \frac{m_i n_j}{G^2}\int \Phi_{ij}(\boldsymbol{k})\exp(\mathrm{i}\boldsymbol{k}\cdot(\boldsymbol{s}-\boldsymbol{r}))\int_{-G/2}^{G/2}\int_{-G/2}^{G/2}\exp(\mathrm{i}\boldsymbol{k}\cdot(l'\boldsymbol{n}-l\boldsymbol{m}))\mathrm{d}l\mathrm{d}l'\mathrm{d}\boldsymbol{k} \\ &= m_i n_j\int \Phi_{ij}(\boldsymbol{k})\cos(\boldsymbol{k}\cdot(\boldsymbol{s}-\boldsymbol{r}))\,\mathrm{sinc}\,(\boldsymbol{k}\cdot\boldsymbol{m}G/2)\,\mathrm{sinc}\,(\boldsymbol{k}\cdot\boldsymbol{n}G/2)\,\mathrm{d}\boldsymbol{k}, \end{aligned} \tag{2.4}$$

where $\mathrm{sinc}(x) \equiv \sin(x)/x$.

The velocity components measured by the three sonics in the K sonic array are $H_1 + h_1$ (upper), $H_2 + h_2$ (lower) and w_{av} (vertical), where $\langle h_1\rangle = \langle h_2\rangle = \langle w_{av}\rangle = 0$. The non-zero component of the mean wind vector is $U = \sqrt{H_1^2 + H_2^2}$. The measured longitudinal

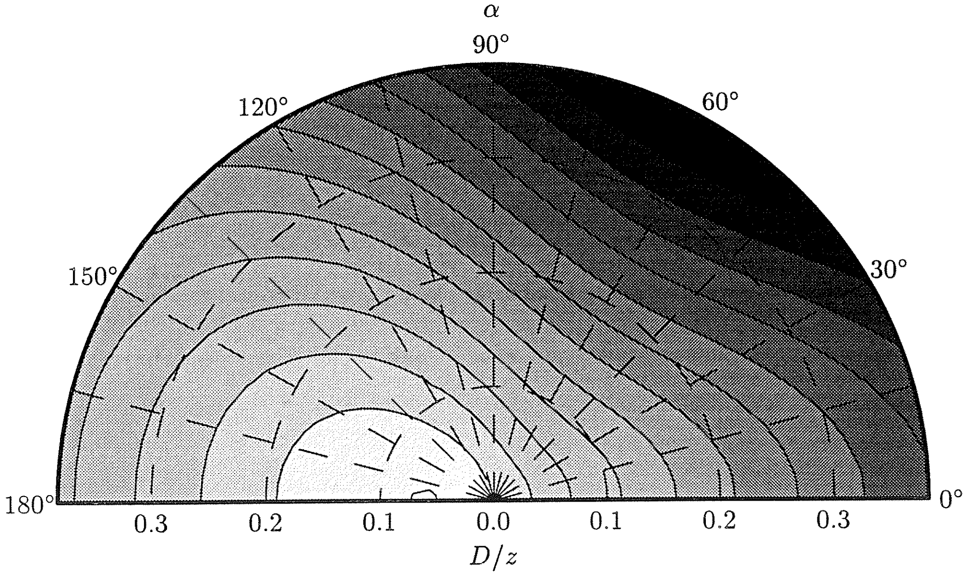

FIGURE 9. Contour plot of $\langle uw \rangle_m / R_{13}(0,0,0)$, the normalized momentum flux as expected to be measured by the K sonic. The radial axis is the 'size' of the sonic $D = 0.185$ m divided by the height above the ground z, and α is the direction of the mean wind field with $\alpha = 0$ being parallel to the boom head on the vertical sonic, see figure 8. The 100% contour passes exactly through zero, because here neither the distance between the acoustic paths nor the finite gap will influence the measurement. Contours are spaced by 2.5%.

---

velocity fluctuations become $u = h_1 \cos\alpha - h_2 \sin\alpha$, where $\cos\alpha = H_1/U$, and $v = h_1 \sin\alpha + h_2 \cos\alpha$ for the transversal.

If D denotes the horizontal distance from the vertical sonic to the others, which is equal to half the distance from the upper to the lower sonic, then the measured momentum flux is

$$\langle uw \rangle_m = \langle h_1 w_{av} \rangle \cos\alpha - \langle h_2 w_{av} \rangle \sin\alpha \tag{2.5}$$

with displacement vector $\boldsymbol{s} - \boldsymbol{r} = (D\cos\alpha, D\sin\alpha, D)$ for the first term on the right hand side and $(D\cos\alpha, D\sin\alpha, -D)$ for the second in the coordinate system defined by the mean wind velocity. Each term in (2.5) is calculated by (2.4) for the geometry of the K sonic ($D = 0.185$ m) and the result is shown in figure 9.

As seen from figure 9 the measured flux for any incident angle will be larger than 92% of the real flux, if $D/z = 0.1$, i.e. $z = 1.85$ m. So it seems that the instrument has to be very close to the ground (< 2 m) to get any significant flux reduction ($> 10\%$). This agrees well with Kaimal's (1990) recommendation not to use the instrument below 4 m. If the instrument were turned up side down the error for small α would be even less. This is because in that case the displacement vector between the u- and w-sensor will be positive Δx and negative Δz so the momentum flux will be reduced comparably little, see figure 7.

From (2.4) it can be seen that the averaging by the gaps is not important. The 'Half Width at Half Maximum' of the cosine term in (2.4) is $k_{\mathrm{HWHM}} = \arccos(\frac{1}{2})/|\boldsymbol{r} - \boldsymbol{s}| \approx 4.00\mathrm{m}^{-1}$ for the geometry of the K sonic. The HWHM of the sinc term is $k_{\mathrm{HWHM}} =$

$3.79/G \approx 25.3\text{m}^{-1}$. So it is almost only the cosine term that attenuates the flux, i.e. only the displacement of the sensors matters. Careful numerical experimentation shows that the line averaging in the acoustic gaps has a detectable but *very* small effect on the momentum flux measured by the K sonic.

For the validation of the theoretical predictions in this appendix a small experiment at Risø has been planed. Unfortunately, the experiment has been delayed and could thus not be included in this dissertation.

3. The spatial structure of boundary layer wind tunnel turbulence

The purpose of this section is to compare the turbulence in the new, wide boundary layer tunnel at the Danish Maritime Institute (DMI) in Lyngby to the turbulence measured at Sprogø in the Great Belt. It is of particular interest to estimate the differences in the turbulent energy available for buffeting excitation (Davenport *et al.* 1992, and references therein) at different frequencies attributed to the imperfectly simulated turbulence in the wind tunnel. The tool used to do this is the spectral tensor model of Part IA.

The wind tunnel has in addition to carpets on the tunnel floor 21 spires to create the turbulent wind. The difference between the natural turbulent wind and the wind tunnel turbulence is primarily that latter is slightly more isotropic. This implies that the length scales of the u-spectrum and w-spectrum are not far apart, while in the natural boundary layer the scales are separated by a factor of ~ 10. The reason for this is primarily the limited length of the wind tunnel. In absence of spires at the tunnel inflow a turbulent equilibrium boundary layer is not able to develop to the height of the bridge deck.

Since the turbulent fluctuation of the vertical velocity component is the most important for the buffeting excitation of the bridge deck the w-scale has been chosen to fit the target spectrum (as described in the design basis of the Eastern Bridge of the Great Belt connection) so we shall emphasize vertical fluctuations in the this investigation.

We compare the wind tunnel data with the US model in §IA.3.2. We have chosen not to use the US+B model because it is more complicated and does not give very different results.

In §3.2 the US model will be used to estimate the differences in turbulent energy available for buffeting excitation response due to imperfectly simulated turbulence as a function of wavenumber or frequency. In order to do so the following highly idealized assumptions are made:

(i) The length scales of the relevant eigen-modes of the bridge are large compared to the transversal distance over which fluctuations are correlated or equivalently, where the coherence is not small.

(ii) There is a linear relation between the two-point cross-spectrum of w (or u) and response spectrum of a given eigenmode.

Clearly, this last assumption can only be valid for buffeting excitation, and even in that case the assumption is probably too crude. The 'idealized response amplitudes' derived in §3.2 should thus only give an indication of how the Boundary Layer Wind Tunnel (BLWT) over- or underestimates the buffeting response amplitudes.

The tentative conclusion is that at the highest relevant frequencies the the buffeting response amplitude due to vertical velocity fluctuations will be overestimated by the

BLWT by up to 20%. However, as discussed in §3.3, the extrapolation of the Great Belt data to very high wind speeds adds uncertainty to this conclusion.

The data were kindly provided by Timothy A. Reinhold and Michael Brinch of the Danish Maritime Institute.

3.1. *Data analysis*

In the wind tunnel experiment the vertical and horizontal velocity was measured simultaneously in two points. The measurements were carried out without the model bridge in the tunnel. The probes were displaced by a distance ranging from 0.01 m to 0.22 m normal to the flow in a height of 0.35 m. This corresponds to a full scale height of 70 m and horizontal separations of 2 to 44 m since the bridge model (which was not in the wind tunnel during this test) was build on the scale of 1 to 200. The velocity measuring devices were of the type DANTEX 55F63 and consisted of two slanting hot wires in an X configuration. Since lateral homogeneity of the most simple statistics such as mean velocity and velocity variance already has been shown by Smitt and Brinch (1992) we only perform this more detailed analysis for the velocity probes placed at the center line of the tunnel at the downstream position of where the bridge model were situated during aerodynamic tests.

The w- and u-components have been derived without taking into account the sensitivity to the transversal velocity fluctuations and deviations from a pure cosine response (Larsen 1986, Appendix E.). Using Larsen's (1986) values for the pitch and yaw correction valid for the DISA 55F11 sensor which is similar to the present sensors we multiply the u-spectrum by 0.97, w- by 1.11 and the uw-cross-spectrum by ~ 1.06. This is done to all wind tunnel spectra in this report†.

Three one-point spectra can be determinated from the data, namely $F_u(k_1)$, $F_w(k_1)$ and the cross-spectrum $\chi_{uw}(k_1)$, where $k_1 = 2\pi f/U$ is the wave number in the direction of the mean wind, f the frequency and U the mean wind speed. Furthermore, we calculate two two-point cross-spectra for each horizontal separation Δy of the cross-wires: $\chi_{ww}(k_1, \Delta y, 0)$ and $\chi_{uu}(k_1, \Delta y, 0)$, where the zero indicates no vertical separation of the probes.

The purpose of data analysis or data reduction is to describe large amounts of data by a simple theory or model. Here we shall use the spectral tensor model (US) developed in Part IA.

The three one-point spectra are fitted to the data in figure 10. This procedure yields the three parameters of the tensor which in turn enables us to predict all cross-spectra or *coherences* defined as

$$\mathrm{coh}_{ii}(k_1, \Delta y, \Delta z) = \frac{|\chi_{ii}(k_1, \Delta y, \Delta z)|^2}{F_i^2(k_1)}, \tag{3.1}$$

where $F_i(k_1) = \chi_{ii}(k_1, 0, 0)$ (no summation) is the one-point spectrum. Experimenting with the lifetime models in §IA.3.1 we find that (IA.3.6) is not the best fit to the wind tunnel data, as was the case for the atmospheric experiments, but that (IA.3.1) fits better. The minimized χ^2 (see eq. IA.4.1) for the model (IA.3.6) is 50% larger than for

---

† The ratio between the u-spectrum and the w-spectrum is ~ 0.87, i.e., not 3/4 as it should be in the inertial subrange (high frequencies). Without Larsen's correctinos the ratio would be even larger.

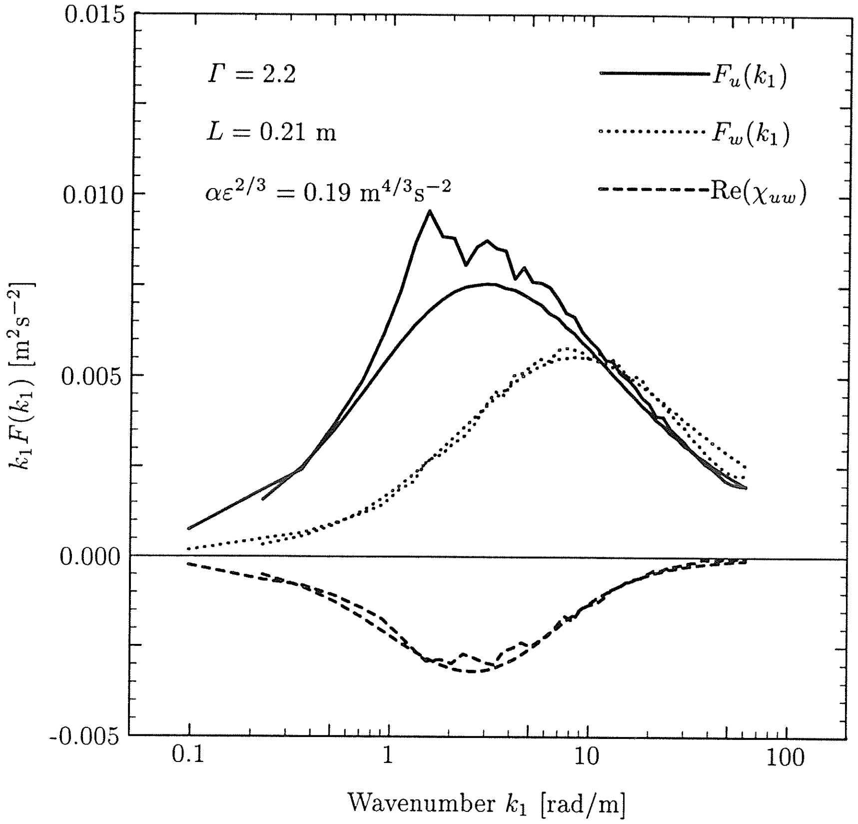

FIGURE 10. The spectral tensor model fitted to the three measured one-point spectra giving the three parameters Γ, L and $\alpha\varepsilon^{2/3}$. The smooth curves are the fit and the ragged curves the data.

(IA.3.1) for the wind tunnel spectra. Consequently, we use (IA.3.1) in the US model to predict the coherences in the wind tunnel.

The model fits the one-point spectra well as seen from figure 10, and the predicted coherences are shown in figures 14 to 16. Around the theoretical predictions in these figures the expected 1-σ scatter is shown as dashed lines according to (IA.4.6) with 82 degrees of freedom. It is seen that the predictions are fairly accurate. However, a curious deviation from the predictions is seen in figure 14 for $\Delta y = 0.01$ m both for the u- and the w-component. A possible explanation for this is that Δy could have been close to 0.013 m instead of 0.01 m.

To compare atmospheric and wind tunnel the data have to be scaled in such a way that the Froude number $F = U^2/(lg)$ is invariant. Since the acceleration due to gravity g can not be changed and all dimensions of the model l is scaled down from the full scale bridge by a factor of 200, the mean velocity in the wind tunnel U must be scaled up by a factor $\sqrt{200}$. The wind tunnel wind speed is 4.1 m/s corresponding to a atmospheric wind speed of $\sim$ 58 m/s. Spectra and cross-spectra were only obtained at wind speeds up to 23 m/s at Sprogø so these spectra must also be scaled. Larsen *et al.* (1991) found experimentally $\sigma_w^2 \propto U^2$ for $U < 30$ m/s. We assume that this proportionality holds

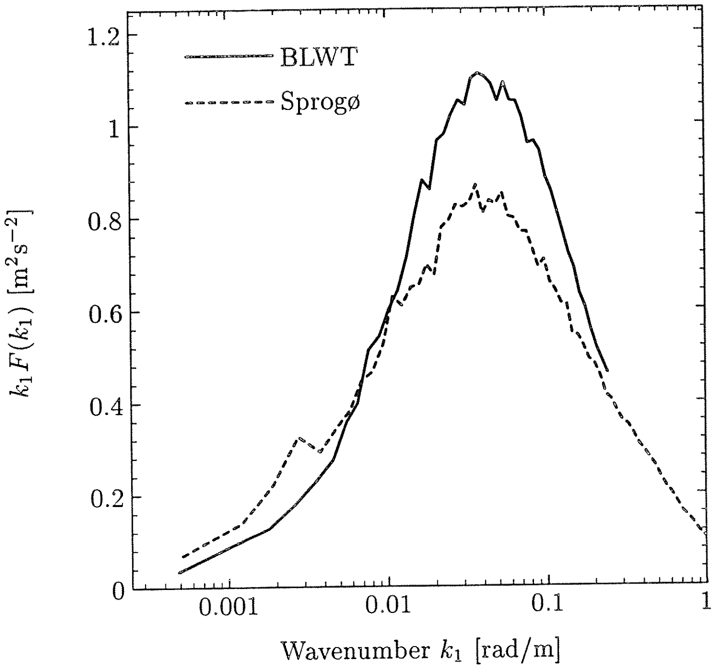

FIGURE 11. Comparison of w-spectra from the boundary layer wind tunnel and from Sprogø at a full scale velocity of 58 m/s.

up to 56 m/s. The scaled w-spectra are shown in figure 11. Comparing the spectra the turbulence seems to be somewhat too strong in the wind tunnel at most frequencies.

3.2. *Consequences for the 'idealized response amplitudes'*

Having compared turbulence measurements from the Great Belt to the BLWT we shall in this section discuss the consequences for the buffeting response amplitudes. The discussion is highly idealized, so the results are only an indication of what the imperfectly simulated turbulence in the BLWT might imply for the prediction of the oscillation amplitudes of the bridge deck.

Assuming linear excitation of the eigenmodes of the bridge and that the width of the bridge deck is smaller than the scales in the turbulence that excites the motions, the square of the amplitude can be written as a weighted integral of the cross-spectrum of the component(s) of the wind that excites the mode. The weighting includes the mode shape, damping coefficient, eigenfrequency and more. It is obvious from experimental studies that these assumptions are too crude. See e.g. Davenport *et al.* (1992, figure 16), where forces and wind fluctuations are seen to have different correlations along the bridge deck. However, we assume that we are able to give an indication of the relative difference in the amplitudes due to differences between the simulated boundary layer turbulence and the atmospheric turbulence over the Great Belt.

Since the wavelengths of the relevant eigen-modes are long compared to the separation over which the turbulent velocity fluctuations become uncorrelated, the squared amplitude A^2 of a given mode can under these idealized circumstances be shown to be

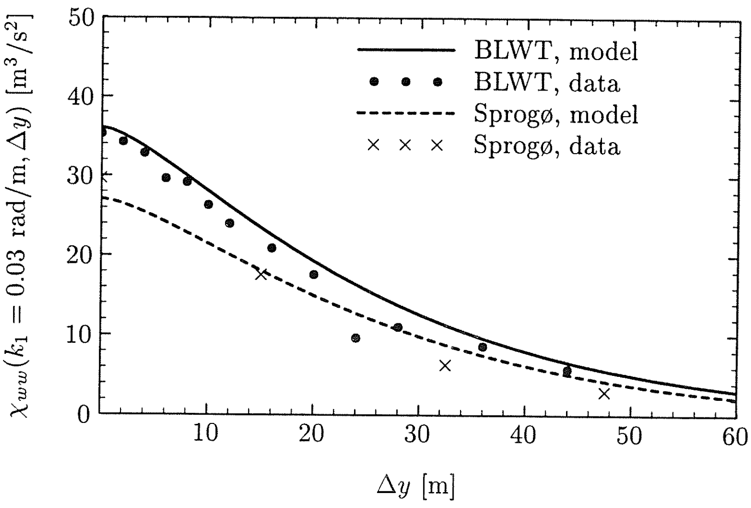

FIGURE 12. Cross-spectra of vertical velocity fluctuations as a function of horizontal displacement Δy for a fixed wavenumber $k_1 = 0.03$ rad/m. Both model predictions and actual data are shown. Wind tunnel data are scaled up to full size and Sprogø data are scaled up to $U = 58$ m/s.

---

proportional to the integral of the cross-spectrum. We get

$$\begin{aligned} A^2 &\propto \int_{-\infty}^{\infty} \chi_{ij}(k_1, y, 0)\mathrm{d}y \\ &= \int\int_{-\infty}^{\infty} \Phi_{ij}(\boldsymbol{k}) \exp(\mathrm{i}k_2 y)\mathrm{d}y\mathrm{d}\boldsymbol{k}_\perp \\ &= \int \Phi_{ij}(\boldsymbol{k}) 2\pi\delta(k_2)\mathrm{d}\boldsymbol{k}_\perp \\ &= 2\pi \int_{-\infty}^{\infty} \Phi_{ij}(k_1, 0, k_3)\mathrm{d}k_3 \end{aligned} \tag{3.2}$$

where we have used (IA.2.7) to relate the cross-spectrum to the spectral tensor and the identity $\int_{-\infty}^{\infty} \exp(\mathrm{i}k_2 y)\mathrm{d}y = 2\pi\delta(k_2)$, where δ is Dirac's delta function. Equation (3.2) gives an approximate relation between the amplitude and the tensor for a wavenumber $k_1 = 2\pi f_0/U$, where f_0 is the eigenfrequency and U is the mean wind speed.

Cross-spectra of vertical velocities are shown on figure 12 as a function of displacement Δy. It is seen that the US model predicts both cross-spectra well.

The tensor obtained from the boundary layer wind tunnel is scaled up from model size and is called $\Phi_{ij}^{\mathrm{BLWT}}$ and the tensor extracted from the Great Belt Coherence Experiment is denoted by $\Phi_{ij}^{\mathrm{GBelt}}$. By (3.2) the ratio between the 'idealized response amplitudes' of the model in the wind tunnel scaled up to natural size and the amplitudes of the Great Belt bridge is

$$\frac{A_{\mathrm{BLWT}}}{A_{\mathrm{GBelt}}} = \left(\frac{\int_{-\infty}^{\infty} \Phi_{ij}^{\mathrm{BLWT}}(k_1, 0, k_3)\mathrm{d}k_3}{\int_{-\infty}^{\infty} \Phi_{ij}^{\mathrm{GBelt}}(k_1, 0, k_3)\mathrm{d}k_3} \right)^{1/2} \tag{3.3}$$

under the assumptions given in the start of this section.

If $i = j = 3$ then (3.3) gives the ratio of amplitudes for modes primarily excited by the w-component of the velocity fluctuations and if $i = j = 1$ it gives the ratio of u-excited

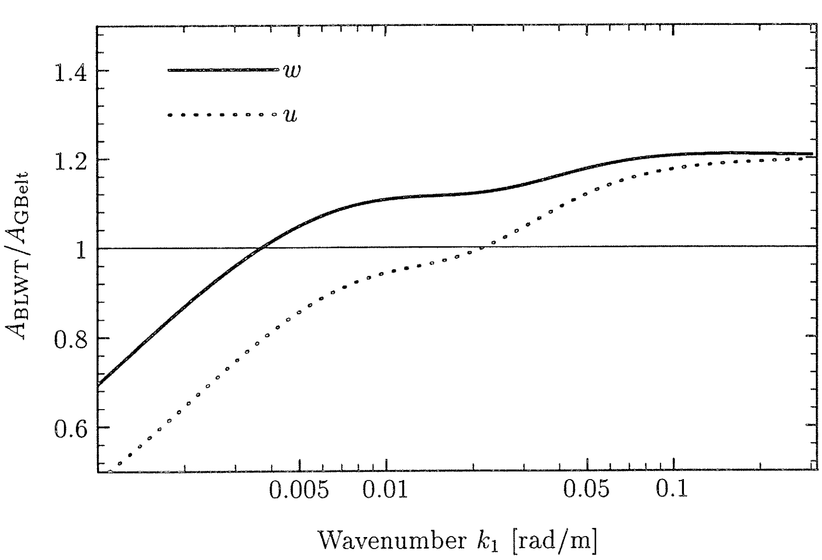

FIGURE 13. Ratio of 'idealized response amplitudes' (3.3) as a function of wavenumber.

modes. Both are shown in figure 13. It is seen that the w-excited modes in the wind tunnel are too large by a small amount for most frequencies.

According to Reinhold *et al.* (1992) the relevant eigen-frequencies of the bridge deck are between 0.05 Hz and 0.38 Hz. If we assume the relevant wind speeds to be between 30 and 56 m/s then the interesting wavenumbers will be in the interval 0.006 rad/m to 0.080 rad/m. According to figure 13, this implies that the w-excited modes most probably are overestimated due to the imperfectly simulated wind tunnel turbulence, while the energy in the u-excited modes are better estimated.

3.3. *Conclusion*

Turbulence from the wide boundary layer wind tunnel at DMI has been compared to measurements from the Great Belt.

The US model of Part IA fits the measured wind tunnel spectra well and predicts the cross-spectra almost perfectly (figures 14 to 16). The US model is used to predict that in the wavenumber interval of interest for dynamic load calculation (~0.006 rad/m to 0.080 rad/m) under very simplistic assumptions about the interaction between turbulence and the motion of the bridge deck, the amplitudes of the oscillation modes are slightly overestimated by up to 20% (for modes excited by the w component, see figure 13).

However, there are two major systematic uncertainties in this estimate. Firstly, the tensor model does not fit the Great Belt data perfectly as seen from figure IA.7. Secondly, the Great Belt spectra has been extrapolated up to $U = 58$ m/s by assuming that the turbulence intensity is independent of U as in Larsen *et al.* (1991). The assumption of constant turbulence intensity is fairly obvious for fixed surfaces but the surface of the sea changes as the wind speed grows, which can affect the turbulence intensity. I have used a simple model of how the sea surface reacts to the wind, Charnock's relation (Charnock 1955), to estimate the increase in turbulence intensity. From 25 m/s to 58 m/s it increases by roughly 20% (assuming that the ratio between σ^2 and $\langle uw \rangle$ is constant), which should be added the amplitudes estimated from the Great Belt data. This may cancel the 20% overestimation seen in figure 13 for the w-excited modes.

Under the very simple assumptions relating turbulence to mode amplitude (3.2) it seems – taking the uncertainties mentioned above into account – that scaled amplitudes at the relevant frequencies will lie within ±30% of amplitudes of the real bridge, if all other physics is being perfectly scaled and modeled.

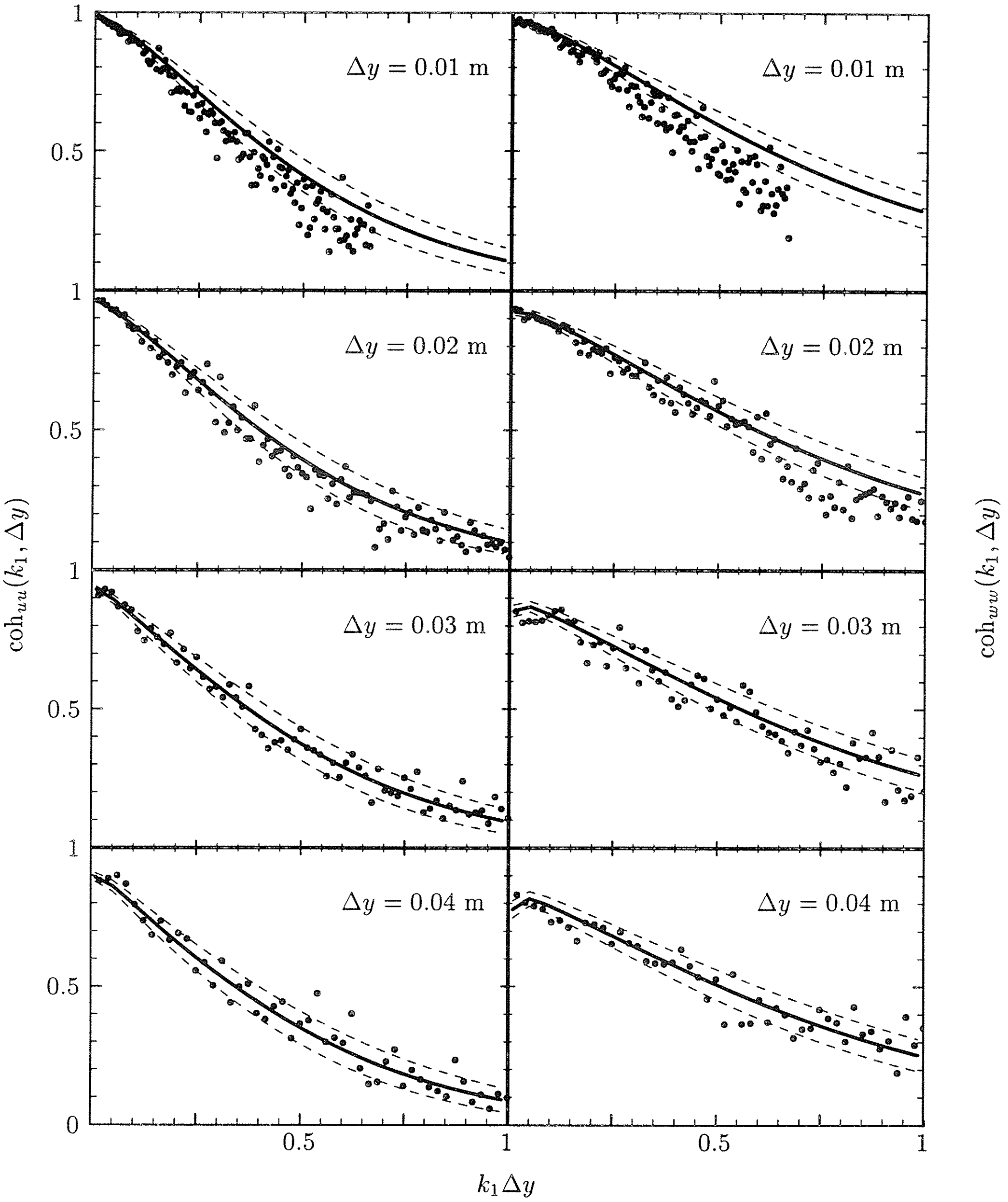

FIGURE 14. Measured coherences from the wind tunnel (dots) and predicted coherences (solid curves) as a function of $k_1\Delta y$. The dashed curves are the expected 1-σ deviation from the predicted coherences according to (IA.4.6). The left column is the u-coherences, the right the w-coherences. The separation of the cross-wires is indicated on each plot.

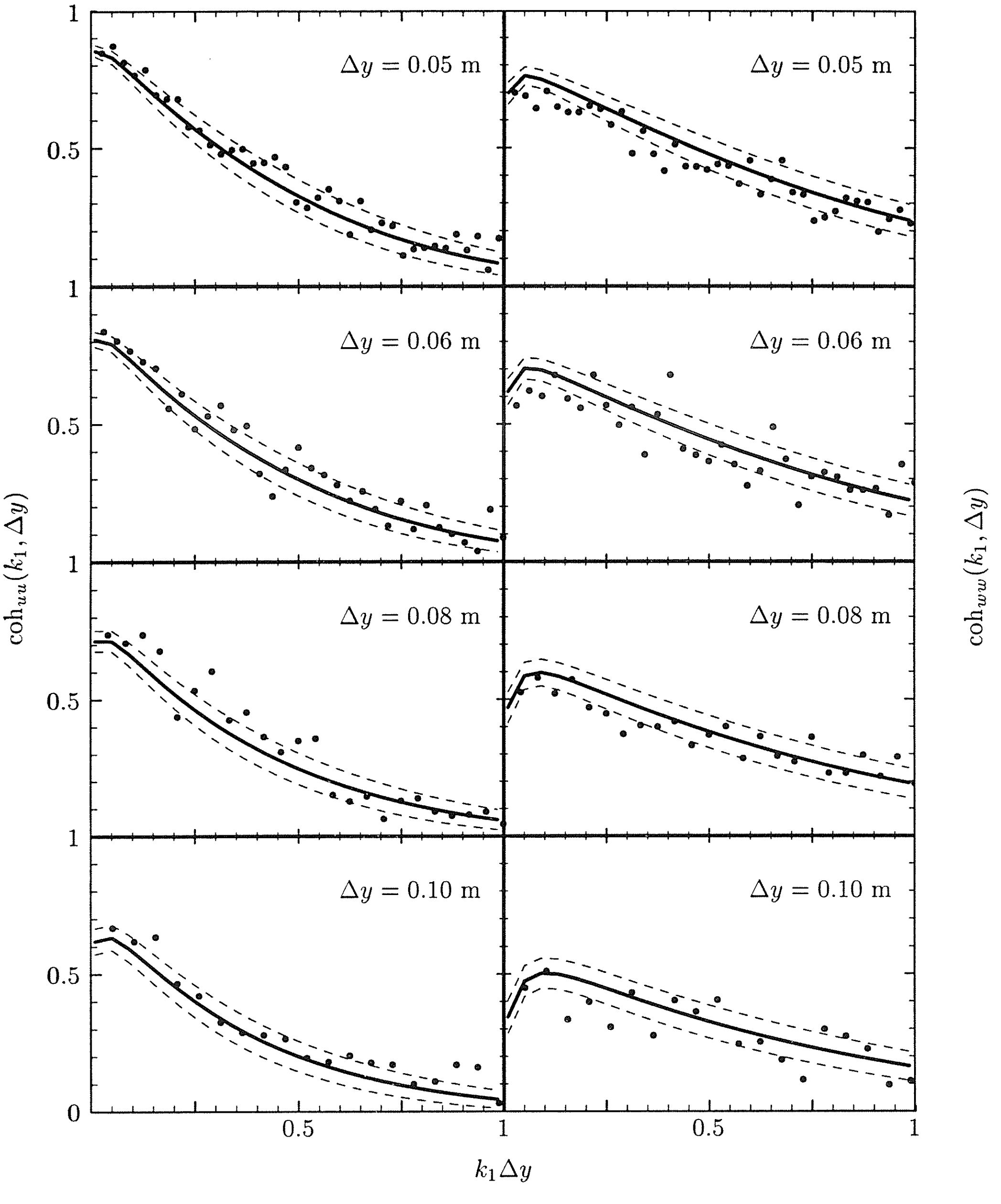

FIGURE 15. See caption of figure 14.

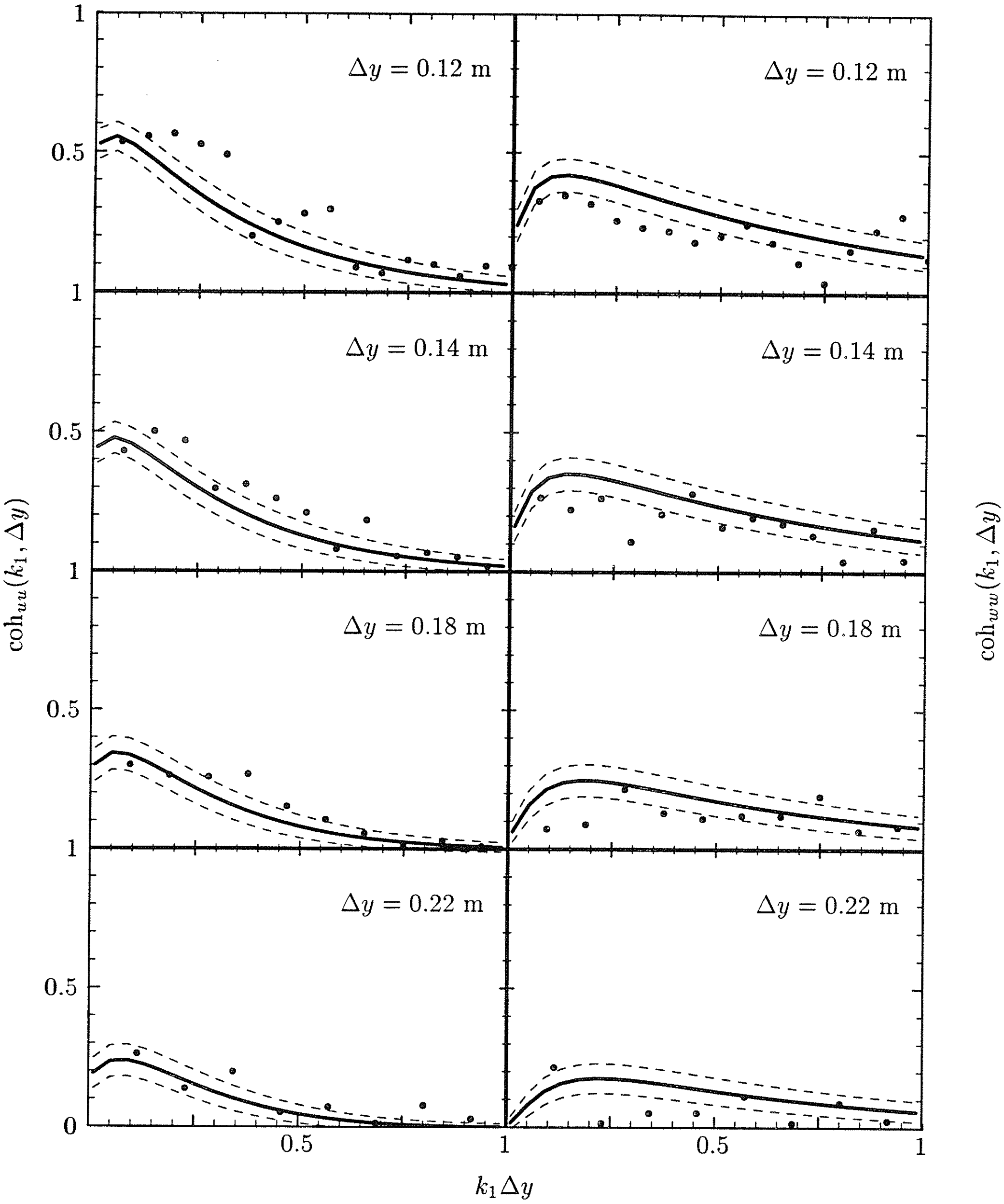

FIGURE 16. See caption of figure 14.

REFERENCES

CHARNOCK, H. 1955 Wind stress on a water surface *Q. J. Roy. Meteorol. Soc.*, **81**, 639–640.

DAVENPORT, A. G., KING, J. P. C. & LAROSE, G. L. 1992 Taut strip model tests. In *Aerodynamics of Large Bridges*, ed. A. Larsen, A.A. Balkema.

KAIMAL, J. C., GAYNOR, J. E., ZIMMERMAN, H. A. & ZIMMERMAN, G. A. 1990 Minimizing flow distortion errors in a sonic anemometer *Boundary-Layer Meteorol.*, **53**, 103–115.

KRETZ, A., MADSEN, H. AA., PETERSEN, J. T. 1994 Measured and Simulated Turbulence – Compared at a Section of a Rotating Wind Turbine Blade, *Risø Report No. R-671*, 98 pp (draft).

LARSEN, S. E. 1986 Hot-wire Measurements of Atmospheric Turbulence Near the Ground *Risø Report No. R-233*, 342 pp.

LARSEN, S. E., COURTNEY, M. S., HANSEN, F. AA., HØJSTRUP, J. & JENSEN, N. O. 1991 Measurement of turbulence intensity and power spectra at Sprogø – April 1989 – April 1990, *Risø Report No. M-2898.*

REINHOLD, T. A., BRINCH, M. & DAMSGAARD, AA. 1992 Wind tunnel tests for the Great Belt Link. In *Aerodynamics of Large Bridges*, ed. A. Larsen, A.A. Balkema.

SHINOZUKA, M. & JAN, C.-M. 1972 Digital Simulation of Random Processes and its Applications, *Journal of Sound and Vibration*, **25** (1), 111-128.

SMITT. L. W. & BRINCH, M. 1992 A new wide boundary layer wind tunnel at the Danish Maritime Institute. In *Aerodynamics of Large Bridges*, ed. A. Larsen, A.A. Balkema.

VEERS, P. S. 1988 Three-Dimensional Wind Simulation, Sandia National Laboratories, SAND88-0152.

WINKELAAR, D. 1991 Fast Three Dimensional Wind Simulation and the Prediction of Stochastic Blade Loads, In *Proceedings from the 10'th ASME Wind Energy Symposium, Houston.*

WYNGAARD, J. C. & COTÉ, O. R. 1972 Co-spectral similarity in the atmospheric surface layer. *Quart. J. R. Met. Soc.*, **98**, 590–603.

PART IIA:

How long is long enough when measuring fluxes and other turbulence statistics?

By **D.H. LENSCHOW, J. MANN[†] AND L. KRISTENSEN[†]**
National Center for Atmospheric Research[‡], Boulder, Colorado 80307

(Accepted for publication in *Journal of Atmospheric and Oceanic Technology*)

We determine how long a time series must be to estimate covariances and moments up to fourth order with a specified statistical significance. For a given averaging time T there is a systematic difference between the true flux or moment and the ensemble average of the time means of the same quantities. This difference, which we call the systematic error, is a decreasing function of T tending to zero for $T \to \infty$. The variance of the time mean of the flux or moment, the so-called error variance, represents the random scatter of individual realizations which, when T is much larger the integral time scale $\mathcal{T}$ of the time series, is also a decreasing function of T. This makes it possible to assess the minimum value of T necessary to obtain systematic and random errors smaller than specified values. Assuming that the time series are either Gaussian processes with exponential correlation functions or a skewed process derived from a Gaussian, we obtain expressions for the systematic and random errors. These expressions show that the systematic error and the error variance in the limit of large T are both inversely proportional to T which means that the random error, i.e. the square root of the error variance, will in this limit be larger than the systematic error. We demonstrate theoretically, as well as experimentally with aircraft data from the convective boundary layer over the ocean and over land, that the assumption that the time series are Gaussian leads to underestimation of the random errors, while derived processes with a more realistic skewness and kurtosis give better estimates. For fluxes we estimate the systematic and random errors when the time series are sampled instantaneously, but the samples separated in time by an amount Δ. We find that the random error variance and the systematic error increase by less than 8% over continuously-sampled data if Δ is no larger than the integral scale obtained from the flux time series and the co-spectrum, respectively.

1. Introduction

A fundamental tool in studying turbulence processes is the use of statistical moments to describe the properties of a field of turbulent fluctuations. Ideally the statistical moments should be determined by ensemble averaging, but in practical experimental situations

---

[†] Permanent affiliation: Risø National Laboratory, 4000 Roskilde, Denmark.

[‡] The National Center for Atmospheric Research is sponsored by the National Science Foundation.

this is not possible. Instead, the moments are estimated by a finite number of sample averages over a finite time period. Since theoretical treatments of turbulence often assume ensemble-averaged statistical moments, it is an important practical consideration to be able to estimate the difference between measured moments and the idealized ensemble-averaged moments that they are assumed to represent.

Recent observational studies such as the First ISLSCP† Field Experiment (FIFE) and the Atmospheric Boundary Layer Experiments (ABLE) have renewed interest in examining the significance of turbulence statistics measurements. This interest is related to such issues as the effects of changes in greenhouse gas concentrations on climate and on understanding the interaction of vegetated land surfaces with the atmosphere (Lenschow and Hicks, 1989). One example of the importance of this issue is the observation by Betts *et al.* (1990), Kelly *et al.* (1992), and Grossman (1992) of a significant reduction in airplane-measured scalar fluxes in FIFE due to inadequate length of flight legs and high-pass filtering.

Another example is the comparison of large-eddy simulation (LES) and direct simulation results with observations. For example, measurements of third-order moments do not always agree with LES, and in some cases it is not clear whether the differences are statistically significant. Moeng and Rotunno (1990), for example, have carried out direct simulations of buoyancy-driven turbulence and found that their simulations differ significantly from observations in a convective boundary layer. Similarly, large-eddy simulations of the convective atmospheric boundary layer (Schmidt and Schumann, 1989; Mason, 1989) make predictions about the behavior of turbulence statistics, and again differences between simulated and observed values, particularly for third moments, are found. However, observations of the third-order moment contain considerable scatter and are difficult to measure accurately. LeMone (1990) discusses some observations of skewness and possible sources of error in skewness measurements. Her approach is to investigate the effects of specific mesoscale phenomena in altering skewness rather than a general approach for estimating the significance of measurements of higher-order moments.

For these reasons, we have carried out a detailed evaluation of the error generated in second-, third-, and fourth-order moments of a single variable, and in covariances of two variables (e.g. fluxes) due to using measured time series of limited length to estimate the ensemble statistics. This error contains both a systematic and a random contribution. We also consider the additional error introduced by selecting an equally-spaced subset of the original time series from which the covariance is computed. Practical applications of this include: 1) use of sampling technology to grab an instantaneous sample of air whose constituents can then be measured in a more leisurely fashion with slower-responding sensors than required for direct measurements of the covariance without compromising the frequency response of the measurement (Cooper, 1993); and 2) it may be possible to reduce the amount of data to be stored without increasing the error in the covariance estimates. We then compare the theoretical expressions with errors calculated from airplane measurements of vertical air velocity and temperature.

In the following analysis we consider only stationary time series. This implies that they must be of infinite duration. Real time series are, of course, never strictly stationary and very often they are far from it. For example, they often have significant trends, and often

† International Satellite Land Surface Climatology Project

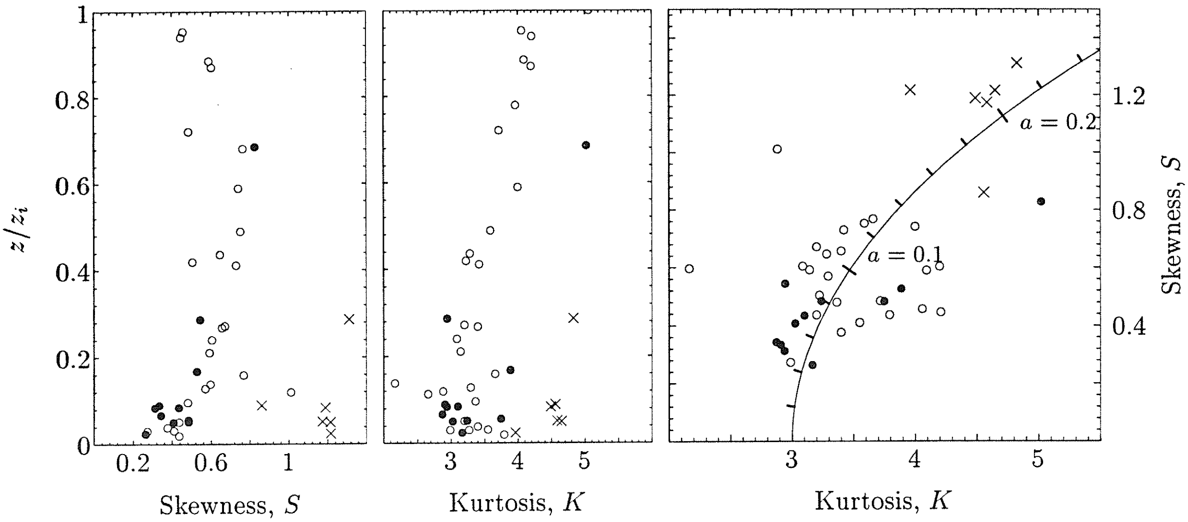

FIGURE 1. Open circles are values of skewness and kurtosis of w from the flight legs used by Lenschow and Stankov (1986) in their analyses of length scales. Most of the legs are from the Air Mass Transformation Experiment (AMTEX); a few are from NCAR Queen Air flight legs over eastern Colorado and over the Gulf of Mexico. The flight legs varied from 42 to 170 km in length. Closed circles (w) and crosses (θ) are the values from the flight legs used used in the analyses presented here, which are about 180 km in length. The right panel has the same data plotted as K vs. S. The parametric curve shows the skewness and kurtosis for the process (2.19) as a function of the parameter a.

---

random fluctuations have a different character at different regions in the time series. We often then assume that the given time series is a part of an infinitely long stationary time series, but that the given time series is too short for all these large-scale features to be statistically resolved. For this reason, real time series are often preprocessed to eliminate or suppress these large-scale features. Examples of preprocessing are *trend removal*, *time-dependent scaling or 'windowing'* and *high-pass filtering*. Dealing with this inevitability of the real world requires skill, experience and some a priori knowledge of the phenomenon under investigation to preprocess time series in such a way that the physical information is minimally corrupted.

The problem of estimating the statistical errors of higher moments has been addressed before by Lumley and Panofsky (1964). Their results have been discussed and applied by e.g. Wyngaard (1973) and Sreenivasan *et al.* (1978). As we discuss here, their approach differs from ours in that they do not separate systematic errors from random errors. It is quite natural to make this separation because averaged moments of second and higher order are functions of the averaging time (or length) and therefore systematically different from the theoretical ensemble values, which we can imagine to be the result of infinite averaging time. Furthermore, they only predict errors of second- and fourth-order moments, not third.

2. Systematic Errors

In the following we separate the analysis into moments of one variable and moments of more than one variable. In the first category we deal with second, third and fourth moments, whereas in the second we discuss only second moments, i.e. co-variances or fluxes.

2.1. *Single Time Series Moments*

We consider an ergodic and consequently stationary time series $w(t)$ with the ensemble mean removed for notational convenience, i.e.

$$\langle w(t)\rangle = 0. \tag{2.1}$$

The ensemble mean is in experimental situations estimated by the time average

$$w_T = \frac{1}{T}\int_{-T/2}^{T/2} w(t)dt, \tag{2.2}$$

which in general is different from $\langle w(t)\rangle$. However, taking the ensemble average of (2.2) implies

$$\langle w_T\rangle = \langle w(t)\rangle = 0. \tag{2.3}$$

By the assumption of ergodicity,

$$\lim_{T\to\infty} (w_T) = \langle w(t)\rangle. \tag{2.4}$$

The nth-order central moment is

$$\mu_n = \langle (w - \langle w\rangle)^n\rangle = \langle w^n\rangle, \tag{2.5}$$

which, in analogy to (2.2), is determined experimentally by time averaging, viz.

$$\mu_n(T) = \frac{1}{T}\int_{-T/2}^{T/2} (w(t) - w_T)^n dt. \tag{2.6}$$

In general, when $n > 1$

$$\langle \mu_n(T)\rangle \neq \mu_n.$$

For the second-order moment we get

$$\begin{aligned}\langle \mu_2(T)\rangle &= \frac{1}{T}\int_{-T/2}^{T/2} \langle (w(t) - w_T)^2\rangle dt \\ &= \mu_2 - \frac{1}{T^2}\int_{-T/2}^{T/2} dt_1 \int_{-T/2}^{T/2} dt_2 \langle w(t_1)w(t_2)\rangle.\end{aligned} \tag{2.7}$$

Since there will subsequently be several definite, multi-dimensional integrals of the type occurring in (2.7), we introduce the short-hand notation for the n-dimensional, dimensionless integral operator:

$$\int \equiv \frac{1}{T^n}\int_{-T/2}^{T/2} dt_1 \int_{-T/2}^{T/2} dt_2 \cdots \int_{-T/2}^{T/2} dt_n. \tag{2.8}$$

Using this new convention, we get for the third- and fourth-order moments

$$\langle \mu_3(T)\rangle = \mu_3 - 3\int \langle w^2(t_1)w(t_2)\rangle + 2\int \langle w(t_1)w(t_2)w(t_3)\rangle. \tag{2.9}$$

and

$$\langle \mu_4(T) \rangle = \mu_4 - 4\int \langle w^3(t_1)w(t_2)\rangle + 6\int \langle w^2(t_1)w(t_2)w(t_3)\rangle$$
$$- 3\int \langle w(t_1)w(t_2)w(t_3)w(t_4)\rangle. \tag{2.10}$$

We define the auto-covariance function $R_{ww}(\tau)$ and the auto-correlation function $\rho(\tau)$ by

$$R_{ww}(t_2 - t_1) = \langle w(t_1)w(t_2)\rangle \tag{2.11}$$

and

$$\mu_2\rho(t_2 - t_1) = R_{ww}(t_2 - t_1) \tag{2.12}$$

which, due to ergodicity and consequently, stationarity, are even functions of only one variable, namely the time lag $\tau = t_2 - t_1$. From this it follows that the double integral in (2.7) can be reduced to a single integral,

$$\frac{\langle \mu_2(T)\rangle}{\mu_2} = 1 - \frac{2}{T}\int_0^T \left(1 - \frac{\tau}{T}\right)\rho(\tau)d\tau \tag{2.13}$$

and in the limit $T \gg \mathcal{T}$,

$$\frac{\langle \mu_2(T)\rangle}{\mu_2} \approx 1 - 2\frac{\mathcal{T}}{T}, \tag{2.14}$$

where

$$\mathcal{T} = \int_0^\infty \rho(t)dt \tag{2.15}$$

is the integral time scale.

In order to estimate $\langle \mu_3(T)\rangle$ and $\langle \mu_4(T)\rangle$ we use the approximation that the signal can be derived from a Gaussian process. In the case of $\langle \mu_4(T)\rangle$, we assume that the signal itself is a Gaussian process. This implies that the Isserlis relation (Koopmans, 1974)†

$$\begin{aligned}\langle w(t_1)w(t_2)w(t_3)w(t_4)\rangle = \; & \langle w(t_1)w(t_2)\rangle\langle w(t_3)w(t_4)\rangle \\ & + \langle w(t_1)w(t_3)\rangle\langle w(t_2)w(t_4)\rangle \\ & + \langle w(t_1)w(t_4)\rangle\langle w(t_2)w(t_3)\rangle\end{aligned} \tag{2.16}$$

can be applied to (2.10) to obtain in the limit $T \gg \mathcal{T}$

$$\frac{\langle \mu_4(T)\rangle}{\mu_4} \approx 1 - 4\frac{\mathcal{T}}{T}. \tag{2.17}$$

Lenschow, Mann and Kristensen (1993) (LMK) present the exact evaluation of (2.7) or (2.13) together with the fourth-order systematic error for all values of T assuming an exponential autocorrelation function

$$\rho(\tau) = \exp(-|\tau|/\mathcal{T}), \tag{2.18}$$

see also (A 1) and (A 2) in appendix A.

When evaluating (2.9), we obtain the trivial result that $\langle \mu_3(T)\rangle$, as well as all other odd moments, are zero if we assume that $w(t)$ is a Gaussian process. Most real processes

---

† The Isserlis relation states that, in general, the $2n$th-order moment can be reduced to a sum of $(2n-1)!!$ terms, where $(2n-1)!! \equiv (2n-1) \times (2n-3) \times (2n-5) \times \cdots \times 3 \times 1$, each of which is a product of $n/2$ second-order moments.

in the boundary layer are non-Gaussian. Therefore, to estimate the systematic error of odd moments in particular, we use a non-Gaussian process with skewness and kurtosis different from zero and three, respectively. A simple way to construct such a process is by modifying a Gaussian process $z(t)$ with variance σ_0^2 and an exponential auto-correlation function such that

$$w(t) = z(t) + a\frac{z^2(t) - \langle z^2(t)\rangle}{\sigma_0}. \tag{2.19}$$

Using the Isserlis relation, it is easily seen that the skewness and kurtosis of $w(t)$ are:

$$\begin{aligned} S &\equiv \frac{\mu_3}{\mu_2^{3/2}} = \frac{2a(3+4a^2)}{(1+2a^2)^{3/2}} \\ K &\equiv \frac{\mu_4}{\mu_2^2} = \frac{3(1+20a^2+20a^4)}{(1+2a^2)^2}. \end{aligned} \tag{2.20}$$

Realistic values of a are between 0 and 0.1 for the vertical velocity w and around 0.2 for the temperature θ as seen from the right panel of Fig. 1, where values of skewness and kurtosis from the flight legs used by Lenschow and Stankov (1986) in their analysis of length scales as well as the flight legs used here, are displayed together with a parametric curve of $\{K(a), S(a)\}$ from (2.20). LMK derive the asymptotic systematic errors ($T \gg \mathcal{T}$) for all higher order moments of the skewed process (2.19), see also appendix B. The error of the third-order moment becomes

$$\left(\mu_3 - \langle\mu_3(T)\rangle\right)/\mu_3 = 3\left(2 - \frac{1}{(1+a^2)(3+4a^2)}\right)\frac{\mathcal{T}}{T} \tag{2.21}$$

which is between $5\mathcal{T}/T$ and $6\mathcal{T}/T$. The systematic errors of the second- and fourth-order moments are not very different from the Gaussian results (2.14) and (2.17). (See Table 6 and §B.4.)

2.2. *Fluxes*

It is straightforward to generalize the preceeding discussion to more than one signal. It is of particular interest to extend the analysis to second-order moments of two random variables such as the vertical flux of a scalar $s(t)$. In this case $w(t)$ is the vertical velocity. Let us assume that $s(t)$ has a zero ensemble mean. Then (2.1) – (2.4) apply to $s(t)$ as well as $w(t)$. The second-order moment, i.e. the flux, is defined as

$$F \equiv \langle w(t)s(t)\rangle. \tag{2.22}$$

Experimentally, the flux is determined as the time average

$$F(T) = \int \{w(t) - w_T\}\{s(t) - s_T\}. \tag{2.23}$$

In general the ensemble average of $F(T)$ will be different from F. We get, in analogy to (2.13)

$$\langle F(T)\rangle = F - \int R_{ws}(t_2 - t_1), \tag{2.24}$$

where

$$R_{ws}(\tau) = \langle w(t)s(t+\tau)\rangle \tag{2.25}$$

is the covariance function of $w(t)$ and $s(t)$. If we define an integral time scale

$$\mathcal{T}_{ws} = \frac{1}{F} \int_0^\infty R_{ws}(\tau) d\tau \tag{2.26}$$

in analogy to the integral time scale for a single variable (2.15), then (2.24) can be written as

$$\frac{F - \langle F(T) \rangle}{F} \approx 2 \frac{\mathcal{T}_{ws}}{T} \tag{2.27}$$

for $T \gg \mathcal{T}_{ws}$.

LMK discuss the difficulties in the experimental determination of $\mathcal{T}_{ws}$, which in some cases becomes negative. They therefore derive an inequality giving an upper bound on the systematic error in terms of the integral time scale of the vertical velocity $\mathcal{T}$, the integral scale of the scalar fluctuations $\mathcal{T}_s$, and the variances of these quantities; μ_2 and μ_s:

$$\frac{|F - \langle F(T) \rangle|}{\sqrt{\mu_2 \mu_s}} \leq 2 \frac{\sqrt{\mathcal{T} \mathcal{T}_s}}{T}. \tag{2.28}$$

Substituting the correlation coefficient $r_{ws} \equiv F / \sqrt{\mu_2 \mu_s}$ into (2.28),

$$\frac{|F - \langle F(T) \rangle|}{F} \leq \frac{2}{r_{ws}} \frac{\sqrt{\mathcal{T} \mathcal{T}_s}}{T}. \tag{2.29}$$

LMK also derive an exact expression for the error assuming $R_{ws}(\tau)$ to be exponential, given by $R_{ws}(\tau) \equiv F \rho_{ws}(\tau) = F \exp(-|\tau| / \mathcal{T}_{ws})$, in analogy to (2.18):

$$\frac{F - \langle F(T) \rangle}{F} = \frac{2}{x} - \frac{2}{x^2} + \frac{2}{e^x x^2}. \tag{2.30}$$

where $x = T / \mathcal{T}_{ws}$.

3. Random Errors

When averaging over a finite time T the time means of moments will, in general, differ from each other and from the ensemble means; that is, they are randomly scattered. As in the case of systematic errors, we discuss higher moments of one quantity and fluxes separately.

3.1. *Single Time Series Moments*

In the case of the nth-order central moment of $w(t)$, the individual realizations in an ensemble will be distributed around $\langle \mu_n(T) \rangle$ with an error variance

$$\sigma_n^2(T) = \langle (\mu_n(T) - \langle \mu_n(T) \rangle)^2 \rangle. \tag{3.1}$$

If we, for measuring purposes, want to determine how long we need to average in order to get a stable time-averaged value $\mu_n(T)$, i.e. to get an error variance smaller than a specified value, we must find a way to estimate (3.1). Lenschow and Kristensen (1985) show that if the signal is a Gaussian process, for $T \gg \mathcal{T}$

$$\sigma_2^2(T) \approx 4 \frac{\mu_2^2}{T} \int_0^\infty \rho^2(\tau) d\tau. \tag{3.2}$$

Similarly, taking only the first-order terms in $\mathcal{T}/T$, we get for third- and fourth-order moments

$$\sigma_3^2(T) \approx 12\frac{\mu_2^3}{T}\int_0^\infty \rho^3(\tau)d\tau. \tag{3.3}$$

and

$$\sigma_4^2(T) \approx 48\frac{\mu_2^4}{T}\int_0^\infty \{3\rho^2(\tau) + \rho^4(\tau)\}d\tau. \tag{3.4}$$

Again we assume that the autocorrelation function can be represented with sufficient accuracy by the exponential (2.18). Therefore, we have

$$\int_0^\infty \rho^n(\tau)d\tau = \mathcal{T}/n, \tag{3.5}$$

and thus obtain the error variance estimates

$$\sigma_2^2(T) \approx 2\mu_2^2\frac{\mathcal{T}}{T}, \tag{3.6}$$

$$\sigma_3^2(T) \approx 4\mu_2^3\frac{\mathcal{T}}{T} \tag{3.7}$$

and

$$\sigma_4^2(T) \approx 84\mu_2^4\frac{\mathcal{T}}{T} \qquad \text{or} \qquad \sigma_4^2(T) \approx \frac{84}{9}\mu_4^2\frac{\mathcal{T}}{T}. \tag{3.8}$$

LMK (see appendix A) derive exact equations valid for all T for $\sigma_2^2(T)$, $\sigma_3^2(T)$ and $\sigma_4^2(T)$ assuming a Gaussian process and that (3.5) is valid. These exact error variances, normalized by μ_2 to the appropriate powers, are shown in Figs. 6, 7 and 8 (dashed lines). We note that the error variances actually go to zero as $T/\mathcal{T}$ goes to zero. Here the systematic errors correspondingly become very large.

Comparing these results with those obtained by Lumley and Panofsky (1964), and later discussed by Wyngaard (1973), we note that they state the problem of statistical uncertainty somewhat differently. We derive error variances of central moments of a time series, while they discuss powers of time series which do not have a zero time average. In other words, we extract the leading term of (3.1) for $T \gg \mathcal{T}$ in the form

$$\sigma_n^2(T) = \left\langle \left\{ \int [(w(t) - w_T)^n - \langle (w(t) - w_T)^n \rangle] \right\}^2 \right\rangle, \tag{3.9}$$

whereas Lumley and Panofsky (1964) based their asymptotic expressions on

$$\sigma_n^2(T)_{LP} = \left\langle \left\{ \int [w^n(t) - \langle w^n(t) \rangle] \right\}^2 \right\rangle. \tag{3.10}$$

Furthermore, they use the time scale (2.15) as the pertinent integral scale for $w^n(t)$, irrespective of the value of n, whereas we have assumed the exponential autocorrelation function (2.18) and consequently obtained our integral time scale from (3.5).

In our notation, using our definition of the integral time scale, we find $\sigma_n^2(T)_{LP} = \sigma_n^2(T)$ for Gaussian processes when n is even. This is not the case when n is odd. For example, the asymptotic error variance of the third moment, based on (3.10) and (3.5), is

$$\sigma_3^2(T)_{LP} = 22\mu_2^3\frac{\mathcal{T}}{T} = 5.5\sigma_3^2(T). \tag{3.11}$$

For odd moments with n larger than 3 the ratio between $\sigma_n^2(T)_{LP}$ and $\sigma_n^2(T)$ decreases with n. For instance, for $n = 5$ this ratio is very close to 2, and very close to 4/3 for $n = 7$.

In contrast to the systematic errors, the random errors are significantly affected by the introduction of a realistic skewness and kurtosis using (2.19). These modified error variances corresponding to (3.6), (3.7) and (3.8) are derived in LMK (and appendix A) and summarized in Table 6 normalized by μ_n^2, as well as in Figs. 6, 7, 8 and also Table 6 normalized by μ_2^n. The same relative error in the second-order moment requires an average twice as long for a skewed process ($a = 0.2$, in (2.19)) compared to a Gaussian process ($a = 0$).

3.2. *Fluxes*

In analogy to (3.1), we define the error variance of the flux as

$$\sigma_F^2(T) \equiv \langle \{F(T) - \langle F(T) \rangle\}^2 \rangle. \tag{3.12}$$

Inserting (2.23), we find

$$\sigma_F^2(T) = \int \langle f^T(t_1) f^T(t_2) \rangle, \tag{3.13}$$

where

$$f^T(t) = \{w(t) - w_T\}\{s(t) - s_T\} - \langle \{w(t) - w_T\}\{s(t) - s_T\} \rangle \tag{3.14}$$

is a time series with zero ensemble mean and defined only in the interval $-T/2 \leq t \leq T/2$. In the limit $T \to \infty$, (3.14) becomes a stationary time series

$$f^\infty(t) = w(t)s(t) - \langle w(t)s(t) \rangle. \tag{3.15}$$

In analogy to the derivation of the error variance of one signal LMK show that if the variables $w(t_1)$, $s(t_2)$, $w(t_3)$ and $s(t_4)$ have a joint Gaussian probability distribution the error variance for $T \gg \mathcal{T}_f$ becomes

$$\sigma_F^2(T) \approx 2\mu_f \frac{\mathcal{T}_f}{T}, \tag{3.16}$$

where μ_f and $\mathcal{T}_f$ are the variance and the integral time scale, respectively, of the time series $f^\infty(t)$.

The relative error, which is the square root of the random error variance normalized by F^2 can be estimated from (3.16), after first using the Isserlis relation to expand the fourth-order moment, μ_f, as follows:

$$\mu_f = \mu_2 \mu_s + F^2 \Rightarrow \frac{\mu_f}{F^2} = \frac{1 + r_{ws}^2}{r_{ws}^2}. \tag{3.17}$$

Thus, the relative error is

$$\frac{\sigma_F(T)}{|F|} = \left(\frac{2\mathcal{T}_f}{T} \right)^{1/2} \left(\frac{1 + r_{ws}^2}{r_{ws}^2} \right)^{1/2}. \tag{3.18}$$

In parallel to the upper limit of the systematic error (2.29), Lenschow and Kristensen (1985) derive an upper limit to the error variance of the flux

$$\frac{\sigma_F(T)}{|F|} \leq 2 r_{ws}^{-1} \left[\frac{\min(\mathcal{T}, \mathcal{T}_s)}{T} \right]^{1/2}, \tag{3.19}$$

expressed in terms of more commonly available integral time scales.

4. Disjunct Sampling of Fluxes

In the previous sections we have derived expressions for systematic and random errors of fluxes based on continuous sampling over finite periods with duration T. However, it is also of practical interest to experimentalists to know how many samples it is necessary to collect in the period T in order to keep the error below a specified level. In this case, we assume that the measurements are "instantaneous," i.e. that the instrument response time is much smaller compared to the integral scales of w and s, and are collected at equally-spaced time intervals Δ. Therefore, the error becomes a function of two time periods, T and Δ. This technique may preclude estimating spectra and integral time scales. However, the high-frequency contributions to the fluxes are retained at the possible expense of an increased systematic error and a larger statistical uncertainty.

This technique was proposed by Haugen (1978) for reducing the amount of data to be archived and to be used in computations of turbulence statistics while still maintaining acceptable error levels. Kaimal and Gaynor (1983) applied this procedure to data from BAO (Boulder Atmospheric Observatory) and called it "grab sampling". Some authors (Bendat and Piersol, 1986) refer to the process as "decimation". Still another application of the technique, proposed by Cooper (1993), is for estimating scalar fluxes using sensors with frequency responses that would not be adequate for straightforward flux measurement. With this technique, which Cooper calls "intermittent sampling," the samples are grabbed quickly in a time interval which determines the temporal resolution of the measurement; the scalar quantity is then measured over a longer period, compatible with the time response of the sensor. We suggest the term "disjunct sampling" for this process, since it conveys the interpretation of separation between data points, while decimation means literally taking every tenth sample and intermittency already has a quite separate meaning in the context of turbulent flows.

We illustrate these considerations, with only small modifications in the derivation from the case with continuous sampling, by considering measurements of the flux of a scalar $s(t)$ at equidistant time intervals Δ over a total record length T, although the technique is applicable to other turbulence statistics as well. The number of sampled points is

$$N = T/\Delta. \tag{4.1}$$

The time averages are now

$$w_{T,\Delta} = \frac{1}{N}\sum_{\ell=0}^{N-1} w(\ell\Delta), \tag{4.2}$$

$$s_{T,\Delta} = \frac{1}{N}\sum_{\ell=0}^{N-1} s(\ell\Delta). \tag{4.3}$$

The time average of the flux is, in analogy to (2.23),

$$F(T,\Delta) = \frac{1}{N}\sum_{\ell=0}^{N-1}\{w(\ell\Delta) - w_{T,\Delta}\}\{s(\ell\Delta) - s_{T,\Delta}\}. \tag{4.4}$$

The ensemble average of $F(T,\Delta)$ now becomes

$$\langle F(T,\Delta)\rangle = F - \frac{1}{N}\sum_{\ell_1=0}^{N-1}\frac{1}{N}\sum_{\ell_2=0}^{N-1}\langle w(\ell_1\Delta)s(\ell_2\Delta)\rangle \tag{4.5}$$

If we assume, as in the preceeding sections that the covariance function ρ_{ws} is exponential, then it is straightforward to evaluate (4.5) exactly for all values of $N = T/\Delta \geq 1$. We get

$$\frac{F - \langle F(T,\Delta)\rangle}{F}\frac{T}{\mathcal{T}_{ws}} = \\ \frac{\Delta}{\mathcal{T}_{ws}}\left\{\coth\left(\frac{\Delta}{2\mathcal{T}_{ws}}\right) - \frac{(\Delta/\mathcal{T}_{ws})(\mathcal{T}_{ws}/T)[1 - \exp(-T/\mathcal{T}_{ws})]}{2\sinh^2\left(\frac{\Delta}{2\mathcal{T}_{ws}}\right)}\right\} \tag{4.6}$$

The two asymptotes of the relative systematic error can be written, for $T \gg \mathcal{T}_{ws}$, as

$$\frac{F - \langle F(T,\Delta)\rangle}{F}\frac{T}{\mathcal{T}_{ws}} = \begin{cases} 2 & \text{for} \quad \Delta \ll \mathcal{T}_{ws} \\ \frac{\Delta}{\mathcal{T}_{ws}} & \text{for} \quad \Delta \gg \mathcal{T}_{ws} \end{cases} . \tag{4.7}$$

This result does not depend on the assumption of an exponential covariance function.

For disjunct sampling, the error variance becomes

$$\sigma_F^2(T,\Delta) = \frac{1}{N}\sum_{\ell_1=0}^{N-1}\frac{1}{N}\sum_{\ell_2=0}^{N-1}\langle f^\infty(\ell_1\Delta)f^\infty(\ell_2\Delta)\rangle + O(1/N^2). \tag{4.8}$$

which to first order in $\Delta/T = 1/N \ll 1$ becomes, for an exponential covarince function,

$$\frac{\sigma_F^2(T,\Delta)}{\mu_f}\frac{T}{\mathcal{T}_f} = \frac{\Delta}{\mathcal{T}_f}\coth\left(\frac{\Delta}{2\mathcal{T}_f}\right) \tag{4.9}$$

(see LMK for a derivation). Normalizing the error variance by $\mu_f\mathcal{T}_f/T$, the asymptotes can be written, for $T \gg \mathcal{T}_f$, as

$$\frac{\sigma_F^2(T,\Delta)}{\mu_f}\frac{T}{\mathcal{T}_f} = \begin{cases} 2 & \text{for} \quad \Delta \ll \mathcal{T}_f \\ \frac{\Delta}{\mathcal{T}_f} & \text{for} \quad \Delta \gg \mathcal{T}_f \end{cases} . \tag{4.10}$$

independent of the assumption of an exponential covariance function.

Equation (4.9) is used by Cooper (1993) in his uncertainty analysis. For $T \gg \mathcal{T}_{ws}$, the second term in (4.6) is negligible, so that the systematic and random errors have a similar dependence on the ratio of Δ and the appropriate integral scale.

5. Experimental Validation

Here we compare the theoretical expressions derived in the previous sections with moment errors calculated from actual time series. We use vertical air velocity, w, and temperature, θ, measured by the NCAR Electra aircraft during two field campaigns: 1) a set of ten 30-minute flight legs over the East China Sea during wintertime cold-air outbreaks over a relatively warm ocean surface, and 2) one 30-minute leg over land in the daytime convective boundary layer. The first campaign took place in February, 1975 as part of the Air Mass Transformation Experiment (AMTEX), which is described by Lenschow and Agee (1976). The second campaign (ELDOME) was carried out in May, 1988 over the sand-hill country of Western Nebraska, where the rolling hills (stabilized sand dunes) extend to a height of up to 80 m. We include this leg for comparison with the over-water flight legs from AMTEX. A summary of flight parameters is given in Table 1. Prior to the analysis, a linear trend was removed from all the time series to eliminate contributions from large-scale variability and instrument drift.

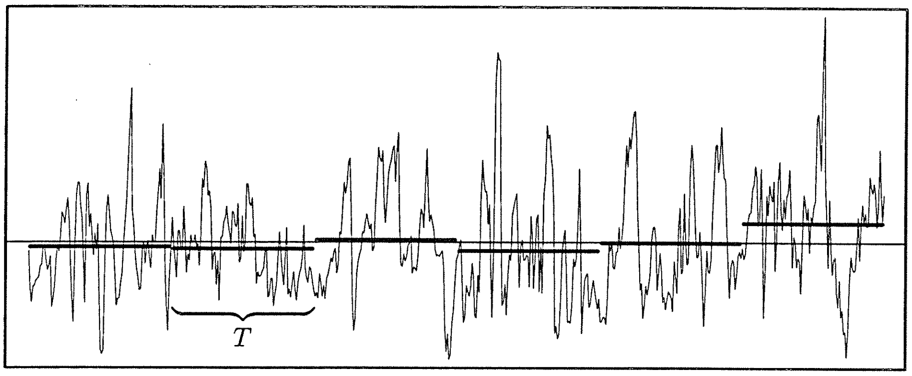

FIGURE 2. Subdivision of a time series in 'realizations' of length T.

For each of the flight legs we calculated the three moments μ_2, μ_3 and μ_4, the corresponding values of the skewness S and the kurtosis K, and the integral scale $\mathcal{T}$ for the vertical velocity w . The integral scale was obtained from the spectrum of w by a least squares fit to the function

$$\Phi_{ww}(\omega) = \frac{\mathcal{T}\mu_2}{\pi}\frac{1}{1+\omega^2\mathcal{T}^2}, \tag{5.1}$$

which is the Fourier transform of the autocorrelation function (2.18). The results of these calculations are shown in Table 2. We note that most of the integral time scales are about 1 s or less. However, two of the time series (AMTEX03 and AMTEX07) have time scales around 2 s. The values of z/z_i for these flight legs were 0.7 and 0.3, i.e. cruising heights well into the boundary layer.

The temperature signals, $\theta(t)$, were generally of lower quality than the velocity data and, as shown in Table 3 not all the temperature time series could be used because of noise and other instrument problems. In the remaining temperature time series the mesoscale structures were removed by a symmetric Gaussian high-pass filter with a time constant which was 100 times the integral time scale $\mathcal{T}$ of the concurrent w time series. This removes temperature fluctuations at scales larger than about 10 to 20 times the depth of the boundary layer z_i. After this filtering, the selected temperature time series were analyzed in the same way as w to obtain moments and the integral time scales $\mathcal{T}_s$. The results are shown in Table 3. The values of $\mathcal{T}_s$ are generally about 50% larger than for $\mathcal{T}$, in contrast to Lenschow and Stankov (1986) who obtained values of $\mathcal{T}_s$ about 6 times larger than $\mathcal{T}$. This is likely due to their use of unfiltered temperature time series (although they used legs mostly of from 50 to 100 km length) and their use of the autocorrelation function only up to the first zero crossing for computing the integral scale.

We then computed the co-spectrum of temperature and velocity and the power spectrum of the product time series (3.15) to obtain, by fitting to a spectrum of the type (5.1), the integral time scales $\mathcal{T}_{ws}$ and $\mathcal{T}_f$. These are presented in Table 4, together with the estimated values of the flux F and the variance μ_f of the the product.

Name	Date	Period Local time	Airspeed (m s^{-1})	z (m)	z_i (m)
AMTEX01	15-2-75	11:30–12:00	97.3	100	1200
AMTEX02	16-2-75	11:36–12:06	104.0	95	1430
AMTEX03	16-2-75	16:11–16:41	108.0	980	1430
AMTEX04	18-2-75	11:02–11:32	103.7	90	1010
AMTEX05	18-2-75	14:30–15:00	103.5	85	1010
AMTEX06	19-2-75	10:47–11:17	101.8	95	1842
AMTEX07	21-2-75	12:02–12:32	100.9	315	1100
AMTEX08	22-2-75	12:04–12:34	99.2	95	1900
AMTEX09	28-2-75	12:42–13:12	105.4	95	1700
AMTEX10	28-2-75	13:28–13:58	106.4	285	1700
ELDOME	12-5-88	14:12–14:42	101.0	70†	2950

† 30 - 100 m

TABLE 1. Time, true airspeed, height above the surface z and inversion height z_i for the airplane flight legs used in the data analysis.

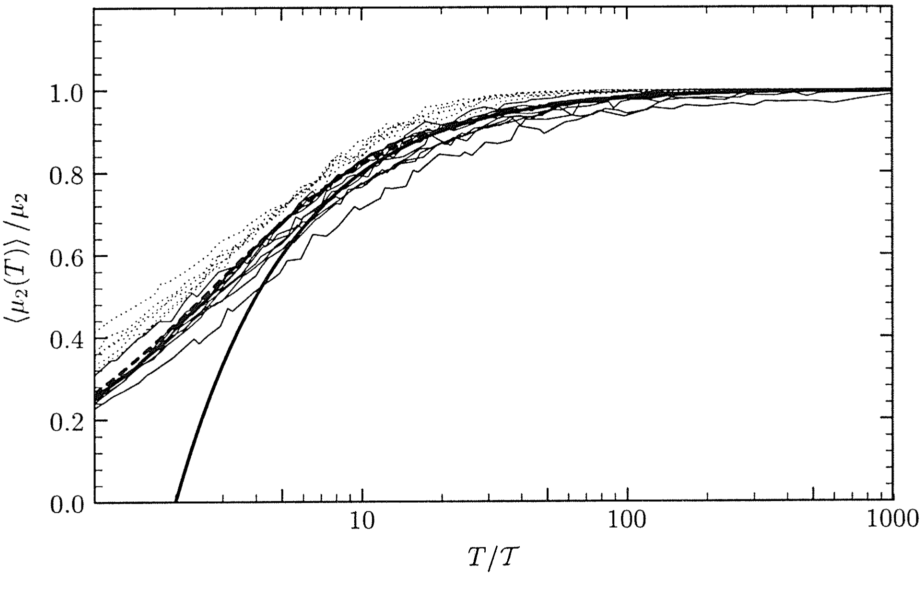

FIGURE 3. Normalized second-order moment of vertical velocity (solid lines) and temperature (dotted lines) versus observation time T divided by the timescale $\mathcal{T}$ or $\mathcal{T}_s$ (see Table 2 and 3). The broad solid line is the asymptotic expression, (2.14), the dashed almost obscured by the data curves is the exact expression valid for all $T/\mathcal{T}$ assuming exponential auto-correlation, (A 1).

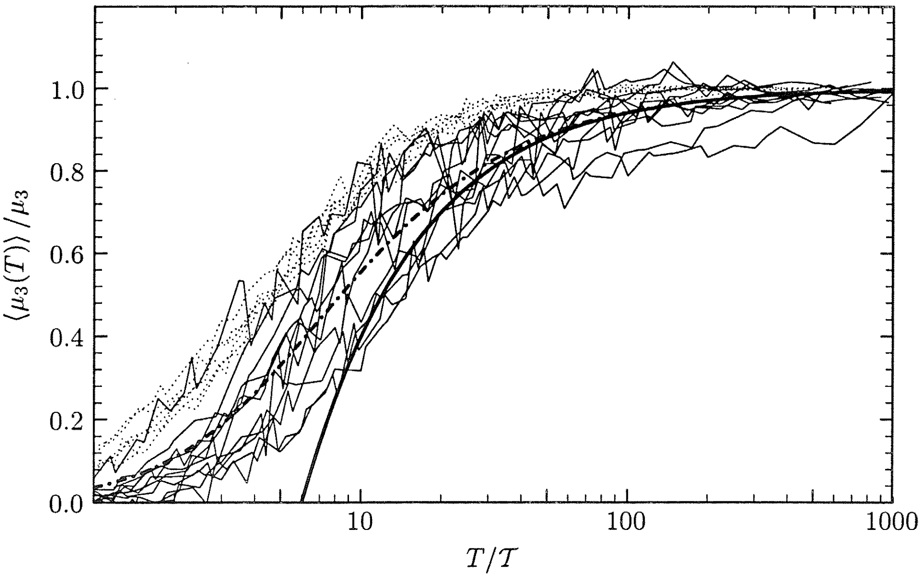

FIGURE 4. Normalized third-order moments. See caption of Figure 3. The solid line is the asymptotic expression, $1 - 6\mathcal{T}/T$ (from (B37) with $a = \infty$ in (2.19)), the dot-dashed the exact, (A3), also with $a = \infty$.

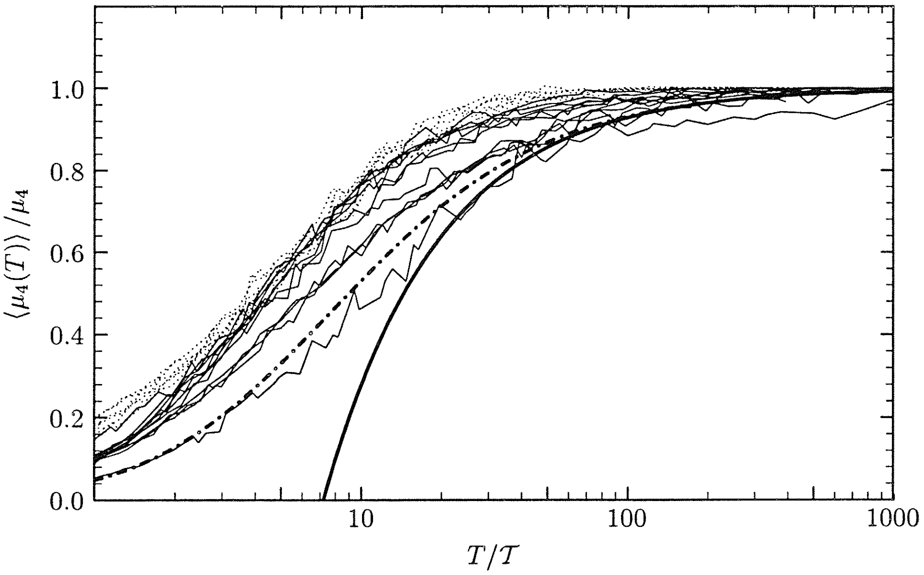

FIGURE 5. Normalized fourth-order moments. See caption of Figure 3. The solid line is the asymptotic expressions, (2.17), the dot-dashed the exact for the Gaussian process (A2).

Name	μ_2 $(\mathrm{ms}^{-1})^2$	μ_3 $(\mathrm{ms}^{-1})^3$	μ_4 $(\mathrm{ms}^{-1})^4$	S	K	$\mathcal{T}$ (s)
AMTEX01	1.060	0.342	3.303	0.313	2.938	1.045
AMTEX02	1.105	0.398	3.507	0.343	2.872	0.789
AMTEX03	1.122	0.983	6.326	0.827	5.022	2.504
AMTEX04	0.420	0.091	0.513	0.334	2.909	0.754
AMTEX05	0.576	0.190	1.030	0.434	3.100	0.681
AMTEX06	1.257	0.682	5.116	0.484	3.238	1.200
AMTEX07	1.963	1.496	11.339	0.544	2.943	1.879
AMTEX08	1.110	0.475	3.724	0.407	3.025	0.681
AMTEX09	0.213	0.047	0.170	0.483	3.747	0.583
AMTEX10	0.187	0.042	0.136	0.526	3.886	0.737
ELDOME	0.885	0.220	2.479	0.264	3.165	1.038

TABLE 2. Moments and integral scales of w for the analyzed flight legs.

Name	μ_2 (K^2)	μ_3 (K^3)	μ_4 (K^4)	S	K	$\mathcal{T}_s$ (s)
AMTEX01	0.0297	0.00610	0.00397	1.188	4.490	1.249
AMTEX04	0.00547	0.000348	0.000137	0.860	4.558	1.354
AMTEX06	0.0479	0.0123	0.0105	1.173	4.583	1.456
AMTEX07	0.0225	0.00441	0.00294	1.311	4.826	2.266
AMTEX08	0.0398	0.00964	0.00737	1.215	4.649	1.034
ELDOME	0.0470	0.0124	0.0110	1.216	3.962	1.528

TABLE 3. Moments and integral scales of θ for the analyzed flight legs.

Name	F ($\mathrm{ms}^{-1}\mathrm{K}$)	μ_f $(\mathrm{ms}^{-1}\mathrm{K})^2$	$\mathcal{T}_{ws}$ (s)	$\mathcal{T}_f$ (s)
AMTEX01	0.1073	0.0467	1.277	0.419
AMTEX04	0.0263	0.00370	0.982	0.306
AMTEX06	0.1534	0.1067	1.563	0.488
AMTEX07	0.1118	0.0891	1.898	0.894
AMTEX08	0.1290	0.0719	0.937	0.326
ELDOME	0.0896	0.06055	1.597	0.356

TABLE 4. Fluxes, variances of the fluxes and flux integral scales of θ.

Figure 2 shows an example of the analysis procedure. The time series are divided into sub-series of length T from which the moments $\mu_2(T)$, $\mu_3(T)$ and $\mu_4(T)$ are calculated. Even though T is of the order of 25 time scales, the means (indicated by broad horizontal lines) are not equal to the mean of the entire time series shown by the thin horizontal line. This has the consequence that second- and higher order moments are slightly underestimated as predicted in Section 2.

Assuming the entire time series to be stationary, the averages of the estimates of the

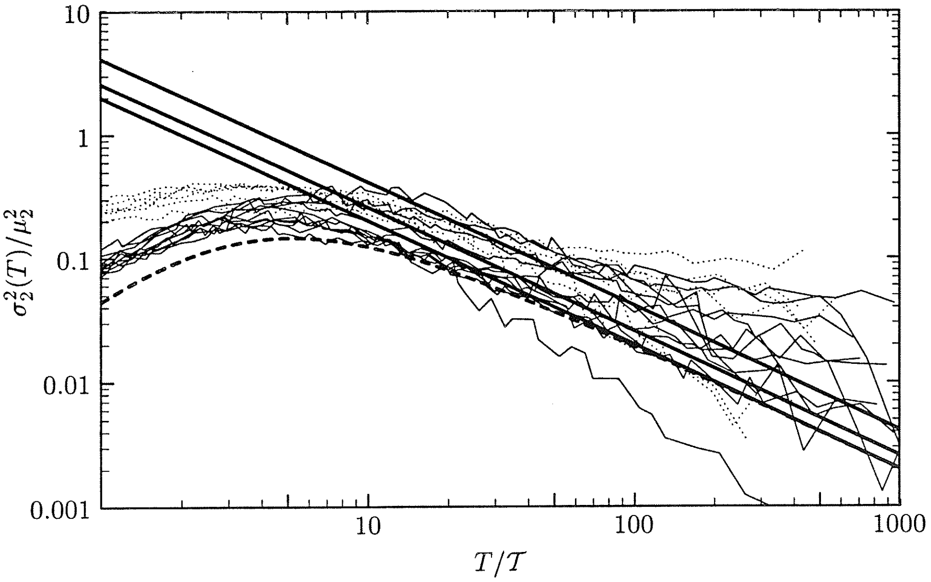

FIGURE 6. Normalized random error variance of the second-order moment of vertical velocity (solid lines) and temperature (dotted lines) versus observation time T divided by the timescale $\mathcal{T}$ or $\mathcal{T}_s$ (see Table 2 and 4). The three straight lines are the asymptotic expression from Table 6 for $a = 0$, $a = 0.1$ and $a = 0.2$ with $a = 0$ as the lower and $a = 0.2$ as the upper line. The dashed line is the exact expression for the error variance for the Gaussian process (A5).

---

moments represent $\langle\mu_n(T)\rangle$, which are shown in Figs. 3, 4 and 5 as functions of $T/\mathcal{T}$. The means of the moments estimated from a time series of length T are normalized by μ_n determined from the entire time series in order to compare with the theoretical expressions. For the second moment we compare to the exact expression, (A1), which is valid both for a Gaussian and the skewed process (2.19) provided that the auto-correlation is exponential. The experimental systematic errors of the third moment are compared to (A3), which is derived from the very skewed process ($a \to \infty$ in (2.19)), and errors of the fourth moment are compared to (A2), derived from the Gaussian process. The systematic error of the second moment is well predicted. The estimates of the systematic error of the third moment have more scatter and the error of the fourth moment is generally less than predicted. The error of the temperature moments tends to be smaller than for the vertical velocity moments, which might be due to the filtering. The asymptotic expressions differ significantly from the exact ones only at very small averaging times.

The variances of the estimates of the nth moment normalized by μ_2^n versus averaging time divided by the time scale are shown in Figs. 6, 7 and 8. Generally, the error variance estimates for a Gaussian process in section 3 are lower limits for the error variance of the moment estimates for the atmospheric signals. The estimates are improved when we use the results from the skewed process (2.19) from Table 6. This can be seen most clearly in Fig. 7 where the temperature, which generally has larger skewness than the velocity signal, has larger error variance. From Tables 2 and 3, and Fig. 1 it can be seen that $a \approx 0.2$ for the temperature signals and that a is between zero and 0.1 for the velocity. The velocity signal from AMTEX03 has an exceptionally large skewness and kurtosis and

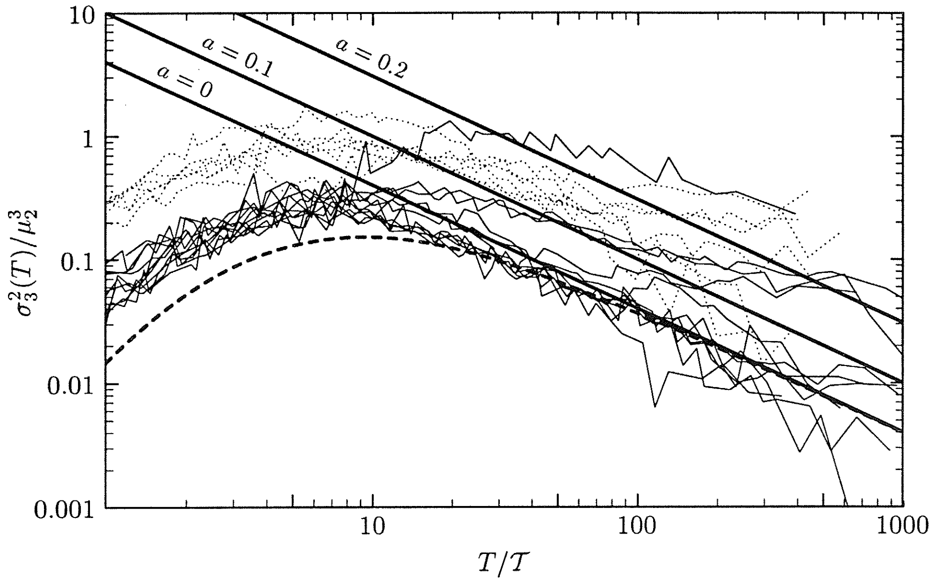

FIGURE 7. Normalized error variance of the third-order moment. See caption of Fig. 6 and Table 6. The dashed line is the exact expression for the Gaussian process, (A6).

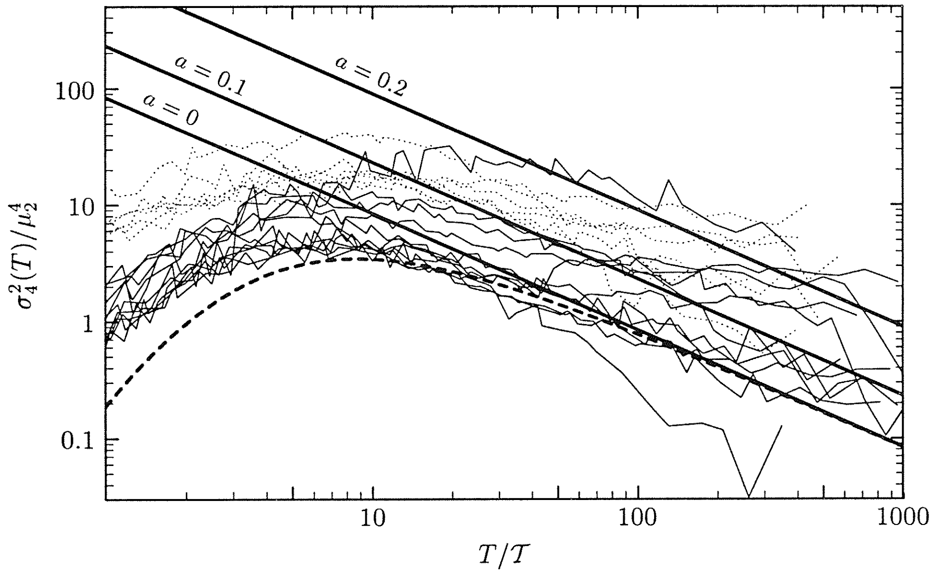

FIGURE 8. Normalized error variance of the fourth-order moment. See caption of Fig. 6 and Table 6. The dashed line is the exact expression for the Gaussian process (A7).

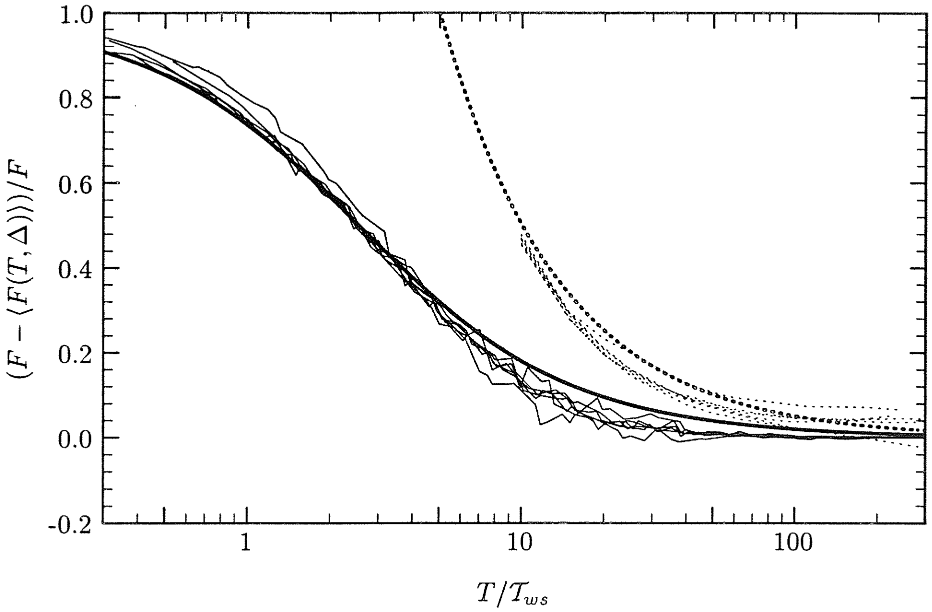

FIGURE 9. Systematic error of continuously sampled fluxes (thin solid lines) and disjunctly sampled fluxes (thin dotted lines) with $\Delta/\mathcal{T}_{ws} = 5$. The lower broad curve is (2.30) while the upper dotted broad curve is (4.6).

therefore has large error variances (see the uppermost thin solid lines in Figs. 7 and 8). The spread of the curves in Fig. 6 for $T/\mathcal{T} \approx 1000$ is partly due to poor statistics. Only three estimates of μ_n were made here for each half hour time series giving an uncertain determination of $\sigma_n^2(T)$. We do not know why the error variance of one run, AMTEX07, drops significantly below the Gaussian estimate for both $n = 2$ and $n = 4$.

To test the theory of random and systematic errors of flux measurements both the scalar (temperature) and the vertical velocity signal were subdivided into shorter pieces of length T as shown in Fig. 2. The averages w_T and s_T were subtracted and the flux was estimated according to (2.23). For the disjunctly sampled flux (4.4) was used to estimate the flux, and in order to use all the information in the data and not only data points separated by Δ, we permitted the intervals of length T, used to estimate of $F(T, \Delta)$, to be overlapping. This improved the statistics of the estimates of $\langle F(T, \Delta)\rangle$ and $\sigma_F^2(T, \Delta)$.

As seen from Fig. 9 the theory predicts the systematic errors of the flux estimates well. For the random error variance, however, there is a large spread around the theory as shown in Figs. 10 and 11. Among the reasons for this spread are poor statistics for large T and nonstationarities in the product time series $s(t)w(t)$, which were not obvious from a visual inspection of the time series. We conclude that (3.16) is slightly superior to (3.19) as an estimate of the error variance. The data analysis shown in Fig. 12 supports the asymptotic expression (4.9) for the error variance of disjunctly sampled fluxes, although the data points are somewhat scattered.

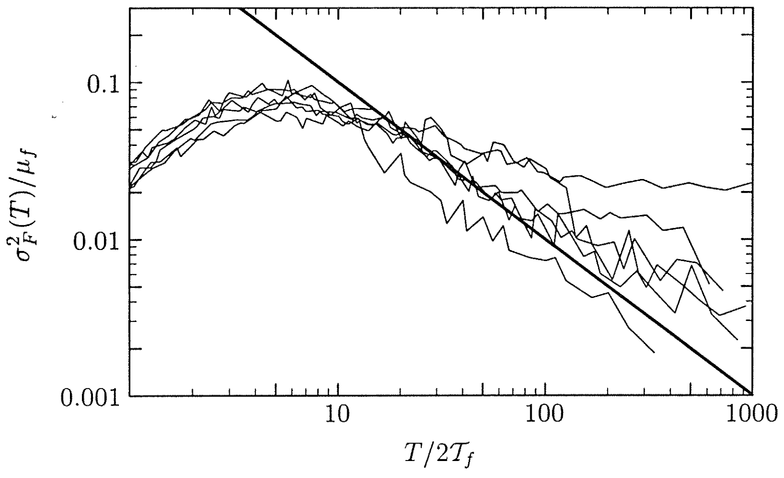

FIGURE 10. Normalized random error variance of the vertical flux of temperature. The broad line is the asymptotic expression (3.16).

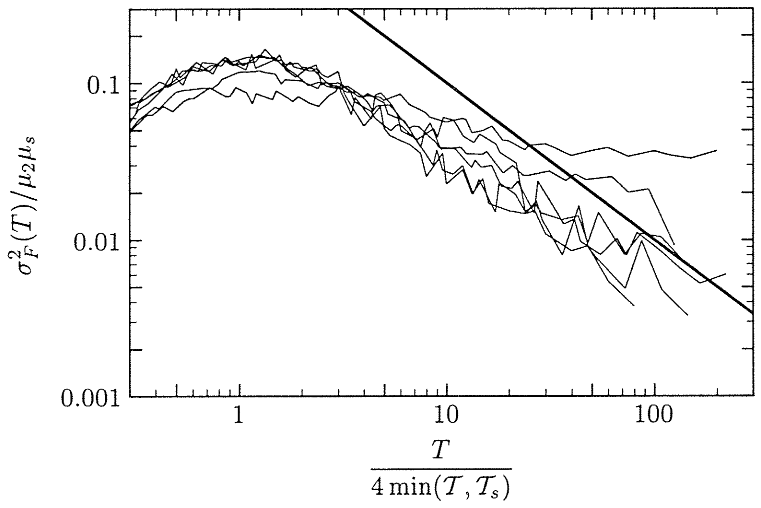

FIGURE 11. Normalized random error variance of the vertical flux of temperature. The broad line is the square of the asymptotic expression (3.19).

---

6. Discussion and Conclusions

Several previous evaluations of statistical errors of moments and fluxes have been carried out subsequent to the analysis of Lumley and Panofsky (1964). For example, Sreenivasan *et al.* (1978) investigated statistical errors of moments and fluxes using wind velocity, temperature and humidity measurements at a height of 5 m above MSL over Bass Strait off the Gippsland coast of Victoria, Australia. The conditions were slightly unstable with a Monin-Obukhov length of about −100 m. Our data are from

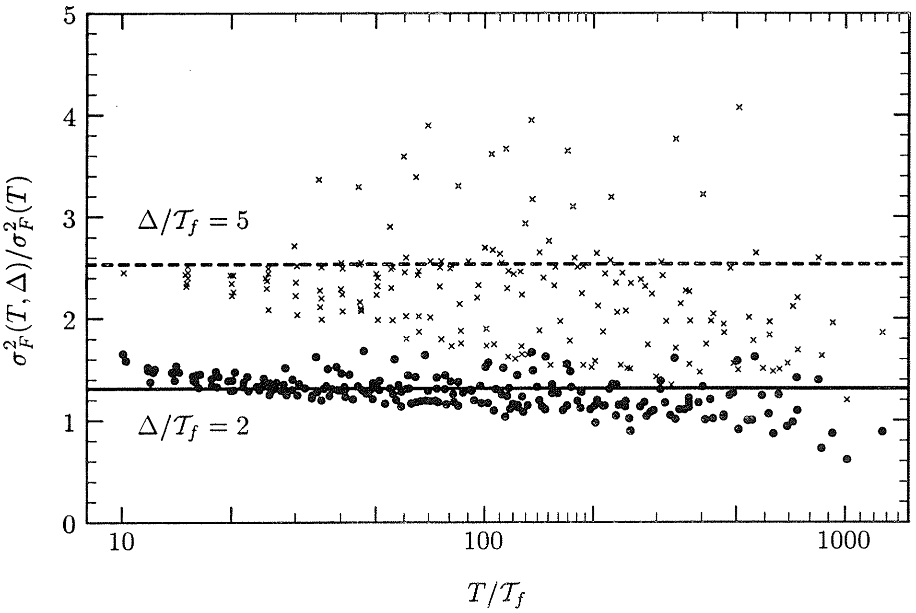

FIGURE 12. Normalized random error variance, $\sigma_F^2(T,\Delta)/\sigma_F^2(T)$, of disjunctly sampled fluxes of temperature. Dots have $\Delta/\mathcal{T}_f = 2$ while the crosses have $\Delta/\mathcal{T}_f = 5$. The horizontal lines are the asymptotic expression (4.9) valid for $N = T/\Delta \gg 1$ normalized by (3.16).

	w		θ	
	SCA	LMK	SCA	LMK
S	0.02	~0.4	0.39	~1.
K	3.16	~3.5	3.05	~4.5
$\frac{T}{\mathcal{T}}\frac{\sigma_2^2(T)}{\mu_2^2}$	2.2	2.6	2.9	4.
$\frac{T}{\mathcal{T}}\frac{\sigma_4^2(T)}{\mu_4^2}$	10.5	19.	10.9	40.

TABLE 5. Comparison between the results of Sreenivasan *et al.* (1978) (SCA) and the present analysis (LMK) for random errors of second and fourth order.

the convective boundary layer and consequently we observe somewhat higher values of skewness S and kurtosis K. In Table 5 we compare their relative error variances of second and fourth moments of w (a=0.1) and θ (a=0.2) with ours. The normalized relative error variances for Gaussian processes with exponential autocorrelation functions are 2 and $28/3 \approx 9.3$ for second- and fourth-order moments, respectively. We notice that for both orders the results of Sreenivasan *et al.* (1978) are indeed not far from the predictions for Gaussian variables, as they pointed out. However, our results show that the error variances, in particular that for the fourth-order moment, vary significantly with deviations from a Gaussian process.

In view of the general agreement between theory and experiment, we now feel confident in addressing the question of how long is "long enough" when measuring fluxes and other

	$\frac{\mu_2 - \langle\mu_2(T)\rangle}{\mu_2}\frac{T}{\mathcal{T}}$	$\frac{\mu_3 - \langle\mu_3(T)\rangle}{\mu_3}\frac{T}{\mathcal{T}}$	$\frac{\mu_4 - \langle\mu_4(T)\rangle}{\mu_4}\frac{T}{\mathcal{T}}$
$a = 0$	2	—	4
$a = 0.1$	2	5.02	4.3
$a = 0.2$	2	5.09	4.8

	$\frac{\sigma_2^2(T)}{\mu_2^2}\frac{T}{\mathcal{T}}$	$\frac{\sigma_3^2(T)}{\mu_3^2}\frac{T}{\mathcal{T}}$	$\frac{\sigma_4^2(T)}{\mu_4^2}\frac{T}{\mathcal{T}}$
$a = 0$	2	—	9.3
$a = 0.1$	2.6	29.	19.
$a = 0.2$	4.1	24.	40.

	$\frac{\sigma_2^2(T)}{\mu_2^2}\frac{T}{\mathcal{T}}$	$\frac{\sigma_3^2(T)}{\mu_2^3}\frac{T}{\mathcal{T}}$	$\frac{\sigma_4^2(T)}{\mu_2^4}\frac{T}{\mathcal{T}}$
$a = 0$	2	4	84
$a = 0.1$	2.6	9.97	231
$a = 0.2$	4.1	30.6	897

TABLE 6. Systematic and random errors of second-, third- and fourth-order moments. The Gaussian process has $a = 0$, while $a = 0.1$ and $a = 0.2$ (in (2.19)) correspond to skewnesses typical for the vertical velocities and temperatures analyzed here. The random errors are normalized in two different ways.

turbulent statistics. We first consider continuous sampling of higher moments and fluxes. Table 6 summarizes our results for both systematic and random errors of continuously sampled moments. Applying (2.28) and (3.19), and assuming on basis of the data in Tables 2 and 3 that $\mathcal{T}_s \simeq \mathcal{T}$, we arrive at the general result for the ratios of the errors

$$\frac{\sigma_n(T)}{\mu_n - \langle\mu_n(T)\rangle} \approx \frac{\sigma_F(T)}{|F - \langle F(T)\rangle|} \approx A\sqrt{\frac{T}{\mathcal{T}}}, \tag{6.1}$$

where A is a dimensionless constant of order unity for the one-variable moments. (For fluxes A is not necessarily close to unity.) Equation (6.1) and Table 6 tell us that for $T \gg \mathcal{T}$, the systematic error becomes small and the random error $\gg$ the systematic error, so that we can generally disregard the systematic error.

As an example, we estimate how long an airplane flight leg is required to estimate μ_4 with an error of 10%. Neglecting the observation that the measured kurtosis in the boundary layer is larger than for a Gaussian process, we estimate that $\sigma_4(T)/\mu_4 \simeq 0.10 \simeq 3\sqrt{\mathcal{L}/L}$, where we have now transformed from the time to the space domain, and use L as the averaging length and $\mathcal{L}$ as the integral length scale. Thus $L \simeq 900\mathcal{L}$ or, since $\mathcal{L} \sim 100$ m, $L \simeq 90$ km. With these values of L and $\mathcal{L}$ the systematic error becomes

$\sim 0.4\%$. If we assume the time series to be skewed as the temperature measurements analyzed here ($a \approx 0.2$) the flight leg would have to be $L \approx 40\mathcal{L}/(0.10)^2 \approx 400$ km.

The approach here complements that of Lenschow and Stankov (1986), who used the formulation of Lumley and Panofsky (1964) and estimated integral scales of the second moments from aircraft observations. They did not consider systematic errors nor the effects of non-Gaussianity on the errors. A situation where the systematic error becomes relevant is when trying to evaluate a scalar flux from an area of limited extent with aircraft measurements. From Lenschow and Stankov (1986) the integral length scales for w and a scalar s are $\mathcal{L} \simeq 0.24 z_i (z/z_i)^{1/2}$ and $\mathcal{L}_s \simeq 1.49 z_i (z/z_i)^{1/2}$, respectively, and the value they used for the correlation coefficient in the lower part of the mixed layer is

$$r_{ws} \equiv F_0/\sqrt{\mu_2 \mu_s} \simeq 0.56, \tag{6.2}$$

where F_0 is the surface flux. [We know of no similar general formulation in the literature for $\mathcal{L}_{ws}$, so we cannot use (2.27).] Therefore, from (2.29) the systematic error, expressed here as a function of the length L of the particular flight segment, is given by

$$\left| \frac{F - \langle F(L) \rangle}{F} \right| \leq \frac{1.2 z_i (z/z_i)^{1/2}}{|r_{ws}| L}. \tag{6.3}$$

Thus, the systematic error in the lower part of the mixed layer normalized by the surface flux is

$$\frac{|F_0 - \langle F_0(L) \rangle|}{F_0} \leq \frac{2.2 z_i (z/z_i)^{1/2}}{L}. \tag{6.4}$$

As an example, if $z_i = 1000$ m, $L = 4000$ m, and $z = 100$ m, the systematic error is $\leq 17\%$.

Using the integral length scale for the flux in the mixed layer given by Lenschow and Stankov (1986), $\mathcal{L}_f \simeq 0.16 z_i (z/z_i)^{1/3}$, in (3.18) and (6.2) we get

$$\frac{\sigma_F(L)}{|F|} = 1.16 \left(\frac{z}{z_i} \right)^{1/6} \left(\frac{z_i}{L} \right)^{1/2} \tag{6.5}$$

The result for the above example is 39%.

Substituting (6.2) and the expression for $\mathcal{L}$ into the alternative expression (3.19) we have, since $\mathcal{L} \leq \mathcal{L}_s$,

$$\frac{\sigma_F(L)}{|F|} \leq 1.75 \left(\frac{z}{z_i} \right)^{1/4} \left(\frac{z_i}{L} \right)^{1/2}. \tag{6.6}$$

The result for the above example is $\leq 49\%$.

We see that the random error is more than twice the systematic error. In order to reduce the random error to $< 10\%$, we would have to fly over the same 4 km section 16 times. This would not, of course, reduce the systematic error. If we extend the flight segment to 20 km, however, the systematic error is reduced to $\leq 4\%$, while the random error is $\simeq 18\%$. Thus, the systematic error rapidly becomes negligible while the random error may still be significant. This means that a running integral of the cospectrum from high frequency to low frequency, as utilized by e.g. Friehe *et al.* (1988), may approach a particular estimate of the flux, but that particular value will still have random scatter associated with it that will require further averaging to reduce.

In the above example, we have estimated the errors in a measured flux by normalizing by the flux at that level. This is often not as appropriate as the surface flux since the surface flux is used as a scaling parameter in both the surface layer and the mixed layer. In the lowest ~ 10% of the boundary layer the flux is often assumed to be equal to the surface flux. In other cases, it may be preferable to normalize by the flux at the measurement height, since the errors would be the relative errors at that particular level. The disadvantage of using the flux at the measurement height is that in some cases (e.g. the buoyancy flux at some level in the upper part of the mixed layer) the flux goes to zero so that the relative error becomes large for any reasonable measurement length.

In the case of stress or momentum flux measurement, Lenschow and Stankov (1986) point out that in the mixed layer generally considerably longer averaging lengths are required than for scalar fluxes to achieve the same accuracy. This follows from having a correlation coefficient that is smaller than for scalars, which more than compensates for the momentum flux having an integral scale about 75% that of scalars. Consideration of the momentum flux is somewhat more complicated than scalar fluxes since in the mixed layer the correlation coefficient depends on both z/z_i and on the ratio of the Monin-Obukhov length L_{MO} to z_i. From the results of Lenschow *et al.* (1980), we obtain for the correlation coefficient of the wind component along the direction of flow in the lower part of the mixed layer, where the momentum and temperature fluxes are assumed to have their surface values,

$$r_{wu} \simeq 0.74 \left(\frac{-L_{MO}}{z_i} \right)^{2/3} \left(\frac{z}{z_i} \right)^{-1/3} . \tag{6.7}$$

This means that in most cases $r_{wu} < 0.25$, and that typically the averaging lengths for momentum flux will be several times that for scalar fluxes for the same accuracy.

The results in this paper can also presented from the perspective of spectra and cospectra by noting that the integral time scale for an exponential autocorrelation (or correlation) function is related to the frequency of the peak in the corresponding spectrum (or cospectrum) (5.1) multiplied by frequency. The relation is $\omega_m = (\mathcal{T})^{-1}$. The corresponding relationship between the integral length scale and the wavelength of the spectral maximum is $\lambda = 2\pi\mathcal{L}$.

We have used mixed layer scaling for the examples here, but similar formulations can be obtained and applied to the surface layer. From the flux cospectrum presented by Wesely *et al.* (1989), the integral length scale for scalar fluxes in the surface layer is $\mathcal{L}_{ws}/z \simeq 1.6$, while from the spectra presented by Kaimal *et al.* (1972), $\mathcal{L}/z$ ranges from ~ 0.3 to ~ 1.0, depending on stability.

Both theory and data show that disjunct sampling of fluxes does not appreciably increase the systematic error and the error variance by much until the time between samples Δ becomes several times the appropriate integral scale. For example, (4.9) shows that for the same total averaging time T, σ_F^2 is about 8% larger than for continuous sampling when $\Delta = \mathcal{T}_f$, increasing to 31% and 250% when $\Delta/\mathcal{T}_f$ is increased to 2 and 5, respectively. The same is true for the systematic error using $\mathcal{T}_{ws}$ for the integral scale with the condition that $T \gg \mathcal{T}_{ws}$. From this point of view it seems that it is possible to use rather slow sensors with a temporal resolution of several seconds for flux measurements in the mixed layer without appreciable loss of statistical significance if the sample is grabbed quickly, as pointed out by Cooper (1993).

We acknowledge the contributions of Art Isbell, Mike Dipurna, John DeSanto, and Michelle Querijero who developed programs and carried out calculations of moments from aircraft data. Peter Kirkegaard provided helpful clarification of the use of the Isserlis relation. We also acknowledge the contributions of the NCAR Research Aviation Facility in conducting the Electra research flights and processing the aircraft data sets. Helpful comments on the manuscript were received from Tom Horst and Steve Oncley. We are particularly grateful to one of the referees for several helpful comments including suggesting the modified Gaussian process (2.19).

REFERENCES

BENDAT, J. S. AND PIERSOL, A. G. 1986 *Random Data, Analysis and Measurement Procedures*, 2. ed., John Wiley & Sons, New York, xvi+566 pp.

BETTS, A. K., DESJARDINS, R. L., MACPHERSON, J. I. AND KELLY, R. D. 1990 Boundary-layer heat and moisture budgets from FIFE. *Boundary-Layer Meteorol.*, **50**, 109–137.

COOPER, W. A. 1993 personal communication.

FRIEHE, C. A., WILLIAMS, E. R. AND GROSSMAN, R. L. 1988 An intercomparison of two aircraft gust probe systems. Symposium on Lower Tropospheric Profiling, Boulder, CO, 31 May – 3 June, American Meteorological Society, Boston, MA., 235–236F.

GROSSMAN, R. L. 1992 Sampling errors in the vertical fluxes of potential temperature and moisture measured by aircraft during FIFE. *J. Geophys. Res.*, **97**, D17, 18,439–18,443.

HAUGEN, D. A. 1978 Effects of sampling rates and averaging periods on meteorological measurements. In *Proceedings, Fourth Symposium on Meteorological Observations and Instrumentation*, April 1978, Denver, CO, American Meteorological Society, Boston, MA, 15–18.

KAIMAL, J. C. AND GAYNOR, J. E. 1983 The Boulder Atmospheric Observatory. *J. Clim. Appl. Meteor.*, **22**, 863-880.

KAIMAL, J. C., WYNGAARD, J. C., IZUMI, Y. AND COTÉ, O. R. 1972 Spectral characteristics of surface-layer turbulence *Quart. J. Roy. Meteor. Soc.*, **98**, 563–589.

KELLY, R. D., SMITH, E. A. AND MACPHERSON, J. I. 1992 A Comparison of Surface Sensible and Latent Heat Fluxes From Aircraft and Surface Measurements in FIFE 1987. *J. Geophys. Res.*, **97**, D17, 18,445–18,453.

KOOPMANS, L. H. 1974 *The Spectral Analysis of Time Series*, Academic Press, New York, xiv+368 pp.

LEMONE, M. A. 1990 Some observations of vertical-velocity skewness in the convective planetary boundary layer. *J. Atmos. Sci.*, **47**, 1163-1169.

LENSCHOW, D. H. AND AGEE, E.M. 1976 Preliminary results from the Air Mass Transformation Experiment (AMTEX). *Bull. Amer. Meteor. Soc.*, **57**, 1346–1355.

LENSCHOW, D. H., WYNGAARD, J. C. AND PENNELL, W. T. 1980 Mean-field and second-moment budgets in a baroclinic, convective boundary layer. *J. Atmos. Sci.*, **37**, 1313-1326.

LENSCHOW, D. H. AND HICKS, B. B. 1989 *Global Tropospheric Chemistry: Chemical Fluxes in the Global Atmosphere*, National Center for Atmospheric Research, Boulder, CO, 107 pp.

LENSCHOW, D. H. AND KRISTENSEN, L. 1985: Uncorrelated noise in turbulence measurements. *NCAR Tech. Note*, NCAR/TN-254, 52 pp. and *J. Atm. Ocean. Tech.*, **2**, 68-81.

LENSCHOW, D. H., MANN, J. AND KRISTENSEN, L. 1993 How long is long enough when measuring fluxes and other turbulence statistics? NCAR/TN-389+STR. Available from NCAR, P.O. Box 3000, Boulder, CO80307, 53 pp.

LENSCHOW, D. H. AND STANKOV, B. B. 1986 Length scales in the convective boundary layer. *J. Atmos. Sci.*, **43**, 1198-1209.

LUMLEY, J. L. AND PANOFSKY, H. A. 1964 *The Structure of Atmospheric Turbulence*, John Wiley & Sons, New York, 239 pp.

MASON, P. J. 1989 Large eddy simulation of the convective atmospheric boundary layer. *J. Atmos. Sci.*, **46**, 1492-1516.

MOENG, C.-H AND ROTUNNO, R. 1990 Vertical-velocity skewness in the buoyancy-driven boundary layer. *J. Atmos. Sci.*, **47**, 1149–1162.

SCHMIDT, H. AND SCHUMANN, U. 1989 Coherent structure of the convective boundary layer derived from large-eddy simulations. *J. Fluid Mech.*, **200**, 511-562.

SREENIVASAN, K. R., CHAMBERS, A. J. AND ANTONIA, R. A. 1978 Accuracy of moments of velocity and scalar fluctuations in the atmospheric surface layer. *Boundary-Layer Meteorol.*, **14**, 341-359.

WESELY, M. L., LENSCHOW D. H. AND DENMEAD, O. T. 1989 Flux measurement techniques. A chapter in *Global Tropospheric Chemistry: Chemical Fluxes in the Global Atmosphere*, edited by D.H. Lenschow and B.B. Hicks, published by NCAR, P.O. Box 3000, Boulder, CO 80307, 31–46.

WOLFRAM, S. 1991 *Mathematica:* A System for Doing Mathematics by Computer, 2. ed., Addison-Wesely Publishing Company, Inc., 749 pp.

WYNGAARD, J. C. 1973 On surface-layer turbulence. A chapter in *Workshop on Micrometeorology,* edited by D.A. Haugen, American Meteorological Society, Boston, MA, 101–149.

Appendix A. Exact 2nd-, 3rd- and 4th-Order Moments

We have obtained exact formulations of systematic as well as random errors up to fourth order, assuming an exponential autocorrelation function. As it is a trivial, but extremely cumbersome task to evaluate and verify all these expressions, we have employed the capabilities of *Mathematica* (Wolfram, 1991) to automate most of the symbolic mathematical operations.

The second-order systematic error (2.13) becomes

$$\frac{\langle \mu_2(T) \rangle}{\mu_2} = 1 - \frac{2}{x} + \frac{2}{x^2} - \frac{2}{e^x x^2}, \tag{A 1}$$

where $x = T/\mathcal{T}$.

For all other systematic and random errors we must assume that the process is either Gaussian or derived from a Gaussian process such that it becomes possible to break moments of higher than second order down to second-order moments using the Isserlis relations.

The fourth order systematic error for a Gaussian process is then

$$\frac{\langle \mu_4(T) \rangle}{\mu_4} = 1 - \frac{4}{x} + \frac{8}{x^2} - \frac{4}{x^3} - \frac{12}{x^4} + \frac{4}{e^x x^2} + \frac{8}{e^x x^3} + \frac{24}{e^x x^4} - \frac{4}{e^{2x} x^3} - \frac{12}{e^{2x} x^4}. \tag{A 2}$$

When the process $w(t)$ is not Gaussian, but given by (2.19) in the extremely skewed limit of $a \to \infty$, i.e. $w(t) \propto z^2(t) - \sigma_0^2$, where $z(t)$ is Gaussian and has a zero ensemble mean and variance σ_0, the systematic errors are

$$\frac{\langle \tilde{\mu}_3(T) \rangle}{\tilde{\mu}_3} = 1 - \frac{6}{x} + \frac{18}{x^2} - \frac{24}{x^3} + \frac{6}{e^x x^2} + \frac{24}{e^x x^3} \tag{A 3}$$

and

$$\frac{\langle \tilde{\mu}_4(T) \rangle}{\tilde{\mu}_4} = 1 - \frac{36}{5x} + \frac{168}{5x^2} - \frac{492}{5x^3} + \frac{684}{5x^4} - \frac{12}{5e^x x^2} - \frac{216}{5e^x x^3} - \frac{648}{5e^x x^4} - \frac{12}{5e^{2x} x^3} - \frac{36}{5e^{2x} x^4}, \tag{A 4}$$

where a tilde denotes moments for the skewed process.

For a Gaussian process the error variances are

$$\frac{\sigma_2^2(T)}{\mu_2^2} = \frac{2}{x} - \frac{9}{x^2} + \frac{12}{x^3} + \frac{8}{x^4} - \frac{8}{e^x x^2} - \frac{16}{e^x x^3} - \frac{16}{e^x x^4} + \frac{1}{e^{2x} x^2} + \frac{4}{e^{2x} x^3} + \frac{8}{e^{2x} x^4}, \tag{A 5}$$

$$\begin{aligned} \frac{\sigma_3^2(T)}{\mu_2^3} = {} & \frac{4}{x} - \frac{112}{3x^2} + \frac{138}{x^3} - \frac{70}{x^4} - \frac{576}{x^5} - \frac{480}{x^6} \\ & + \frac{72}{e^x x^2} + \frac{288}{e^x x^3} + \frac{666}{e^x x^4} + \frac{1440}{e^x x^5} + \frac{1440}{e^x x^6} \\ & - \frac{126}{e^{2x} x^3} - \frac{666}{e^{2x} x^4} - \frac{1152}{e^{2x} x^5} - \frac{1440}{e^{2x} x^6} \\ & + \frac{4}{3e^{3x} x^2} + \frac{12}{e^{3x} x^3} + \frac{70}{e^{3x} x^4} + \frac{288}{e^{3x} x^5} + \frac{480}{e^{3x} x^6} \end{aligned} \tag{A 6}$$

and

$$\begin{aligned} \frac{\sigma_4^2(T)}{\mu_2^4} = {} & \frac{84}{x} - \frac{743}{x^2} + \frac{8768}{3x^3} - \frac{12472}{3x^4} - \frac{7176}{x^5} + \frac{16032}{x^6} + \frac{29376}{x^7} + \frac{13824}{x^8} \\ & + \frac{288}{e^x x^2} + \frac{1344}{e^x x^3} - \frac{26864}{3e^x x^4} - \frac{6048}{e^x x^5} - \frac{52320}{e^x x^6} - \frac{100224}{e^x x^7} - \frac{55296}{e^x x^8} \end{aligned}$$

$$
\begin{aligned}
&+\frac{36}{e^{2x}x^2}-\frac{1152}{e^{2x}x^3}-\frac{1152}{e^{2x}x^4}+\frac{17280}{e^{2x}x^5}+\frac{61344}{e^{2x}x^6}+\frac{124416}{e^{2x}x^7}+\frac{82944}{e^{2x}x^8}\\
&\qquad+\frac{352}{3e^{3x}x^3}-\frac{272}{3e^{3x}x^4}-\frac{5280}{e^{3x}x^5}-\frac{29856}{e^{3x}x^6}-\frac{65664}{e^{3x}x^7}-\frac{55296}{e^{3x}x^8}\\
&+\frac{3}{e^{4x}x^2}+\frac{32}{e^{4x}x^3}+\frac{728}{3e^{4x}x^4}+\frac{1224}{e^{4x}x^5}+\frac{4800}{e^{4x}x^6}+\frac{12096}{e^{4x}x^7}+\frac{13824}{e^{4x}x^8}.
\end{aligned}
\tag{A 7}
$$

Assuming the special non-Gaussian process $w(t) \propto z^2(t) - \sigma_0^2$ we get for the error variance of $\tilde{\mu}_2(T)$

$$
\begin{aligned}
\frac{\tilde{\sigma}_2^2(T)}{\tilde{\mu}_2^2} = {} & \frac{22}{x}-\frac{155}{x^2}+\frac{500}{x^3}-\frac{688}{x^4}\\
&-\frac{8}{e^x\,x^2}+\frac{208}{e^x\,x^3}+\frac{656}{e^x\,x^4}\\
&+\frac{3}{e^{2\,x}\,x^2}+\frac{12}{e^{2\,x}\,x^3}+\frac{32}{e^{2\,x}\,x^4}.
\end{aligned}
\tag{A 8}
$$

In this case the third- and fourth-order error variances turned out to be too complicated to evaluate.

Appendix B. Asymptotic Results for Higher Order Moments

In §B.1 we derive asymptotic expressions valid for large $x = T/\mathcal{T}$ for the systematic error and the error variance of measured moments of arbitrary order for a Gaussian process. Then, in §B.2, we derive similar expressions for a highly skewed process $w(t) \propto z^2(t) - \sigma_0^2$ or $a \to \infty$ in (2.19). Since this process has unrealistic kurtosis and skewness we also derive the systematic and random errors in §B.3 of the more realistic process (2.19), but only up to the fourth moment. Finally, in §B.4 the results are summarized in some tables.

The property that odd moments of a Gaussian process are zero while even order moments of order $2n$ can be expanded into a sum over all possible products of n covariances, will be used extensively (the Isserlis relation). The number of terms in this sum is $(2n-1)!!$. Simple combinatorial arguments are also used.

B.1. *The Gaussian Process*

In order to evaluate the ensemble average of (2.6), the estimate of the n-order moment, we expand $(w(t) - w_T)^n$ and obtain a series of n-order moments. If n is odd then the ensemble average is zero, so we assume n to be even. Without loss of generality we assume $\langle w^2(t) \rangle = 1$. The simplest term in the expansion is $\langle w^n(t) \rangle = (n-1)!!$. The next simplest is

$$\int \langle w^{n-1}(t) w(t_1) \rangle = (n-1)!! \int \rho(t - t_1) \tag{B 1}$$

The factor $(n-1)!!$ is found as follows. The pair containing $w(t_1)$ can be chosen in $n-1$ different ways. The remaining $n-2$ Gaussian variables in the ensemble mean can form pairs in $(n-3)!!$ ways. All terms in the expansion reduce to $\langle w(t) w(t_1) \rangle$ and there are in all $(n-1) \times (n-3)!! = (n-1)!!$. In the limit $T \gg \mathcal{T}$ or $x \gg 1$ the integral on the right hand side reduces to $2/x$.

To first order in $x^{-1} = \mathcal{T}/T$ we have

$$\int \langle w^{n-2}(t) w(t_1) w(t_2) \rangle = (n-3)!! \int \rho(t_1 - t_2) \overset{1.}{=} (n-3)!! 2/x \tag{B 2}$$

The first equality is exact while the second is valid to the first order in x^{-1} as indicated by the special sign $\overset{1.}{=}$. To understand this asymptotic relation note that only the $(n-3)!!$ products of the form $\langle w^2(t) \rangle^{n/2-1} \langle w(t_1) w(t_2) \rangle$ are of first order in $1/x$ when integrated, while other terms like $\int \langle w^2(t) \rangle^{n/2-2} \langle w(t) w(t_1) \rangle \langle w(t) w(t_2) \rangle$ would be of higher order in $1/x$. Finally,

$$\int \left\langle w^{n-i}(t) \prod_{\ell=1}^{i} w(t_\ell) \right\rangle \overset{1.}{=} 0, \qquad \text{for } i > 2 \tag{B 3}$$

so expanding the ensemble average of (2.6) we get

$$\begin{aligned} \langle \mu_n(T) \rangle &= \sum_{i=0}^{n} (-1)^i \binom{n}{i} \int \left\langle w^{n-i}(t) \prod_{\ell=1}^{i} w(t_\ell) \right\rangle \\ &\overset{1.}{=} (n-1)!! - n(n-1)!! 2/x + \frac{n(n-1)}{2} (n-3)!! 2/x \\ &= (n-1)!! \, (1 - n/x) \qquad (n \text{ even}) \end{aligned} \tag{B 4}$$

by inserting (B 1), (B 2) and (B 3). For the normalized systematic error of the estimated

n-order moment we therefore get

$$\frac{\langle \mu_n(T)\rangle}{\mu_n} \overset{1.}{=} 1 - \frac{n}{x}, \qquad \text{for } n \text{ even.} \tag{B 5}$$

in the limit of large T or x.

To find asymptotic expressions for the random error of the moments we proceed in almost the same way, not expanding $\langle \mu_n(T)\rangle$ but

$$\langle \mu_n^2(T)\rangle = \int \langle (w(t_a) - w_T)^n (w(t_b) - w_T)^n \rangle \tag{B 6}$$

To do this we again need to expand and estimate the leading terms of various higher order correlations. We get

$$\int \langle w^n(t_1) w^n(t_2)\rangle = {\sum_2}_{i=0}^{n} \left[(n-i-1)!! \binom{n}{i} \right]^2 i! \int \rho^i(t_2 - t_1), \tag{B 7}$$

where we have introduced the notation

$${\sum_2}_{i=k}^{n} \equiv \begin{cases} \displaystyle\sum_{i \text{ even},\ k \le i \le n} & \text{for } n \text{ even} \\ \displaystyle\sum_{i \text{ odd},\ k \le i \le n} & \text{for } n \text{ odd.} \end{cases} \tag{B 8}$$

This is true exactly, not only asymptotically, for large x. To understand (B 7) assume n is even. The number of terms which contains only variances and not covariances when we apply the Isserlis relation is found as the number of possible pairings of the n $w(t_1)$'s times the number of pairings of the $w(t_2)$'s, i.e. $((n-1)!!)^2$. This is the first term in the sum in (B 7). To find the number of terms including the factor $\rho^i(t_2 - t_1)$ we select i of the $w(t_1)$'s and i of the $w(t_2)$'s (where i has to be even) which can be done in $\binom{n}{i}^2$ ways. These terms can be grouped to $\langle w(t_1) w(t_2)\rangle^i$ in $i!$ ways. The remaining $(n-i)$ $w(t_1)$'s and $w(t_2)$'s can be paired to variances ($= 1$) in $((n-i-1)!!)^2$ ways. The product of these numbers is the coefficient of ρ^i in (B 7). The arguments are very similar for odd n.

The following relations are valid for large x:

$$\int \langle w^n(t_1) w^{n-1}(t_2) w(t_3)\rangle \overset{1.}{=} \begin{cases} ((n-1)!!)^2 \int \rho(t_2 - t_1) & n \text{ even} \\ n\,((n-2)!!)^2 \int \rho(t_2 - t_1) & n \text{ odd} \end{cases} \tag{B 9}$$

$$\int \langle w^{n-1}(t_1) w^{n-1}(t_2) w(t_3) w(t_4)\rangle \overset{1.}{=} \begin{cases} 0 & n \text{ even} \\ ((n-2)!!)^2 \int \rho(t_2 - t_1) & n \text{ odd} \end{cases} \tag{B 10}$$

$$\int \langle w^n(t_1) w^{n-2}(t_2) w(t_3) w(t_4)\rangle$$
$$\overset{1.}{=} \begin{cases} (n-1)!!(n-3)!! \int \rho(t_2 - t_1) & n \text{ even} \\ 0 & n \text{ odd.} \end{cases} \tag{B 11}$$

All other correlations needed in the expansion of the square of the nth moment†:

$$\langle \mu_n^2(T) \rangle = \sum_{i=0}^{n}\sum_{j=0}^{n}(-1)^{i+j}\binom{n}{i}\binom{n}{j}\int\left\langle w^{n-i}(t_a)w^{n-j}(t_b)\prod_{\ell=1}^{i+j}w(t_\ell)\right\rangle \tag{B 12}$$

can be shown to be of higher order in $1/x$ and are therefore dropped in the summation. We now assume that $w(t)$ has an exponential correlation function in which case $\int\rho^n(t_2-t_1)\overset{1.}{=}2/(nx)$. Substituting (B 7), (B 9), (B 10) and (B 11) into (B 12) and using the result for $\langle\mu_n(T)\rangle$, (B 4) we obtain after some rearrangement

$$\frac{\sigma_n^2(T)}{\mu_2^n} = \frac{\langle\mu_n^2(T)\rangle - \langle\mu_n(T)\rangle^2}{\mu_2^n} \overset{1.}{=} \frac{2}{x}\sum_{i=2}^{n}{}_2\left[(n-i-1)!!\binom{n}{i}\right]^2(i-1)! \tag{B 13}$$

for arbitrary values of μ_2.

B.2. *A Skewed Process*

The process $w(t)$ is here defined as the highly skewed process $z^2(t)-\langle z^2(t)\rangle$, where $z(t)$ is a Gaussian process. For simplicity we let $\langle z^2(t)\rangle = 1$, and let $\rho_0(\tau)$ denote the correlation function for $z(t)$.

The derivation is similar to the Gaussian case, but more cumbersome. In the expansion (B 12) we need to estimate expressions of the form

$$\int\left\langle z^{2k}(t_a)z^{2p}(t_b)\prod_{\ell=1}^{m}z^2(t_\ell)\right\rangle \tag{B 14}$$

for $x \gg 1$. When applying the Isserlis relation, the number of terms where $2q$ of the $z(t_a)$'s and $2q$ of the $z(t_b)$'s combine to give $\rho_0^{2q}(t_a-t_b)$ and all other z's combine to give variances (=1) is found easily: Select $2q$ of the $z(t_a)$'s and $2q$ of the $z(t_b)$'s, which can be done in $\binom{2k}{2q}\binom{2p}{2q}$ ways. These can form $\rho_0^{2q}(t_a-t_b)$ in $(2q)!$ ways. The left over z's can form variance pairs in $(2(k-q)-1)!!\,(2(p-q)-1)!!$ ways. All terms where $z(t_a)$ and $z(t_b)$ form $\rho_0(t_a-t_b)$ in various powers are thus

$$\begin{aligned} Z_1(k,p) = \sum_{q=0}^{\min(k,p)}&\binom{2k}{2q}\binom{2p}{2q}(2q)!\,(2(k-q)-1)!!\,(2(p-q)-1)!! \\ &\times\int\rho_0^{2q}(t_a-t_b). \end{aligned} \tag{B 15}$$

The expansion of (B 14) to first order in x^{-1} is

$$\begin{aligned} &\int\left\langle z^{2k}(t_a)z^{2p}(t_b)\prod_{\ell=1}^{m}z^2(t_\ell)\right\rangle \overset{1.}{=} Z_1(k,p) \\ &+2\binom{m}{2}(2k-1)!!(2p-1)!!\int\rho_0^2(t-t_1) \\ &+2mk(2k-1)!!(2p-1)!!\int\rho_0^2(t-t_1) \\ &+2mp(2k-1)!!(2p-1)!!\int\rho_0^2(t-t_1) \end{aligned}$$

---

† A product from $\ell = 1$ to 0 is just 1

$$= Z_1(k,p) + (2k-1)!!(2p-1)!!\left[m^2 + m\left(2(k+p)-1\right)\right] \int \rho_0^2(t-t_1) \qquad \text{(B 16)}$$

where the first term on the right hand side has already been discussed, the second terms arise from combinations of different $z(t_\ell)$'s to give correlations while the third and the fourth terms come from combinations of $z(t_\ell)$ with $z(t_a)$'s and $z(t_b)$'s, respectively. When $p = 1$ (B 16) simplifies to

$$\int \left\langle z^{2k}(t_a) \prod_{\ell=1}^{m} z^2(t_\ell) \right\rangle \overset{1.}{=} (2k-1)!! \left\{ 1 + \left[m^2 + m(2k-1)\right] \int \rho_0^2(t-t_1) \right\} . \qquad \text{(B 17)}$$

To evaluate the systematic error of the skewed process we need the asymptotic expression

$$\begin{aligned} &\int \left\langle w^n(t) \prod_{\ell=1}^{p} w(t_\ell) \right\rangle \\ &= \sum_{j=0}^{n} (-1)^{n-j} \binom{n}{j} \sum_{q=0}^{p} (-1)^{p-q} \binom{p}{q} \int \left\langle z^{2j}(t) \prod_{\ell=1}^{q} z^2(t_\ell) \right\rangle \\ &\overset{1.}{=} \sum_{j=0}^{n} (-1)^{n-j+p} \binom{n}{j} \sum_{q=0}^{p} (-1)^{q} \binom{p}{q} \times \\ &\qquad (2j-1)!!(2k-1)!! \left\{ 1 + \left[q^2 + q(2k-1)\right] \int \rho_0^2(t-t_1) \right\} \end{aligned} \qquad \text{(B 18)}$$

easily found from (B 17). Using the relations $\sum_{q=0}^{p}(-1)^q \binom{p}{q} = \delta_{0p}$, $\sum_{q=0}^{p}(-1)^q \binom{p}{q} q = -\delta_{1p}$ and $\sum_{q=0}^{p}(-1)^q \binom{p}{q} q^2 = -\delta_{1p} + 2\delta_{2p}$ we get to first order in x^{-1}

$$\int \left\langle w^n(t) \prod_{\ell=1}^{p} w(t_\ell) \right\rangle \overset{1.}{=} \begin{cases} \sum_{j=0}^{n} (-1)^{n-j} \binom{n}{j} (2j-1)!! & p = 0 \\ \sum_{j=0}^{n} (-1)^{n-j} \binom{n}{j} 2j(2j-1)!! \int \rho(t-t_1) & p = 1 \\ 2\sum_{j=0}^{n} (-1)^{n-j} \binom{n}{j} (2j-1)!! \int \rho(t-t_1) & p = 2 \\ 0 & \text{elsewhere} \end{cases} \qquad \text{(B 19)}$$

where we have assumed ρ_0 to be exponential so ρ_0^2 can be substituted by ρ Using the same expansion of the ensemble mean of the nth order moment as in (B 4) we get by (B 19)

$$\begin{aligned} \langle \tilde{\mu}_n(T) \rangle &\overset{1.}{=} \sum_{j=0}^{n} (-1)^{n-j} \binom{n}{j} (2j-1)!! \\ &+ \frac{2n}{x} \sum_{j=1}^{n-1} (-1)^{n-j} \binom{n-1}{j} (2j-3)!! j(4j-3). \end{aligned} \qquad \text{(B 20)}$$

For the random error we use the expansion in (B 12) and note that

$$\begin{aligned}
&\int \left\langle w^{n-i}(t_a) w^{n-j}(t_b) \prod_{\ell=1}^{i+j} w(t_\ell) \right\rangle = \\
&\sum_{k=0}^{n-i} (-1)^{n-i-k} \binom{n-i}{k} \sum_{p=0}^{n-j} (-1)^{n-j-p} \binom{n-j}{p} \sum_{m=0}^{i+j} (-1)^{i+j-m} \binom{i+j}{m} \\
&\times \int \left\langle z^{2k}(t_a) z^{2p}(t_b) \prod_{\ell=1}^{m} z^2(t_\ell) \right\rangle
\end{aligned} \tag{B 21}$$

to get

$$\begin{aligned}
\langle \tilde{\mu}_n^2(T) \rangle &\overset{1.}{=} \sum_{p=0}^{n} \sum_{k=0}^{n} (-1)^{k+p} \binom{n}{k} \binom{n}{p} Z_2(k,p) \\
&+ \frac{4n}{x} \sum_{p=0}^{n} \sum_{k=0}^{n-1} (-1)^{k+p} \binom{n-1}{k} \binom{n}{p} 2(k+p)(2k-1)!!(2p-1)!! \\
&+ \frac{4n^2}{x} \left(\sum_{k=0}^{n-1} (-1)^k \binom{n-1}{k} (2k-1)!! \right)^2 \\
&+ \frac{4n(n-1)}{x} \sum_{p=0}^{n} \sum_{k=0}^{n-2} (-1)^{k+p} \binom{n-2}{k} \binom{n}{p} (2k-1)!!(2p-1)!!
\end{aligned} \tag{B 22}$$

where

$$\begin{aligned}
Z_2(k,p) &= (2k-1)!!(2p-1)!! \\
&+ \sum_{q=1}^{\min(k,p)} \binom{2k}{2q} \binom{2p}{2q} (2q)!(2(k-q)-1)!!(2(p-q)-1)!! \frac{2}{qx}.
\end{aligned} \tag{B 23}$$

B.3. *A More Realistic Skewed Process*

As mentioned in section 2 the stochastic process (2.19) may realistically model the skewness and kurtosis for both the vertical velocity and the temperature. Without loss of generality we assume here that $\sigma_0 = 1$ so (2.19) becomes

$$w(t) = z(t) + a(z^2(t) - 1) \tag{B 24}$$

We calculate the time scale $\mathcal{T}$ of the skewed process $w(t)$ as

$$\mathcal{T} \equiv \frac{\int_0^\infty R_{ww}(\tau) d\tau}{R_{ww}(0)} = \frac{1+a^2}{1+2a^2} \mathcal{T}_0 \tag{B 25}$$

where $\mathcal{T}_0$ is the time scale for the Gaussian process $z(t)$. Expansion of the equation for the mean moments (2.6) and for the error variance of the moments (3.1) requires evaluation of integrals of the form

$$\int \left\langle \underbrace{w(t_1)w(t_1)...w(t_1)}_{n_1} \underbrace{w(t_2)...w(t_2)}_{n_2} ... \underbrace{w(t_m)...w(t_m)}_{n_m} \right\rangle . \tag{B 26}$$

It can be seen that only if the number of odd n_i's is zero or two is the integral of higher than second order in $1/x$. In the first case, i.e. when $n_1, ..., n_m$ are all even, the integral

(B 26) has a constant term

$$\prod_{i=1}^{m}(n_i-1)!! \tag{B 27}$$

and a term proportional to $1/x_0 = \mathcal{T}_0/T = \frac{1+2a^2}{1+a^2}\frac{\mathcal{T}}{T} = \frac{1+2a^2}{1+a^2}1/x$:

$$\sum_{i=1}^{m-1}\sum_{j=i+1}^{m}\prod_{\substack{k=1\\k\neq i,j}}^{m}(n_k-1)!!\sum_{\substack{l=2\\\text{step2}}}^{\min(n_i,n_j)}\frac{2}{lx_0}l!\binom{n_i}{l}\binom{n_j}{l}(n_i-l-1)!!(n_j-l-1)!!. \tag{B 28}$$

In the second case, i.e. when $n_1,\dots,n_{m-2}$ are even and n_{m-1} and n_m are odd, there is no constant term and the term proportional to $1/x_0$ is

$$\prod_{k=1}^{m-2}(n_k-1)!!\sum_{\substack{l=1\\\text{step2}}}^{\min(n_{m-1},n_m)}\frac{2}{lx_0}l!\binom{n_{m-1}}{l}\binom{n_m}{l}(n_{m-1}-l-1)!!(n_m-l-1)!!. \tag{B 29}$$

These equations are obtained by using the Isserlis relation and combinatorial arguments. Expanding (2.6) and (3.1) with the aid of *Mathematica* (Wolfram, 1991) and applying (B 27), (B 28) and (B 29) we get for the first few moments of the skewed process (B 24):

$$\langle\tilde\mu_2(T)\rangle = 1+2a^2-\frac{2}{x_0}(1+a^2), \tag{B 30}$$

$$\langle\tilde\mu_3(T)\rangle = 2a(3+4a^2)-\frac{6a}{x_0}\left(5+4a^2\right) \tag{B 31}$$

and

$$\langle\tilde\mu_4(T)\rangle = 3(1+20a^2+20a^4)-\frac{12}{x_0}\left(1+27a^2+18a^4\right). \tag{B 32}$$

Error variances of the these moments are

$$\tilde\sigma_2^2(T) = \frac{2}{x_0}\left(1+32a^2+22a^4\right), \tag{B 33}$$

$$\tilde\sigma_3^2(T) = \frac{4}{x_0}\left(1+147a^2+1476a^4+780a^6\right) \tag{B 34}$$

and

$$\tilde\sigma_4^2(T) = \frac{84}{x_0}\left(1+\frac{1108}{7}a^2+\frac{24708}{7}a^4+15600a^6+\frac{46296}{7}a^8\right). \tag{B 35}$$

As functions of x the normalized moments thus become:

$$\langle\tilde\mu_2(T)\rangle/\tilde\mu_2 = 1-\frac{2}{x}, \tag{B 36}$$

$$\langle\tilde\mu_3(T)\rangle/\tilde\mu_3 = 1-3\left(2-\frac{1}{(1+a^2)(3+4a^2)}\right)\frac{1}{x} \tag{B 37}$$

and

$$\langle\tilde\mu_4(T)\rangle/\tilde\mu_4 = 1-\frac{4(1+2a^2)(1+27a^2+18a^4)}{(1+a^2)(1+20a^2+20a^4)}\frac{1}{x}. \tag{B 38}$$

Expressions for the error variances normalized by either $\tilde\mu_2^n$ or $\tilde\mu_n^2$ may also easily be derived. Here we give only the general, a-dependent error variances normalized by $\tilde\mu_n^2$. Examples for $a = 0.1$ and $a = 0.2$ for both normalizations are shown in the tabular

	$(\tilde{\mu}_n - \langle\tilde{\mu}_n(T)\rangle)/\tilde{\mu}_n$			
n	Gaussian	more skewed		
	$a = 0$	$a = 0.1$	$a = 0.2$	$a = \infty$
2	$2/x$	$2/x$	$2/x$	$2/x$
3	—	$5.02/x$	$5.09/x$	$6/x$
4	$4/x$	$4.27/x$	$4.78/x$	$36/(5x)$
5	—	?	?	$160/(17x)$

TABLE 7. Systematic errors as functions of $x = T/\mathcal{T}$.

	$\tilde{\sigma}_n^2(T)/\tilde{\mu}_2^n$			
n	Gaussian	more skewed		
	$a = 0$	$a = 0.1$	$a = 0.2$	$a = \infty$
2	$2/x$	$2.57/x$	$4.12/x$	$22/x$
3	$4/x$	$9.97/x$	$30.6/x$	$780/x$
4	$84/x$	$231/x$	$897/x$	$69444/x$
5	$448/x$	?	?	$9491360/x$

TABLE 8. Random errors normalized by $\tilde{\mu}_2^n$ as functions of $x = T/\mathcal{T}$.

summary B.4 and in section 6. The error variances as functions of x and not x_0 as in (B 33) – (B 35) become:

$$\tilde{\sigma}_2^2(T)/\tilde{\mu}_2^2 = \frac{2(1 + 32a^2 + 22a^4)}{(1 + a^2)(1 + 2a^2)}\frac{1}{x}, \tag{B 39}$$

$$\tilde{\sigma}_3^2(T)/\tilde{\mu}_3^2 = \frac{(1 + 2a^2)(1 + 147a^2 + 1476a^4 + 780a^6)}{a^2(1 + a^2)(3 + 4a^2)^2}\frac{1}{x}, \tag{B 40}$$

and

$$\tilde{\sigma}_4^2(T)/\tilde{\mu}_4^2 = \frac{(1 + 2a^2)(7 + 1108a^2 + 24708a^4 + 109200a^6 + 46296a^8)}{3(1 + 20a^2 + 20a^4)^2(1 + a^2)}\frac{1}{x}. \tag{B 41}$$

It can be shown that in the limit $a \to \infty$ the results in this section agree with the expressions derived in section B.2.

B.4. *Tabular summary*

Table 7 contains some of the lowest order normalized systematic errors given by (B 5)†, (B 20) and (B 36) – (B 38). Question marks indicate that the term has not been evaluated.

We see that the introduction of non-zero skewness does not significantly alter the systematic errors.

Using the equations in sections B.1, B.2 and B.3 we have tabulated error variances of some of the lowest order moments in Table 8.

Normalized in this way the parameter a drastically alters the error variance.

---

† Both the odd moments and the systematic error of odd moments of the Gaussian process are zero.

	$\sigma^2(S(T))$	$\sigma^2(K(T))$	S^2	K^2
$a = 0$	$4/x$	$12/x$	0	9
$a = 0.1$	$5.6/x$	$68./x$	0.35	12
$a = 0.2$	$10.5/x$	$333./x$	1.3	22

TABLE 9. Random errors of skewness and kurtosis as functions of $x = T/\mathcal{T}$.

Appendix C. Random Errors of Skewness and Kurtosis

'How Long is Long Enough' evaluates only the random and systematic errors of the moments, not of the skewness and the kurtosis. These errors will not be calculated in the same rigorous fashion as the errors of the moments, only asymptotically ($T \gg \mathcal{T}$). We have evaluated the systematic errors asymptotically. However, only at relatively small values of $T/\mathcal{T}$, where the asymptotic approximation is poor, we find significant systematic errors of the skewness and kurtosis. We therefore concentrate exclusively on the random errors.

C.1. *Estimation of errors*

We shall use considerations of propagation of variances to estimate the random error of the skewness and kurtosis. In general, if $Z = X^A/Y^B$ then the variance of Z can be expressed approximately in terms of the variances of X and Y and the co-variance between X and Y, $\mathrm{Cov}(X,Y)$:

$$\frac{\sigma^2(Z)}{\langle Z\rangle^2} \approx a^2\frac{\sigma_X^2}{\langle X\rangle^2} - 2ab\frac{\mathrm{Cov}(X,Y)}{\langle X\rangle\langle Y\rangle} + b^2\frac{\sigma_Y^2}{\langle Y\rangle^2} \tag{C 1}$$

Since the skewness calculated from a time series of length T is defined as $S(T) \equiv \mu_3(T)/\mu_2(T)^{3/2}$ the variance of the skewness measurement can be estimated as

$$\frac{\sigma^2(S(T))}{S^2} \approx \frac{\sigma_3^2(T)}{\mu_3^2} - 3\frac{\mathrm{Cov}(\mu_3(T),\mu_2(T))}{\mu_3\mu_2} + \frac{9}{4}\frac{\sigma_2^2(T)}{\mu_2^2} \tag{C 2}$$

(Since we are only interested in the asymptotic behaviour it is permissible to substitute $\langle\mu_3(T)\rangle$ with μ_3, etc.) For $T \gg \mathcal{T}$ this expression can be evaluated along the lines described in LMK, i.e. by assuming the process to be Gaussian with an approximately exponential auto-correlation function (or the non-Gaussian process (2.19)), then applying the Isserlis relation and using the asymptotic expressions for (B 26) in appendix B.3. The result for a Gaussian process ($a = 0$) is

$$\sigma^2(S(T)) \approx \frac{4}{x}, \tag{C 3}$$

where $x = T/\mathcal{T}$, and

$$\sigma^2(S(T)) \approx \frac{2\left(2 + 95a^2 + 908a^4 + 2670a^6 + 3792a^8 + 1344a^{10}\right)}{(1+a^2)\,(1+2\,a^2)^4 x} \tag{C 4}$$

for the more general skewed process (2.19).

For the random error of kurtosis there are two possibilities of using (C 1). The first has $A = B = 1$, $X = \mu_4(T)$ and $Y = \mu_2^2(T)$, and the second has $A = 1$, $B = 2$, $X = \mu_4(T)$

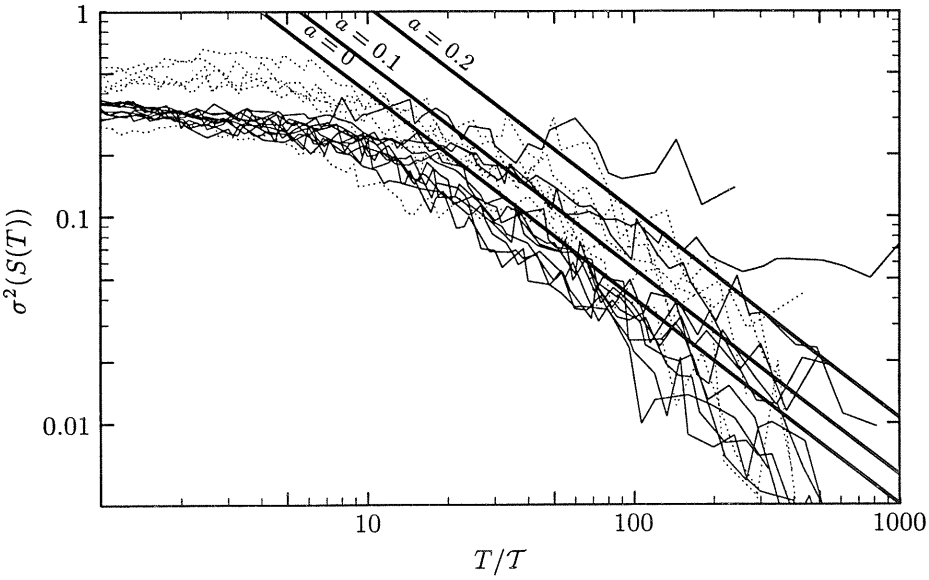

FIGURE 13. Random error variance of the skewness of vertical velocity (solid lines) and temperature (dotted lines) versus observation time T divided by the timescale $\mathcal{T}$ or $\mathcal{T}_s$ (see Table 2 and 3). The three straight lines are the asymptotic expressions from Table 9.

---

and $Y = \mu_2(T)$. In both cases we get after a series of lengthy manipulations

$$\sigma^2(K(T)) \approx \frac{12}{x} \tag{C 5}$$

for the Gaussian process and

$$\sigma^2(K(T)) \approx \frac{12}{x} \times \frac{1 + 404a^2 + 11828a^4 + 88768a^6 + 240264a^8 + 285984a^{10} + 86304a^{12}}{(1+a^2)\,(1+2\,a^2)^5} \tag{C 6}$$

for the skewed.

In Table 9 we have evaluated the random error ((C 4) and (C 6)) for typical values of a. The relative error variance of the kurtosis $\sigma^2(K(T))/K^2 \approx \frac{4}{3}\frac{1}{x}$ (Gaussian case) is much smaller than the relative variance of the fourth order moment $\sigma_4^2(T)/\mu_4^2 = \frac{28}{3}\frac{1}{x}$ (see Table 6).

C.2. *Experimental validation*

The analysis of the AMTEX and ELDOME data is completely parallel to the analysis in section 5. The general agreement with the theoretical predictions is again good except that the theory seems to overestimate the error variance of the skewness for the velocity signals which have small skewnesses. The error variance of the velocity signal AMTEX03 is the uppermost thin solid curves in Figs. 13 and 14. This signal has an exceptional large skewness and kurtosis (see Table 2 and Figure 1) which supports our conjecture that the error variance increases rapidly with skewness and kurtosis. This is also substantiated by the fact that the error variances of the temperature signals are generally larger those

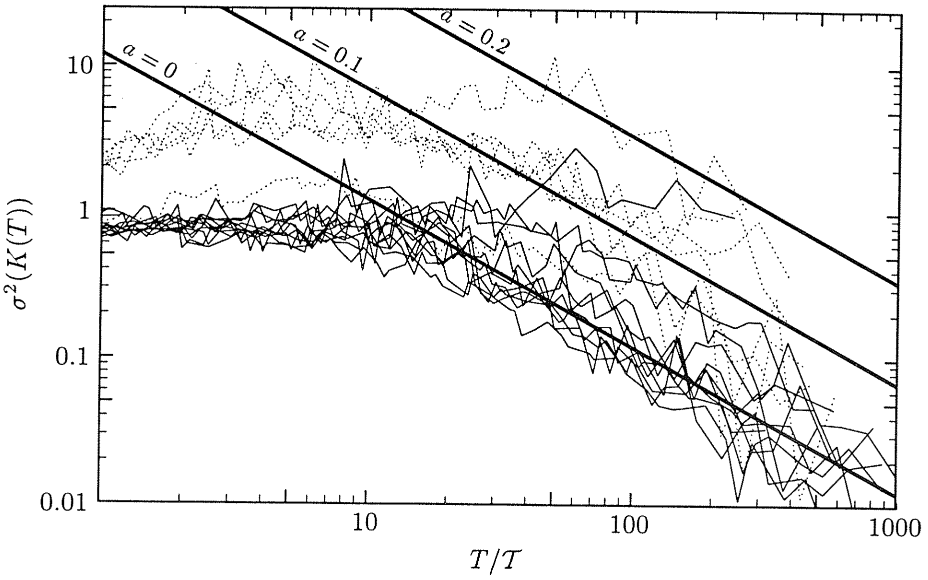

FIGURE 14. Random error variance of the kurtosis of vertical velocity and temperature. See caption of figure 13.

---

of the velocity signals. The uppermost dotted curve in Fig. 14 is the temperature signal with the largest skewness and kurtosis (AMTEX07).

PART IIB:

Errors in Airborne Flux Measurements

By JAKOB MANN† AND DONALD H. LENSCHOW

National Center for Atmospheric Research‡, Boulder, Colorado 80307, USA

(Accepted for publication in *Journal of Geophysical Research*)

We present a general approach for estimating systematic and random errors in eddy-correlation fluxes and flux gradients measured by aircraft in the convective boundary layer as a function of the length of the flight leg, or of the cut-off wavelength of a high-pass filter. The estimates are obtained from empirical expressions for various length scales in the convective boundary layer and they are experimentally verified using data from FIFE, AMTEX and ELDOME. We show that the systematic flux and flux gradient errors can be important if fluxes are calculated from a set of several short flight legs or if the vertical velocity and scalar time series are high-pass filtered. While the systematic error of the flux is usually negative, that of the flux gradient can change sign. For example, for temperature flux divergence the systematic error changes from negative to positive about a quarter of the way up in the convective boundary layer.

1. Introduction

Analysis of aircraft eddy-correlation flux measurements from the First ISLSCP (International Satellite Land Surface Climatology Project) Field Experiment (FIFE) has indicated that significant systematic errors can be introduced by high-pass filtering the vertical velocity w and scalar s time series used in calculating the eddy correlation fluxes, and possibly by inadequate length of the flight legs (Betts *et al.* 1990; Kelly *et al.* 1992; Grossman 1992a, b). Not only is the flux itself affected, but also the vertical divergence of the flux, which is a term in the budget equation for s. Although this issue is of immediate relevance to the FIFE results, as presented in the special issue of *J. Geophys. Res*, **97**, No. D17, it is of critical importance for any field program involving aircraft flux measurements. Therefore, we present here a general approach for consideration of systematic errors in fluxes measured in the convective boundary layer (CBL) as a function of the length of the flight leg, or of the cut-off wavelength of a high-pass filter. One measure of the importance of the systematic error is to compare it with the random error, which we also estimate.

We build on the results of Lenschow & Stankov (1986) and of Lenschow, Mann & Kristensen (1993) to predict the systematic and random errors. The vertical flux of a scalar is equal to the integral of the cospectrum of the vertical velocity and the scalar. When fluxes are calculated from flights of relatively short lengths or if the data signals

---

† Permanent affiliation: Risø National Laboratory, Roskilde, Denmark

‡ The National Center for Atmospheric Research is sponsored by the National Science Foundation.

are high-pass filtered, the low wavenumber contribution to the flux is neglected. The magnitude of this *systematic error* depends on the exact shape of the cospectrum at low wavenumbers, which is related to the integral length scale of the cospectrum. Because the cospectrum typically has the same sign at all wavenumbers, the systematic error will usually reduce the absolute value of the flux. For the random error the relevant length scale is the integral length scale of the flux itself. Errors in estimating flux gradients are dependent on the vertical variation of these length scales.

To test our error estimates we use convective boundary layer (CBL) data from the Air Mass Transformation Experiment (AMTEX) and the ELectra raDOMe Experiment (ELDOME) (Lenschow *et al.* 1993), as well as from FIFE (Kelly *et al.* 1992). AMTEX data were obtained over the ocean, while ELDOME and FIFE were from the continental boundary layer.

These results are, of course also applicable to tower-based eddy-correlation flux measurements. In that case, the sample length is obtained from the product of the sample time and the mean wind, instead of the aircraft true airspeed, and surface layer scaling for the integral length scales (e.g. Lenschow, 1993) is more relevant.

2. Flux errors

We consider a vertical flux of s, $F = \langle ws \rangle$ and assume, without loss of generality, that both s and w have zero mean ($\langle s \rangle = \langle w \rangle = 0$, where $\langle\ \rangle$ denotes an ensemble average). We use the symbol f for the series $f(x) = w(x)s(x) - F$, i.e. departures from the mean flux. The variance of a variable y is denoted by σ_y^2. We first consider systematic flux errors resulting from either the limited length or high-pass filtering of a flight leg. We next consider the random error resulting from the lack of a truly ensemble estimate of the flux.

2.1. *Systematic flux errors*

Lenschow *et al.* (1993) show that the systematic error in the flux is given by

$$F - \langle F(L) \rangle \approx \frac{2F\mathcal{L}_{ws}}{L}, \tag{2.1}$$

where L is the length of the flight leg and $\mathcal{L}_{ws}$ is an Eulerian integral length scale which in principle can be determined from the cospectrum† $C_{ws}(k)$ of w and s in the limit as the wave number $k \to 0$:

$$\mathcal{L}_{ws} = \frac{\pi C_{ws}(0)}{F}. \tag{2.2}$$

Similarly, the integral length scales for w and s are given by

$$\mathcal{L}_w = \frac{\pi \Phi_{ww}(0)}{\sigma_w^2} \tag{2.3}$$

and

$$\mathcal{L}_s = \frac{\pi \Phi_{ss}(0)}{\sigma_s^2}, \tag{2.4}$$

where $\Phi_{yy}(k)$ is the (double sided) power spectrum of y. The height dependence in the CBL of $\mathcal{L}_w$ and $\mathcal{L}_s$ (for temperature, humidity and ozone) was estimated by Lenschow

---

† The spectra are considered double sided, i.e. the integral from minus infinity to infinity equals the covariance.

and Stankov (1986) as

$$\mathcal{L}_w = 0.24 z_i z_*^{1/2} \tag{2.5}$$

and

$$\mathcal{L}_s = 1.49 z_i z_*^{1/2}, \tag{2.6}$$

where $z_* \equiv z/z_i$ and z_i is the height of the CBL.

Another aspect to consider is the different integral length scales generated by a scalar flux at the surface (bottom-up transport) compared to that resulting from a scalar flux at the top of the boundary layer (top-down transport). Moeng and Wyngaard (1989) used large-eddy numerical simulations of the convective boundary layer to estimate the scalar dissipation time scales of these two processes. If we assume spectral similarity between the top-down and bottom-up processes (that is, that the *shapes* of the spectra are the same, but that their amplitude and the location of the spectral maximum may be different), their results predict that the ratio of the integral scales of the top-down to bottom-up increases from about unity at $z/z_i = 0.8$ to about 5 at $z/z_i = 0.2$. They also predict that, for the same flux at the bottom as at the top, the ratio of top-down to bottom-up variance decreases from about 28 at $z/z_i = 0.8$ to about unity at $z/z_i = 0.2$. Thus, we would expect to see larger integral scales for scalars with significant top-down fluxes than for those with relatively small top-down fluxes.

Unfortunately, for temperature the ratio of the top-down to the bottom-up flux is nearly constant and the few humidity flux profiles that have different ratios have very large scatter, so we are unable to test the predictions of Moeng and Wyngaard. In the case of ozone flux over the ocean presented by Lenschow and Stankov (1986), where the surface flux is negligible compared to the top-down flux, they found no significant difference between the ozone, and the temperature and humidity integral scales. This is an issue that need to be investigated further by comparing scalars such as ozone over the ocean which has negligible surface flux with others such as temperature and humidity which normally have larger surface fluxes than top-down fluxes.

We do not know of estimates of $\mathcal{L}_{ws}$ in the literature. This is not surprising because $\Phi_{ws}(k)$ can be difficult to estimate since it can, for example, change sign, especially at low wave numbers where the coherence typically becomes small. Furthermore, in some situations, such as when the sign of the flux at the surface is different from that at the top of the CBL (as is normally the case with temperature flux) the flux must go through zero at some level within the CBL. At this point, the positive area in one region of the cospectrum must be balanced by a negative area in another region. Because of this, (2.2) is not a very 'robust' definition of a length scale. We therefore derive a relation for estimating $\mathcal{L}_{ws}$ from other more robust empirical relations.

In general,

$$|\Phi_{ws}(k)|^2 \leq \Phi_{ww}(k)\Phi_{ss}(k), \tag{2.7}$$

where $\Phi_{ws}(k)$ is the cross-spectrum ($= C_{ws}(k) + iQ_{ws}(k)$, where $Q_{ws}(k)$ is the quadrature spectrum) of w and s. Therefore

$$C_{ws}^2(0) = |\Phi_{ws}(0)|^2 \leq \Phi_{ww}(0)\Phi_{ss}(0). \tag{2.8}$$

Substituting the length scales (2.2), (2.3) and (2.4) into (2.8), we find an upper limit for $\mathcal{L}_{ws}$:

$$\mathcal{L}_{ws}^2 \leq \mathcal{L}_w \mathcal{L}_s r_{ws}^{-2}, \tag{2.9}$$

	σ_w^2 (m^2/s^2)	σ_s^2 (K^2)	F (mK/s)	r_{ws}	$\mathcal{L}_w$	$\mathcal{L}_s$	$\mathcal{L}_{ws}$	$\mathcal{L}_f$ (m)	z	z_i
AMTEX01	1.06	0.0297	0.107	0.60	102	122	124	41	100	1200
AMTEX04	0.42	0.0055	0.026	0.54	78	140	102	32	90	1010
AMTEX06	1.20	0.0479	0.153	0.63	122	148	159	50	95	1842
AMTEX07	1.96	0.0225	0.112	0.53	190	229	192	90	315	1100
AMTEX08	1.11	0.0398	0.129	0.61	68	103	93	32	95	1900
ELDOME	0.89	0.0470	0.090	0.44	105	154	161	36	70	2950

TABLE 1. Characteristics of the AMTEX and ELDOME flight legs used in this note (Lenschow *et al.* 1993). The scalar variable used here is air temperature.

where

$$r_{ws} \equiv \frac{F}{\sigma_w \sigma_s}. \tag{2.10}$$

For the data in Table 1, where s is temperature, we find that

$$\mathcal{L}_{ws} \simeq (\mathcal{L}_w \mathcal{L}_s)^{1/2}. \tag{2.11}$$

We use (2.11) to estimate the systematic error from (2.1).

Assuming the functional forms of (2.5) and (2.6) (but not necessarily the values of the coefficients), we obtain by normalizing (2.1) by $F_0 z_i/L$

$$\frac{L}{z_i}\frac{F - \langle F(L)\rangle}{F_0} = b(1 - az_*)z_*^{1/2}, \tag{2.12}$$

where $b = 2(\mathcal{L}_w\mathcal{L}_s)^{1/2}/(z_i z_*^{1/2})$. Because of (2.5) and (2.6), b is independent of z_*. We have also assumed a linear variation of flux with height (which would be the case for a conserved scalar with no differential advection and which is supported by the temperature and humidity flux profiles from FIFE, see §4): $F_z = (1 - az_*)F_0$, where F_0 is the surface flux and $a = 1 - F_{z_i}/F_0$ is defined so that $F_z = F_{z_i}$ = the flux at the top of the CBL when $z_* = 1$.

From (2.5) and (2.6), $b \simeq 1.2$. Alternatively, if we use the observation from Lenschow *et al.* (1993) that $\mathcal{L}_s/\mathcal{L}_w \simeq 1.4$, along with (2.5), we obtain $b \simeq 0.6$. Thus, the value of b is somewhat uncertain, and depends on how the data are treated and on mesoscale structure in the CBL that may vary from case to case.

2.1.1. *Low frequency behavior of spectra*

Before we try to verify the estimate (2.12) empirically we emphasize that there is some arbitrariness to it, due to mesoscale variability. In the results presented by Lenschow *et al.* (1993) the estimates of the integral length scales were obtained from least square fits of an assumed spectral shape to the measured spectra. The spectral form used was

$$\Phi_{yy}(k) = \frac{\mathcal{L}_y \sigma_y^2}{\pi}\frac{1}{1 + k^2\mathcal{L}_y^2}, \tag{2.13}$$

which is the Fourier transform of an exponential autocovariance function,

$$\langle y(x)y(x+\xi)\rangle = \sigma_y^2 \exp(-|\xi|/\mathcal{L}_y). \tag{2.14}$$

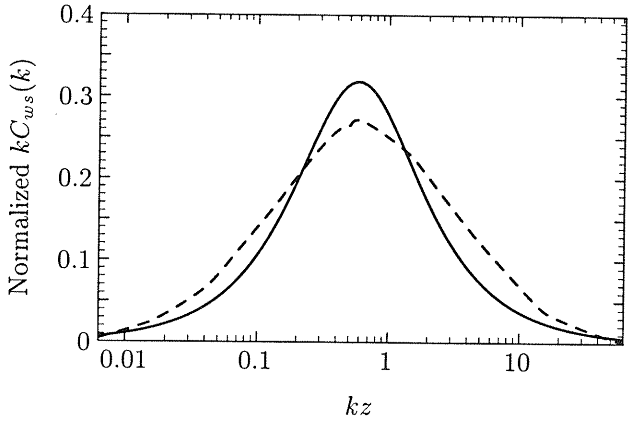

FIGURE 1. Observed surface-layer cospectrum (dashed curve) compared to the model spectrum (2.13) (solid curve). The spectra are normalized so the area under the curves is 1.

On the other hand, Lenschow and Stankov (1986) estimated the integral scales by integrating the autocorrelation function to the first zero crossing. Furthermore, Lenschow and Stankov (1986) used time series that varied from 40 to 170 km in length, with most of the legs 50 to 70 km in length, while Lenschow *et al.* (1993) used legs that were about 180 km (exactly 30 minutes) in length. In practice, scalar variables have mesoscale variations even in otherwise nearly horizontally homogeneous conditions. In AMTEX flights the mean temperature increases along the air trajectory because of heating by the relatively warm ocean. This was largely, but not completely removed by fitting a least-squares linear trend to the data. This large-scale variability can make a large contribution to $\mathcal{L}_s$, but contributes relatively much less to the flux. Lenschow *et al.* (1993) removed these variations by high-pass filtering the temperature series using a Gaussian filter with a length constant equal to $100\mathcal{L}_w$. The result of their analysis is that $\mathcal{L}_s/\mathcal{L}_w = 1.4$, while Lenschow and Stankov (1986) obtained $\mathcal{L}_s/\mathcal{L}_w = 6.2$. The values of $\mathcal{L}_w$ obtained by Lenschow *et al.* (1993) are in reasonable agreement with those of Lenschow and Stankov (1986), while the values of $\mathcal{L}_f$ obtained here are about 45% less than those of Lenschow and Stankov. An important issue that should be investigated further is how best to deal with this mesoscale variability in the scalar fields.

Related to this is the issue of how well the observed spectra and cospectra are fitted with the spectral shape (2.13). Fig. 1 shows that (2.13) predicts a somewhat more peaked cospectrum than what has been observed for surface-layer scalar cospectra from towers (Wesely *et al.* 1989). However, Kaimal *et al.* (1982) point out, based on concurrent aircraft and tower measurements, that aircraft w spectra tend to be somewhat more peaked than tower spectra. Certainly at the high wavenumber end, the model spectral shape decreases somewhat more rapidly than has been observed since the model predicts a -2 slope, as compared to the observed $-\frac{5}{3}$ slope for spectra. However, this difference has negligible impact on the integral scale; rather the behavior at low wavenumbers is much more critical. Fig. 2 shows least-square fits of (2.13) to the spectra and cospectra calculated for the airplane time series. Generally there is good agreement with the assumed spectral shape. The large wavenumber region of the scalar (temperature) spectra is larger than predicted because of random noise present in the recorded signal.

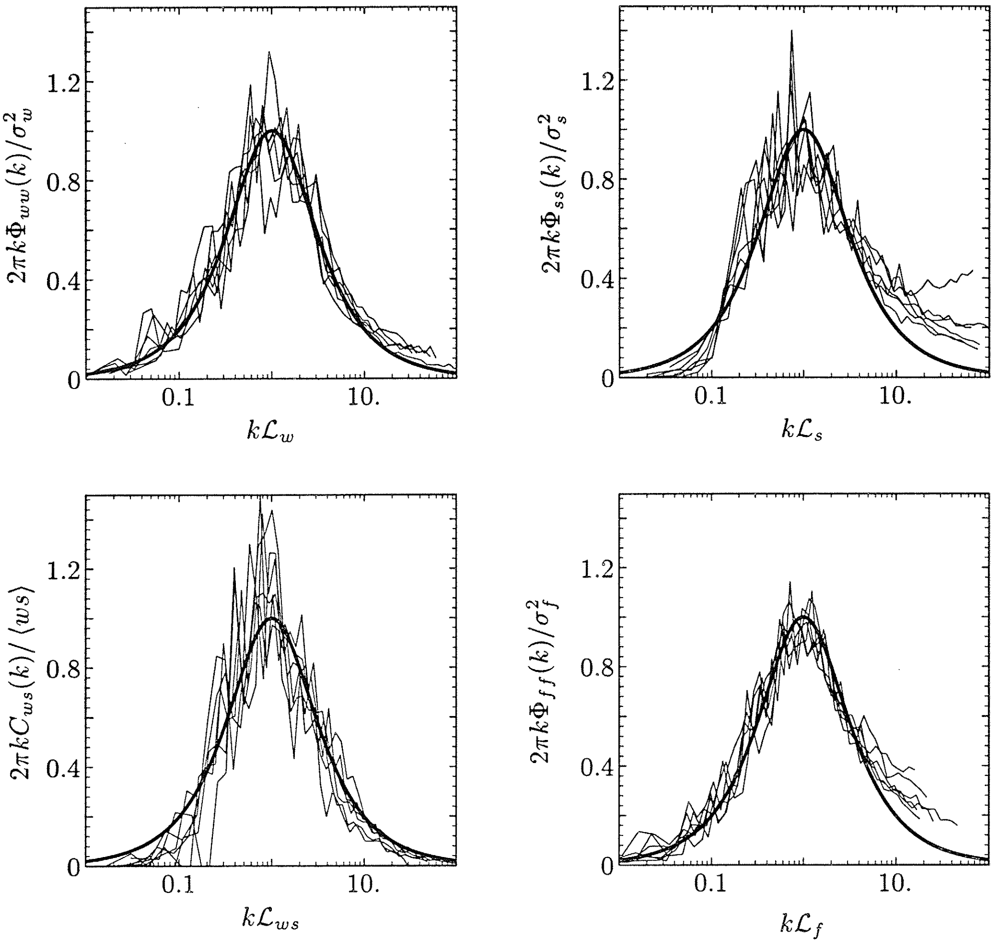

FIGURE 2. Least squares fit to spectra and cospectra for the time series in Table 1. Noise is present in some of the scalar spectra at large wavenumbers. The spectra are normalized so that $\Phi(1/\mathcal{L}) = 1$.

2.2. *Random flux errors*

According to Lenschow *et al.* (1993) the random error of the flux estimate obtained for two joint-Gaussian distributed variables over a leg of length L normalized by the surface flux is

$$\frac{\sigma_F(L)}{F_0} = \left(\frac{2\mathcal{L}_f}{L}\right)^{1/2} \left(\frac{1+r_{ws}^2}{r_{ws}^2}\right)^{1/2} (1 - az_*). \tag{2.15}$$

Lenschow and Stankov (1986) find from mixed-layer observations that

$$\mathcal{L}_f = 0.16 z_i z_*^{1/3}, \tag{2.16}$$

so that (2.15) becomes

$$\left(\frac{L}{z_i}\right)^{1/2} \frac{\sigma_F(L)}{F_0} = 0.57 z_*^{1/6} \left(\frac{1+r_{ws}^2}{r_{ws}^2}\right)^{1/2} (1 - az_*). \tag{2.17}$$

In order to evaluate r_{ws} in (2.15), we resort to a collage of empirical results from both

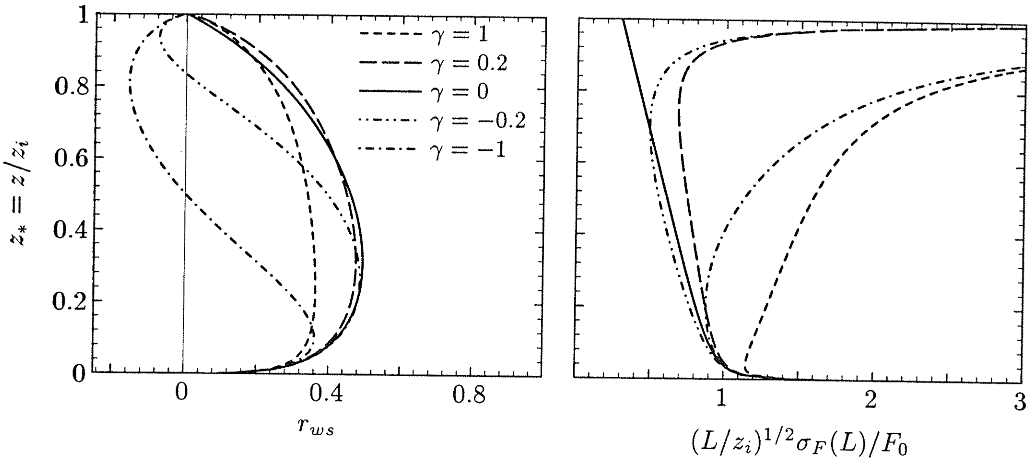

FIGURE 3. The correlation coefficient, r_{ws}, from (2.23) for various values of $\gamma = F_{z_i}/F_0$ and the random flux error according to (2.17). The curves are valid for the approximate range of $0.1 < z_* < 0.9$.

observations and large eddy simulations (LES). We first incorporate the "top-down – bottom-up" formulation for the relationship between fluxes of s at the surface F_0 and at the top F_{zi} of the CBL developed by Moeng & Wyngaard (1989), and $\sigma_s^2(z_*)$:

$$\sigma_s^2(z_*) = \left(\frac{F_0}{w_*}\right)^2 f_b + 2\left(\frac{F_0 F_{z_i}}{w_*^2}\right) f_{tb} + \left(\frac{F_{z_i}}{w_*}\right)^2 f_t, \tag{2.18}$$

where w_* is the convective velocity scale, and $f_b(z_*)$, $f_t(z_*)$, and $f_{tb}(z_*)$ are dimensionless similarity functions for variance from the bottom-up and top-down diffusion processes. These functions were estimated from large-eddy simulations (Moeng & Wyngaard 1989); their results fit the functions:

$$f_b \simeq z_*^{-0.9} \qquad \text{for} \quad z_* > 0.1 \tag{2.19}$$

$$f_t \simeq 3.1(1 - z_*)^{-3/2} \tag{2.20}$$

$$f_{tb} \simeq 1.5. \tag{2.21}$$

Combining this with the estimate of

$$\sigma_w^2 = 1.8 w_*^2 z_*^{2/3}(1 - 0.8 z_*)^2 \tag{2.22}$$

obtained by Lenschow *et al.* (1980) from aircraft measurements, assuming a linear variation of flux with height and solving for r_{ws}, we obtain

$$r_{ws} = \frac{1 + (\gamma - 1) z_*}{1.34 z_*^{1/3}(1 - 0.8 z_*)[z_*^{-0.9} + 3.1\gamma^2(1 - z_*)^{-3/2} + 3\gamma]^{1/2}}, \tag{2.23}$$

where $\gamma = 1 - a = F_{z_i}/F_0$. Values of r_{ws} for a range of γ are shown in Fig. 3. For temperature fluxes in the CBL γ is -0.2 to -0.4, and we see that the values on the figure agree reasonably with the data in Table 1 which are obtained in the lower third of the mixed layer. The random error incorporating these various values of r_{ws} is also given in Fig. 3.

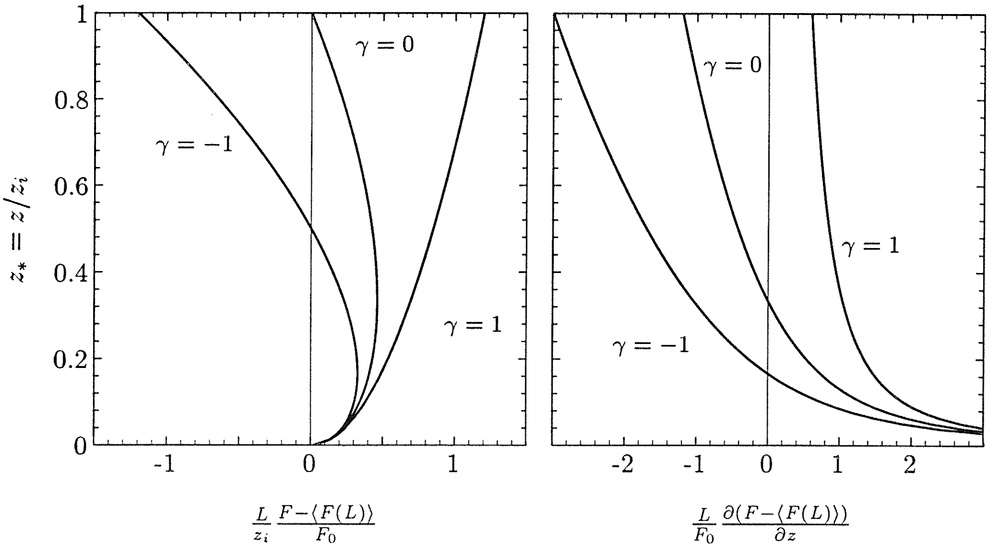

FIGURE 4. Normalized systematic errors of the flux (left plot, eq. 2.12 with $b = 1.2$) and the vertical flux divergence (right plot, eq. 3.1, $b = 1.2$) for various values of $\gamma = F_{z_i}/F_0$.

3. Errors of flux gradients

We first derive an expression for the systematic error and then for the random error of the vertical flux gradient or divergence.

3.1. *Systematic errors*

Differentiating (2.12) with respect to height, the normalized systematic error in the flux divergence is

$$\frac{L}{F_0}\frac{\partial(F-\langle F(L)\rangle)}{\partial z} \simeq \frac{b}{2}(1-az_*)z_*^{-1/2} - baz_*^{1/2}. \tag{3.1}$$

We note that the error (3.1) passes through zero and thus changes sign at $z_* = (3a)^{-1}$. The systematic errors of the normalized flux and flux divergence, (2.12) and (3.1), are plotted in Fig. 4 using the more conservative (larger systematic error) estimate of $b = 1.2$.

3.2. *Random errors of flux gradients*

In order to measure the flux gradient, flux measurements at several heights are needed. It is obvious that the more flight legs used to estimate the flux gradient the smaller the random error, and if all the flights legs are at roughly the same height it is very difficult to estimate a vertical flux gradient. In the following we shall quantify these considerations.

If we assume that the random errors of the individual legs are roughly equal, i.e. $\sigma_F^2(L,z) \approx \sigma_F^2(\overline{L},\overline{z})$, where the overbar denotes a mean value of all the legs used in the flux gradient measurement, we can use a standard expression for fitting straight lines to a set of data points (linear regression) given by Press *et al.* (1986). With this expression, the random error of the gradient is

$$\sigma^2_{\partial F/\partial z} = \frac{\sigma_F^2(\overline{L},\overline{z})}{N\sigma_z^2}, \tag{3.2}$$

where N is the number of legs and σ_z^2 is the variance of the mean heights of the set of

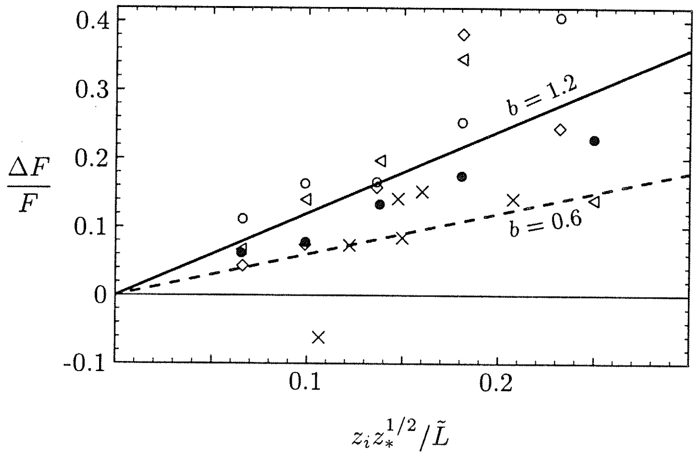

FIGURE 5. Systematic error of scalar flux as a function of $z_i z_*^{1/2}/\tilde{L}$. Sensible heat fluxes: ○, Wyoming King Air; ●, NRC Twin Otter; ×, AMTEX. Latent heat fluxes: ◇, Wyoming King Air; ◁, NRC Twin Otter. The lines are the predicted errors with different values of b (see (2.12) or (4.1)).

N legs. Furthermore, we often estimate the surface flux by linearly extrapolating fluxes measured at several flight levels to the surface. Under the same assumptions leading to (3.2) the random error of the surface flux F_0 is (Press *et al.* 1986)

$$\sigma_{F_0}^2 = \frac{\sigma_F^2(\overline{L},\overline{z})\overline{z^2}}{N\sigma_z^2}. \tag{3.3}$$

Equation (3.3) can be used to design flight patterns for a minimum random error of the surface flux. If z_b is the lowest flight level that can be flown and z_t is the highest flight level within the CBL, then, still assuming σ_F to be roughly constant in this height interval, it can easily be shown that $\sigma_{F_0}^2$ is minimized if $Nz_b/(z_t + z_b)$ legs are flown at z_t and $Nz_t/(z_t + z_b)$ at z_b. As an example, suppose that 18 flight legs are available, and $z_b \approx 0.1$ and $z_t \approx 0.8$. Then the most reasonable distribution of heights that will minimize $\sigma_{F_0}^2$ is 2 at z_t and 16 at z_b. Thus to accurately estimate the surface flux, the optimal approach is to minimize the flux measurement error at the lowest flight level.

4. Experimental verification

In order to verify the estimates of the systematic error of the flux and the flux gradient, (2.12) and (3.1), we use data from the Canadian National Research Council Twin Otter and the University of Wyoming King Air research aircraft obtained during the First International Satellite Land Surface Climatology Project (ISLSCP) Field Experiment (FIFE) as described by Kelly *et al.* (1992). We use both the sensible and latent heat flux from these sources. We also use the sensible heat flux data from AMTEX and ELDOME described in Lenschow *et al.* (1993).

Two different flux estimates are given for each leg in the FIFE data. The first is calculated from detrended time series while the second is from high-pass filtered time series. Kelly *et al.* (1992) use a third-order recursive filter with a cut-off wave length of 5 km. Lenschow *et al.* (1993) used in their theoretical analysis a simple high-pass

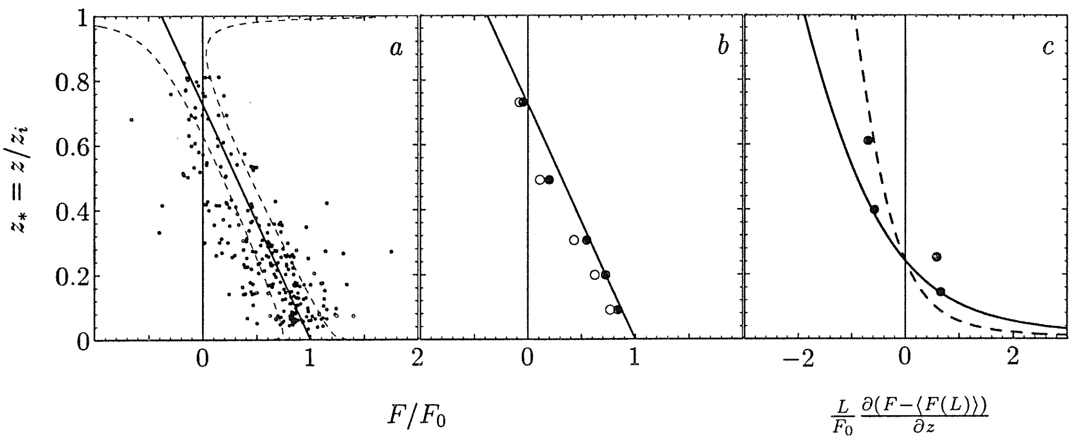

FIGURE 6. *a*: Scatter plot of unfiltered (detrended) sensible heat flux from 261 flight legs. The line is $F(z_*)/F_0 = 1 - az_*$ with $a = 1.38$ and the dashed lines are the expected $\pm 1\sigma$ deviations from (2.17). *b*: Averaged profiles of sensible heat flux. The dots are unfiltered measurements while the circles are filtered. *c*: From these average profiles the systematic error of the flux gradient is calculated. The curves are the predicted error from (3.1) with $a = 1.38$ and $b = 0.6$ and 1.2, respectively.

removal of running mean filter. It can be shown that if we choose the length scale in running mean filter of Lenschow *et al.* to be $L_{rm} = 2.8$ km, the spectral attenuation will closely resemble that of the filter of Kelly *et al.*.

4.1. *Systematic flux errors*

The systematic error contributed by the difference between using a detrended time series and the high-pass filter can be predicted from (2.12) and written as (after replacing F_0 by $F(1 - az_*)^{-1}$):

$$\Delta F = \langle F(L)\rangle - \langle F(L_{rm})\rangle \approx b\frac{z_i z_*^{1/2}}{\tilde{L}}F \qquad (4.1)$$

where $\tilde{L}^{-1} = L_{rm}^{-1} - L^{-1}$. Thus for a given narrow range of values of the parameter $z_i z_*^{1/2}/\tilde{L}$ there is a linear relation between ΔF and the flux, F. We extract the constant of proportionality of the relation $\Delta F \propto F$ by a least squares fit of (4.1) to all points, $\{F(L), F(L) - F(L_{rm})\}$, which have $z_i z_*^{1/2}/\tilde{L}$ in the same narrow bin. For this analysis we chose only flight legs with $L > 12.5$ km. The average length is 21 km for the 401 Twin Otter legs and 15.6 km for the 134 King Air legs. The results are shown in Fig. 5. Because we have used fewer legs from the King Air these points have more scatter.

The analysis of the AMTEX and ELDOME data is simpler since we have a few very long legs instead of many short legs. For these legs we first calculate the flux for the detrended 180 km data series. Then the series are divided into 64 sections 2.8 km in length from which we estimate $\langle F(2.8 \text{ km})\rangle$. $\Delta F/F$ is calculated for all six runs analyzed by Lenschow *et al.* (1993) (×'s in Fig. 5).

4.2. *Systematic flux gradient errors*

It is difficult to obtain accurate measurements of flux gradients, and therefore even more difficult to empirically estimate their systematic error. In order to get sufficient statistical

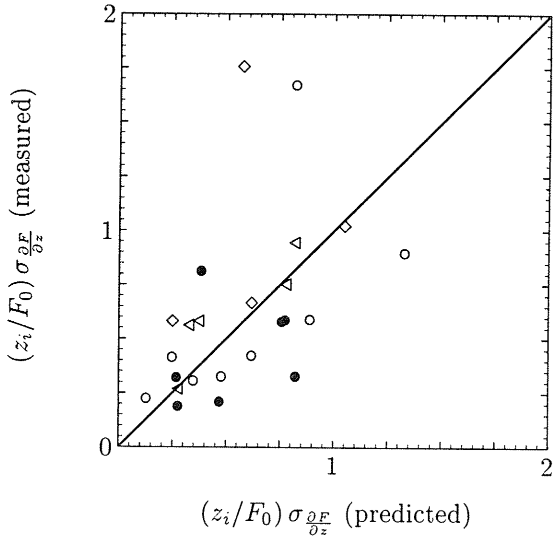

FIGURE 7. Random error of flux gradient (3.2). See caption to Fig. 5 for list of symbols.

significance from the flux gradient measurements so that we can compare (3.1) with the observations, we found that it was not sufficient to just compare the flux gradients derived from filtered and unfiltered flux measurements from the ~ 20 legs of a typical FIFE flight. This is because the random error from this limited number of legs is large enough to obscure the systematic error. Instead we combine all sensible heat fluxes (from legs with $L > 12.5$ km) from all FIFE flights. First, all sensible heat fluxes are normalized by the surface flux, F_0, determined by linear extrapolation of the fluxes from each flight to the surface (Fig. 6*a*). All sensible heat fluxes from all 261 flight legs are then treated as if they were obtained from one flight. It is possible to proceed in this way with the sensible heat flux because all flights have roughly the same normalized flux gradient, while the latent heat flux gradients vary widely (Betts *et al.* 1990, 1992). Both the unfiltered (detrended) and filtered normalized fluxes are then grouped with respect to normalized CBL height and averaged (Fig. 6*b*). Finally, we calculate flux gradients from the averaged filtered and unfiltered fluxes and take the difference in order to estimate the systematic errors. These are compared to the prediction (3.1) with $b = 0.6$ and 1.2. We see in Fig. 6*c* that the systematic error changes sign somewhere in the vicinity of $z_* = 0.25$, which agrees with the prediction discussed in (§3.1) for a value of $a = 1.38$. This is the value of a that is consistent with the data in Fig. 6*a*.

4.3. *Random errors*

We also see in Fig. 6*a* that the estimated random flux error agrees well with the prediction in the lower part of the CBL. Higher up the data show more scatter than predicted. This is mainly because we assume $a = 1.38$, while in fact a varies considerably from flight to flight; for some of the flights $a > 2$.

The random error of the flux gradient is predicted by (3.2) and is estimated from the data for each flight (up to 26 legs per flight) by using all combinations of four legs that are well spread out through the CBL. We then compare the random error of these estimates to (3.2) using $N = 4$, and the mean values of L, z, a and σ_z. Despite considerable scatter the measured results displayed in Fig. 7 agree reasonably well with the prediction (3.2).

5. Discussion

We now apply the formulations for systematic and random flux and flux divergence errors to a specific example to illustrate their impact. We select $z_i = 1000$ m, $z = 200$ m, high-pass filtering with $L_{rm} = 2800$ m, and $b = 1.2$. If we assume that the length of the flight leg $L \gg L_{rm}$, this example gives a systematic error (4.1) of 19%, i.e. the filtered signal gives a 19% lower flux compared to the unfiltered. For comparison, we now calculate how long a flight leg is required to reduce the random error to $< 19\%$. From (2.17), using the flux at flight level for normalization and $r_{ws} = 0.56$, we obtain $L > 22$ km. We note, however, that the systematic error scales with L_{rm}^{-1}, while the random error scales with $L^{-1/2}$. Thus if we, for example, increase L_{rm} by a factor of two, which halves the systematic error, we must increase L by a factor of four to halve the random error.

If we now further assume in the previous example that $a = 1$, i.e., that $\gamma = 0$, which means that the flux linearly decreases to zero at z_i, the systematic error in the flux divergence, obtained by multiplying (3.1) by z_i/L_{rm} is about 47% at $z_* = 0.1$, decreasing monotonically to about -38% at $z_* = 0.9$. Thus, through most of the CBL, the systematic error in the flux divergence for this example is comparable to that for the flux; however, near the surface, it can become considerably larger. In order to keep the random error in the flux divergence at less than 40%, assuming a set of flight legs of 22 km length and a value of $\sigma_z = 0.2z_i$, from (3.2), the number of flight legs $N \geq 6$.

These results show quantitatively the systematic error of high-pass filtering, or of averaging together several relatively short (e.g., less than ten times the depth of the CBL) flight legs to obtain the flux and flux divergence. One might ask, however, whether fluxes or flux divergences that have significant systematic error can be corrected with the formulations obtained here. To some extent, they undoubtedly can be, but the scatter in the data is considerable, which means that this practice would be no substitute for directly measuring the significant contributions to the flux. Significant factors contributing to this scatter are: (1) the contribution of mesoscale variations, which do not necessarily scale with z_i, to the fluxes; (2) possible organization of the convective eddies relative to the mean wind direction; and (3) over land, the effects of a horizontally inhomogeneous surface on the distribution and sizes of the convective eddies. This is an area worthy of further research.

We are indebted to Robert D. Kelly of the University of Wyoming for providing the FIFE data and explaining the high-pass filtering process. J. M. is grateful to the Danish Research Academy for supporting his visit to NCAR.

REFERENCES

Betts, A. K., R. L. Desjardins & J. I. MacPherson, Budget Analysis of the Boundary Layer Grid Flights During FIFE 1987. *J. Geophys. Res.*, **97**, D17, 18,533–18,546, 1992.

Betts, A. K., R. L. Desjardins, J. I. MacPherson, and R. D. Kelly Boundary-layer heat and moisture budgets from FIFE. *Boundary-Layer Meteorol.*, **50**, 109–137, 1990.

Grossman, R. L., Convective boundary layer budgets of moisture and sensible heat over an unstressed prairie. *J. Geophys. Res.*, **97**, D17, 18,425–18,438, 1992a.

Grossman, R. L., Sampling errors in the vertical fluxes of potential temperature and moisture measured by aircraft during FIFE. *J. Geophys. Res.*, **97**, D17, 18,439–18,443, 1992b.

Kaimal, J. C., R. A. Eversole, D. H. Lenschow, B. B. Stankov, P. H. Kahn, and J. A. Businger, Spectral characteristics of the convective boundary layer over uneven terrain. *J. Atmos. Sci.*, **39**, 1098–1114, 1982.

Kelly, R. D., E. A. Smith and J. I. MacPherson, A comparison of surface sensible and latent heat fluxes from aircraft and surface measurements in FIFE 1987. *J. Geophys. Res.*, **97**, D17, 18,445–18,453, 1992.

Lenschow, D. H., Micrometeorological techniques for measuring biosphere-atmosphere trace gas exchange. A chapter in *Methods in Ecology: Trace Gases*, edited by P. Matson and R. Harriss, Blackwell Scientific Publications, Cambridge, MA., in press, 1993.

Lenschow, D. H., J. Mann and L. Kristensen, How long is long enough when measuring fluxes and other turbulence statistics? to appear in *J. Atmos. and Oceanic Tech.*. Also available as *NCAR Tech. Note,* NCAR/TN-389+STR (unabridged version), 53 pp., National Center for Atmospheric Research, Boulder, CO, 1993.

Lenschow, D. H. and B. B. Stankov, Length Scales in the convective boundary Layer. *J. Atmos. Sci.*, **43**, 1198–1209,

Lenschow, D. H., J. C. Wyngaard and W. T. Pennell, Mean-field and second-moment budgets in a baroclinic, convective boundary layer. *J. Atmos. Sci.*, **37**, 1313–1326, 1980.

Moeng C.-H., and J. C. Wyngaard, Evaluation of turbulent transport and dissipation closures in second-order modeling. *J. Atmos. Sci.*, **46**, 2311–2330, 1989.

Press, W. H., B. P. Flannery, S. A. Teukolsky, and W. T. Vetterling, *Numerical Recipes*, 735 pp., Cambridge University Press, 1986.

Wesely, M. L., D. H. Lenschow and O. T. Denmead, Flux measurement techniques, a chapter in *Global Tropospheric Chemistry: Chemical Fluxes in the Global Atmosphere*, edited by D. H. Lenschow and B. B. Hicks, pp. 31–46, published by NCAR, P.O. Box 3000, Boulder, CO 80307, 1989.

Dansk sammendrag

Denne afhandling består af to dele. I første del udvikles en model for den rumlige struktur af atmosfærisk turbulens ved høje vindhastigheder. En sådan model kan bruges til at beregne dynamiske laster på konstruktioner, der har en rumlig udstrækning så som vindmøller, hængebroer og master. Modellen består af en spektral tensor, der for enhver bølgevektor $\boldsymbol{k}$ er en 3 gange 3 covarians matrix af de tre hastigheds komposanter's Fourier komponenter hørende til $\boldsymbol{k}$. Modellen bygger på en række antagelser: Den atmosfæriske vindprofil kan, over det område, der har interesse for en given konstruktion, approksimeres med en lineær profil. Vindfeltet antages også at være statistisk homogent i rummet, hvilket igen kun kan være en god approximation over et begrænset højdeinterval.

Modellen bygger på en kombination af *Rapid Distortion Theory* — en linearisering af Navier–Stokes ligningerne — og af estimater af turbulente 'hvirvlers' levetider. Modellen indeholder kun tre justerbare parametre, der kan bestemmes ud fra observationer af spektre målt i ét punkt, hvorefter alle topunkts-spektre kan forudsiges v.h.a. modellen.

To atmosfæriske eksperimenter analyseres for at bekræfte modellen. Det ene er Store Bælts Kohærens Eksperimentet, hvor tre vindvektor sensorer (soniske anemometre) målte turbulente hastigheder i tre punkter i 70 meters højde. Som det ses af figur IA.8 på side 30 er kohærenserne (de normerede krydsspektre) godt forudsagt, måske med undtagelse af de vertikale vindfluktuationer, hvor kohærensen er overestimeret.

Ni anemometre indgår i Lammefjords Eksperimentet, som også er blevet brugt til at teste modellen (se §IA.4.5). Igen er forudsigelserne tilfredsstillende i store træk. En anden lidt mere kompliceret model, der tager hensyn til jordoverfladens blokering af de turbulente strømninger, forudsiger visse aspekter af andenordens statistikken lidt bedre (se §IA.3.3).

I del IB anvendes tensormodellen til at simulere turbulente hastighedsfelter til brug for lastberegninger på konstruktioner. Desuden bruges den til beregning af korrektioner til momentumfluksmålinger for instrumenter, der ikke måler horisontale og vertikale hastighedsfluktuationer i samme punkt i rummet. En sidste anvendelse er en analyse af strukturen af turbulensen i Skibteknisk Laboratoriums brede grænselagsvindtunnel. Her er analysen brugbar i forbindelse med forudsigelser af last på broer ud fra vindtunnel model målinger.

I anden del af afhandlingen udvikles matematiske modeller til at bestemme hvor lange tidsserier skal være for at estimere ko-varianser (flukse) og højere ordens momenter med en given statistisk usikkerhed. For en given midlingstid T er der en systematisk forskel på den sande fluks eller moment og middelværdien af den tidsmidlede størrelse. F.eks. vil variansen af en meget lang tidsserie være større end variansen af små stykker af samme tidsserie (se figur IIA.2). Denne forskel, *den systematiske fejl*, er en aftagende funktion af T og går mod 0, når $T \to \infty$. Variansen af de tidsmidlede målinger (flukse eller momenter), den såkaldte *fejlvarians* eller tilfældige fejl, er også, når T er meget større end integraltidsskalaen $\mathcal{T}$, en aftagende funktion af T. Under antagelse af, at de involverede stokastiske processer er gaussiske med exponentielle korrelationsfunktioner, bestemmes systematiske og tilfældige fejl som funktion af T. Det viser sig imidlertid, at antagelsen om gaussiske processer fører til undervurderinger af de tilfældige fejl. Ved en analyse af ikke-gaussiske processer med mere realistiske skævheder (for turbulente atmosfæriske tidsserier) kan tilfældige fejl bedre forudsiges.

Del IIB anvender de matematiske værktøjer fra del IIA til at estimere tilfældige og systematiske fejl af flukse og fluksgradienter i det konvektive atmosfæriske grænselag.

Bibliographic Data Sheet **Risø–R–727(EN)**

Title and author(s)

Models in micrometeorology

Jakob Mann

ISBN	ISSN
87–550–1950–1	0106–2840

Dept. or group	Date
Meteorology and Wind Energy	March 1994

Groups own reg. number(s)	Project/contract No.

Pages	Tables	Illustrations	References
127	17	52	87

Abstract (Max. 2000 char.)

This report consists of two parts. In the first a spectral tensor model of neutral atmospheric surface layer turbulence is developed. The model is validated trough comparison with second order turbulence statistics from the Great Belt Coherence Experiment, the Lammefjords Experiment and wind tunnel data from Danish Maritime Institute. Based on the spectral tensor an efficient and simple algorithm for simulation of three-dimensional wind fields is generated. The simulation is well suited for load calculation on bridges, wind turbines and other engineering structures. The spectral tensor is also used to estimate errors in momentum flux measurements close to the ground due to displacement of the sensors of vertical and horizontal velocity fluctuations.

In the second part mathematical tools are developed to determine how long a time series of a turbulent signal must be to estimate covariances and higher order moments with a specified statistical significance. Both systematic and random errors are treated. It is demonstrated theoretically, as well as experimentally with aircraft data from the convective boundary layer over the ocean and over land, that if the time series are assumed to be Gaussian the random errors are underestimated. A skewed model process gives better estimates of the random error. The tools are used in the convective boundary layer to show that the systematic flux and flux gradient errors can be important if fluxes are calculated from a set of several short flight legs or if the vertical velocity and scalar time series are high-pass filtered.

Descriptors INIS/EDB

ANEMOMETERS; BOUNDARY LAYERS; BRIDGES; COMPUTERIZED SIMULATION; FLOW MODELS; FLUCTUATIONS; METEOROLOGY; SHEAR; STATISTICS; STOCHASTIC PROCESSES; TENSORS; TURBULENCE; VELOCITY; WIND; WIND LOADS; WIND TURBINES

Available on request from:
Risø Library, Risø National Laboratory (Risø Bibliotek, Forskningscenter Risø)
P.O. Box 49, DK-4000 Roskilde, Denmark
Phone (+45) 46 77 46 77, ext. 4004/4005 · Telex 43 116 · Telefax (+45) 46 75 56 27